Journal of
Mechanics of Materials and Structures

Volume 7, No. 5 May 2012

mathematical sciences publishers

JOURNAL OF MECHANICS OF MATERIALS AND STRUCTURES

jomms.net

Founded by Charles R. Steele and Marie-Louise Steele

See http://jomms.net for submission guidelines.

JoMMS (ISSN 1559-3959) is published in 10 issues a year. The subscription price for 2012 is US $555/year for the electronic version, and $735/year (+$60 shipping outside the US) for print and electronic. Subscriptions, requests for back issues, and changes of address should be sent to Mathematical Sciences Publishers, Department of Mathematics, University of California, Berkeley, CA 94720–3840.

JoMMS peer-review and production is managed by EditFLOW® from Mathematical Sciences Publishers.

PUBLISHED BY
mathematical sciences publishers
http://msp.org/

A NON-PROFIT CORPORATION

Typeset in LaTeX

JOURNAL OF MECHANICS OF MATERIALS AND STRUCTURES
Vol. 7, No. 5, 2012
dx.doi.org/10.2140/jomms.2012.7.413

SCALE EFFECTS ON ULTRASONIC WAVE DISPERSION CHARACTERISTICS OF MONOLAYER GRAPHENE EMBEDDED IN AN ELASTIC MEDIUM

SAGGAM NARENDAR AND SRINIVASAN GOPALAKRISHNAN

Ultrasonic wave propagation in a graphene sheet, which is embedded in an elastic medium, is studied using nonlocal elasticity theory incorporating small-scale effects. The graphene sheet is modeled as an one-atom thick isotropic plate and the elastic medium/substrate is modeled as distributed springs. For this model, the nonlocal governing differential equations of motion are derived from the minimization of the total potential energy of the entire system. After that, an ultrasonic type of wave propagation model is also derived. The explicit expressions for the cut-off frequencies are also obtained as functions of the nonlocal scaling parameter and the y-directional wavenumber. Local elasticity shows that the wave will propagate even at higher frequencies. But nonlocal elasticity predicts that the waves can propagate only up to certain frequencies (called escape frequencies), after which the wave velocity becomes zero. The results also show that the escape frequencies are purely a function of the nonlocal scaling parameter. The effect of the elastic medium is captured in the wave dispersion analysis and this analysis is explained with respect to both local and nonlocal elasticity. The simulations show that the elastic medium affects only the flexural wave mode in the graphene sheet. The presence of the elastic matrix increases the band gap of the flexural mode. The present results can provide useful guidance for the design of next-generation nanodevices in which graphene-based composites act as a major element.

1. Introduction

Graphene [Geim and Novoselov 2007], the two-dimensional (2D) counterpart of three-dimensional (3D) graphite, has attracted vast interest in solid-state physics, materials science, and nanoelectronics since it was discovered in 2004 as the first free-standing 2D crystal. Graphene is considered a promising electronic material in postsilicon electronics. However, large-scale synthesis of high-quality graphene represents a bottleneck for next-generation graphene devices. Existing routes for graphene synthesis include mechanical exfoliation of highly ordered pyrolytic graphite [Novoselov et al. 2004], eliminating Si from the surface of single-crystal SiC [Ohta et al. 2006], depositing graphene at the surface of single-crystal [Oshima and Nagashima 1997] or polycrystalline metals [Obraztsov et al. 2007], and various wet-chemistry-based approaches [Gómez-Navarro et al. 2007; Li et al. 2008]. However, up to now no methods have delivered high quality graphene with the large area required for applications such as practical electronic materials. In recent years, these nanostructured materials have spurred considerable interest in the materials community because of their potential for large gains in mechanical and physical properties as compared to standard structural materials. Since controlled experiments in nanoscale are

Keywords: monolayer graphene, nonlocal elasticity theory, wavenumber, spectrum, dispersion, phase velocity, escape frequency, cut-off frequency.

difficult and molecular dynamics simulations are expensive and formidable, especially for large scale systems, modified continuum models have been widely and successfully used to study the mechanical behavior of nanostructures like carbon nanotubes (CNTs), graphene sheets (GSs), nanofibers/wires, etc. [Tomanek and Enbody 2000].

A nanostructure is defined as a material system or object where at least one of the dimensions is below 100 nm. Oxide nanostructures can be classified into three categories: zero-dimensional (0D); one-dimensional (1D); and two-dimensional (2D). 0D nanostructures are materials in which all three dimensions are at the nanoscale. Good examples of these materials are buckminsterfullerenes [Kroto et al. 1985] and quantum dots [Dabbousi et al. 1997]. 1D nanostructures are materials that have two physical dimensions in the nanometer range while the third dimension can be large, such as in CNTs [Vossen and Kern 1978]. 2D nanostructures, or thin films, only have one dimension in the nanometer range and can be used readily in the processing of complimentary metal-oxide semiconductor transistors [Senturia 2001] and microelectromechanical systems [Martin 1996]. Since the focus of this work is on 2D nanostructures, the others will not be discussed from this point forward. 2D nanostructures (here graphene sheets) have stimulated a great deal of interest due to their importance in fundamental scientific research and potential technological applications in the development of GS-based nanodevices such as strain sensors, mass and pressure sensors, atomic dust detectors, enhancers of surface image resolution, etc.

In contrast to the investigations of CNTs, it is surprising to find that very few studies have been reported in the literature on the theoretical modeling of GSs, even though graphene possesses many superior properties [Luo and Chung 2000], such as good electrical and thermal conductivities parallel to the sheets and poor conductivities normal to the sheets, which makes it suitable for gasket material in high-temperature or chemical environments; good flexibility, which suggests its use as a vibration damping material; and a high strength-to-weight ratio, which makes it an ideal material for sports equipment. Recently, Behfar and Naghdabadi [2005] investigated the nanoscale vibration of a multilayered graphene sheet (MLGS) embedded in an elastic medium, in which the natural frequencies as well as the associated modes were determined using a continuum-based model. The influence of carbon-carbon and carbon-polymer van der Waals (VDW) forces are considered in their work. They further studied the bending modulus of a MLGS using a geometrically based analytical approach [Behfar et al. 2006]. The bending energy in their analysis is based on the VDW interactions of atoms belonging to two neighboring sheets. Their calculations are performed for a double-layered GS, but the derived bending modulus is generalized to a MLGS composed of many double-layered GSs along its thickness, in which the double-layered GSs are alternately the same in configuration. In addition, it should be mentioned that graphite is composed of multilayered sheets, but it was recently reported [Horiuchi et al. 2004] that single-layered sheets are detectable in carbon nanofilms. Sakhaee-Pour et al. [2008a] have studied the free vibrational behavior of single-layer graphene sheets (SLGS) while considering the effects of chirality and aspect ratio as well as boundary conditions, and have developed predictive models for computing the natural frequencies. The potential applications of SLGSs as mass sensors and atomistic dust detectors have further been investigated [Sakhaee-Pour et al. 2008b]. Also, the promising usage of SLGSs as strain sensors has been examined [Sakhaee-Pour and Ahmadian 2008].

The small scale of nanotechnology makes the applicability of classical and local continuum models, such as beam and shell models, questionable. Classical continuum models do not admit intrinsic size

dependence in the elastic solutions of inclusions and inhomogeneities. At nanometer scales, however, size effects often become prominent, the cause of which needs to be explicitly addressed due to an increasing interest in the general area of nanotechnology [Li et al. 2008]. Sun and Zhang (see [Tomanek and Enbody 2000]) indicated the importance of semicontinuum models in analyzing nanomaterials after pointing out the limitations of the applicability of classical continuum models to nanotechnology. In their semicontinuum model for nanostructured materials with plate-like geometry, the material properties were found to be completely dependent on the thickness of the plate structure, contrary to classical continuum models. The modeling of such a size-dependent phenomenon has become an interesting research subject in this field [Vossen and Kern 1978; Kroto et al. 1985; Dabbousi et al. 1997]. It is thus concluded that the applicability of classical continuum models at very small scales is questionable, since the material microstructure, such as the lattice spacing between individual atoms, becomes increasingly important at small sizes and the discrete structure of the material can no longer be homogenized into a continuum. Therefore, continuum models need to be extended to consider the scale effect in nanomaterial studies.

At nanometer scales, size effects often become prominent. Both experimental and atomistic simulation results have shown a significant size-effect in the mechanical properties when the dimensions of these structures become small. As the length scales are reduced, the influences of long-range interatomic and intermolecular cohesive forces on the static and dynamic properties tend to be significant and cannot be neglected. The classical theory of elasticity, being the long wave limit of atomic theory, excludes these effects. Thus traditional classical continuum mechanics would fail to capture small-scale effects when dealing in nanostructures. Small-size analysis using local theory over predicts the results. Thus the consideration of small effects is necessary for correct prediction of micro/nanostructures. Various size-dependent continuum theories which capture the small scale parameter such as couple-stress elasticity theory [Zhou and Li 2001], strain gradient theory [Fleck and Hutchinson 1997], and modified couple-stress theory [Yang et al. 2002] have been reported. These modified continuum theories are being used for the analysis of small-scale structures. However, the most used continuum theory for analyzing small-scale structures is Eringen's nonlocal elasticity theory [Eringen 1972; 1976; 1983; Eringen and Edelen 1972]. The essence of nonlocal elasticity theory is that the small-scale effects are captured by assuming that the stress at a point is a function of the strains at all the other points in the domain. Nonlocal theory considers long-range interatomic interaction and yields results dependent on the size of a body. It is also reported in [Chen et al. 2004] that nonlocal continuum theory-based models are physically reasonable from the atomistic viewpoint of lattice dynamics and molecular dynamics simulations. Understanding the importance of employing nonlocal elasticity theory in small-scale structures, a number of research works have conducted static, dynamic, and stability analyses of micro/nanostructures [Yakobson et al. 1997; Peddieson et al. 2003; Wang 2005; Wang and Hu 2005; Lu et al. 2006; 2007; Duan and Wang 2007; Duan et al. 2007; Ece and Aydoydu 2007; Lim and Wang 2007; Lu 2007; Reddy 2007; Wang and Liew 2007; Adali 2008; Kumar et al. 2008; Reddy and Pang 2008; Tounsi et al. 2008; Wang and Duan 2008; Yang et al. 2008; Aydogdu 2009a; 2009b; Murmu and Pradhan 2009; Narendar and Gopalakrishnan 2009a; 2009b; 2010a; 2010b; 2010c; 2010d; Narendar et al. 2010].

All engineering materials possess intrinsic length scales in terms of their repetitive atomic or molecular structures. The classical theory of elasticity, which is commonly used to explain the behavior of these materials, however, does not accommodate any such scale. The absence of the length scale creates several discrepancies in the predictions of mechanical responses, for example, infinite stress fields near crack tips

or nondispersive wave behavior (constant wave speed, independent of frequency). This occurs in classical elasticity, according to which Rayleigh waves propagating on the surface of a semiinfinite isotropic elastic space are nondispersive in nature [Love 1944], whereas experiments and the atomic theory of lattices predict otherwise. These anomalies indicate the limitations of the classical theory of elasticity and stress the need for molecular dynamics (MD)-based simulations. However, modern practical problems are still intractable for MD-based analysis, even if the highest computing capabilities are at disposal. Hence, refinement of the existing continuum theory for the purpose of more realistic predictions seems to be the only viable alternative. Several attempts have been made so far in this direction, for example, the nonlocal theory of elasticity [Eringen 1972; 1976; 1983; Eringen and Edelen 1972], where the objective is always to modify the stress gradient term in the governing momentum equilibrium equations so that the long-range effects are taken into account. The nonlocal theory generates a singular perturbed partial differential equation. In this work, the nonlocal theory of Eringen is used to develop wave solutions for 2D nanostructures such as graphene. However, in this work, the main concern is the issues involved in wave propagation analysis in the domain of nonlocal elasticity.

One important outcome of the nonlocal elasticity is the realistic prediction of the dispersion curve, that is, the frequency-wavenumber/wavevector relation. As shown in [Eringen 1983], the dispersion relation

$$\frac{\omega}{C_1 k} = \left(1 + (e_0 a)^2 k^2\right)^{-1/2}, \tag{1}$$

where $e_0 a$ is the nonlocality parameter, closely matches with the Born–Karman model dispersion

$$\frac{\omega a}{C_1} = 2 \sin\left(\frac{ka}{2}\right) \tag{2}$$

when $e_0 = 0.39$ is considered. However, among the two natural conditions at the midpoint and end of the first Brillouin zone:

$$\left.\frac{d\omega}{dk}\right|_{k=0} = C_1, \quad \left.\frac{d\omega}{dk}\right|_{k=\frac{\pi}{a}} = 0, \tag{3}$$

these relations satisfy only the first one. It has been suggested that two-parameter approximation of the kernel function will give better results. This is reiterated in [Lazar et al. 2006], that a one-parameter (only $e_0 a$) nonlocal kernel will never be able to model the lattice dynamics relation and it is necessary to use the bi-Helmholtz type equation with two different coefficients of nonlocality to satisfy all the boundary conditions.

The simple forms of the group and phase velocities that exist for isotropic materials allow us to tune the nonlocality parameters so that the lattice dispersion relation is matched. Further, by virtue of the Helmholtz decomposition, only the 1D Brillouin zone needs to be handled. Although the general form of the boundary conditions, that is, group speed is equal to phase speed (at $k = 0$) or zero (at $k = \pi/a$), is still applicable, the expressions are difficult to handle. This is because the Brillouin zone is really a 2D region where four boundary conditions are involved.

Wave propagation in GSs has been a topic of great interest in the nanomechanics of GSs, where the equivalent continuum models are widely used. In this manuscript, we examine this issue by incorporating the nonlocal theory into the classical beam model. The influence of the nonlocal effects has been investigated in detail. The results are qualitatively different from those obtained based on the local beam

theory and thus are important for the development of GS-based nanodevices. The present work is an extension of [Sakhaee-Pour and Ahmadian 2008], in which we studied ultrasonic wave propagation in GS using nonlocal elasticity theory incorporating small-scale effects. The graphene was considered as free standing. In the present work, the unstable graphene is made stable by resting it on substrate. The substrate is assumed and modeled as an elastic medium. The present modeling and results can provide useful guidance for the design of next-generation nanodevices where graphene-based composites act as major elements. For a given nanostructure, the nonlocal small scale coefficient can be obtained by matching the results from MD simulations and the nonlocal elasticity calculations. At that value of the nonlocal scale coefficient, the waves will propagate in the nanostructure at that cut-off frequency. In the present paper, different values of e_0a are used. One can get the exact e_0a for a given GS by matching the MD simulation results of graphene with the results presented in this paper.

In the literature, there is no work on ultrasonic wave propagation in GSs with or without the effects of an elastic matrix. In the present paper, a nonlocal elasticity theory is used for analyzing ultrasonic wave propagation in GSs embedded in an elastic matrix. The present paper is organized as follows. In Section 2, Eringen's nonlocal elasticity theory is explained. In Section 3, the nonlocal governing partial differential equations are given for the graphene-elastic matrix system. Then ultrasonic wave propagation in graphene is carried out. Explicit expressions for the wavenumbers and group/phase speeds for the first three modes (in-plane-longitudinal, lateral, and flexural) of the wave are derived. The wave dispersion results are shown with and without elastic matrix effects. We also show that the flexural wave in graphene is highly affected by the presence of the elastic matrix. In Section 4, some important results are discussed in the context of the effects of nonlocality and the substrate. Finally, the paper ends with some important observations and conclusions.

2. Mathematical formulation

2.1. ***A review of the theory of nonlocal elasticity.*** The theory of nonlocal elasticity [Eringen 1972; 1976; 1983; Eringen and Edelen 1972] accommodates an equivalent effect due to nearest neighbor interaction and beyond the single lattice in the sense of lattice average stress and strain. This model considers that the stress state at a reference point $\mathbf{x}$ in the body is regarded to be dependent not only on the strain state at $\mathbf{x}$ but also on the strain states at all other points $\mathbf{x}'$ of the body. This is in accordance with the atomic theory of lattice dynamics and experimental observations on phonon dispersion. The most general form of the constitutive relation in the nonlocal elasticity-type representation involves an integral over the entire region of interest. The integral contains a nonlocal kernel function, which describes the relative influences of the strains at various locations on the stress at a given location. For nonlocal linear elastic solids, the equations of motion have the form

$$t_{ij,j} + f_i = \rho \ddot{u}_i, \tag{4}$$

where ρ and f_i are, respectively, the mass density and the body (and/or applied) forces; u_i is the displacement vector; and t_{ij} is the stress tensor of the nonlocal elasticity defined by

$$t_{ij}(\mathbf{X}) = \int_V \alpha(|\mathbf{X}' - \mathbf{X}|)\sigma_{ij}(\mathbf{X}')\, dv(\mathbf{X}'), \tag{5}$$

in which $\mathbf{X}$ is a reference point in the body; $\alpha(|\mathbf{X}'-\mathbf{X}|)$ is the nonlocal kernel function; and σ_{ij} is the local stress tensor of classical elasticity theory at any point $\mathbf{X}'$ in the body and satisfies the constitutive relations

$$\sigma_{ij} = c_{ijkl}\varepsilon_{kl}, \quad \varepsilon_{kl} = 0.5(u_{k,l} + u_{l,k}), \tag{6}$$

for a general elastic material, in which c_{ijkl} are the elastic modulus components with the symmetry properties $c_{ijkl} = c_{jikl} = c_{ijlk} = c_{klij}$, and ε_{kl} is the strain tensor. We stress that the boundary conditions involving tractions are based on the nonlocal stress tensor t_{ij} and not on the local stress tensor σ_{ij}.

The properties of the nonlocal kernel $\alpha(|\mathbf{X}'-\mathbf{X}|)$ have been discussed in detail in [Eringen 1983]. When $\alpha(|\mathbf{X}|)$ takes on a Green's function of a linear differential operator $\mathscr{L}$, that is,

$$\mathscr{L}\alpha(|\mathbf{X}'-\mathbf{X}|) = \delta(|\mathbf{X}'-\mathbf{X}|), \tag{7}$$

the nonlocal constitutive relation (5) is reduced to the differential equation

$$\mathscr{L}t_{ij} = \sigma_{ij} \tag{8}$$

and the integro-partial differential equation (4) is correspondingly reduced to the partial differential equation

$$\sigma_{ij} + \mathscr{L}(f_i - \rho\ddot{u}_i) = 0. \tag{9}$$

By matching the dispersion curves with lattice models, Eringen [1972; 1983; Eringen and Edelen 1972] proposed a nonlocal model with the linear differential operator $\mathscr{L}$ defined by

$$\mathscr{L} = 1 - (e_0 a)^2\nabla^2, \tag{10}$$

where a is an internal characteristic length (lattice parameter, granular size, or molecular diameter) and e_0 is a constant appropriate to each material for adjusting the model to match some reliable results by experiments or other theories. Therefore, according to (6), (8), and (10), the constitutive relations may be simplified to

$$\big(1 - (e_0 a)^2\nabla^2\big)t_{ij} = \sigma_{ij} = c_{ijkl}\varepsilon_{kl}. \tag{11}$$

For simplicity and to avoid solving integro-partial differential equations, the nonlocal elasticity model, defined by the relations (8)–(11), has been widely adopted for tackling various problems of linear elasticity and micro/nanostructural mechanics.

Generally used 3D and 2D nonlocal kernel functions are given the following equations, respectively,

$$\alpha(|\mathbf{X}|) = \frac{1}{4\pi\ell^2\tau^2|\mathbf{X}|}e^{-|\mathbf{X}|/\ell\tau}, \quad \alpha(|\mathbf{X}|) = \frac{1}{2\pi\ell^2\tau^2}K_0\Big(\frac{|\mathbf{X}|}{\ell\tau}\Big), \tag{12}$$

where $\tau = g/\ell$, K_0 is the modified Bessel function, and ℓ is a characteristic length of the considered structure.

Eringen [1983] proposed $e_0 = 0.39$ by the matching of the dispersion curves via nonlocal theory for plane waves and the Born-Karman model of lattice dynamics applied at the Brillouin zone boundary ($k = \pi/a$), where a is the distance between atoms and k is the wavenumber in the phonon analysis. On the other hand, Eringen and Edelen [1972] proposed $e_0 = 0.31$ for Rayleigh surface waves via nonlocal continuum mechanics and lattice dynamics. In the present paper, we assume that $e_0 = 0.39$ for analyzing ultrasonic wave propagation in an embedded monolayer graphene.

3. Ultrasonic wave characteristics of graphene embedded in an elastic matrix

3.1. ***Derivation of nonlocal governing partial differential equations of motion.*** In this section, we will derive the nonlocal governing differential equations of motion of the graphene-elastic substrate system.

For the present analysis we consider a single graphene layer resting on an elastic substrate (see Figure 1). This system is modeled as an one-atom thick nanoplate on distributed elastic springs. The displacement field is assumed as

$$\begin{aligned} u(x, y, z, t) &= u^o(x, y, t) - z\frac{\partial w}{\partial x}, \\ v(x, y, z, t) &= v^o(x, y, t) - z\frac{\partial w}{\partial y}, \\ w(x, y, z, t) &= w(x, y, t), \end{aligned} \tag{13}$$

where $u^o(x, y, t)$, $v^o(x, y, t)$, and $w(x, y, t)$ are the axial (in-plane-longitudinal and lateral) and transverse displacements, respectively, along the midplane as shown in Figure 1. The midplane of the plate is at $z = 0$. The associated nonzero strains are obtained as

$$\begin{Bmatrix} \varepsilon_{xx} \\ \varepsilon_{yy} \\ \varepsilon_{xy} \end{Bmatrix} = \begin{Bmatrix} \dfrac{\partial u^o}{\partial x} \\ \dfrac{\partial v^o}{\partial y} \\ \dfrac{\partial u^o}{\partial y} + \dfrac{\partial v^o}{\partial x} \end{Bmatrix} + \begin{Bmatrix} -\dfrac{\partial^2 w}{\partial x^2} \\ -\dfrac{\partial^2 w}{\partial y^2} \\ -2\dfrac{\partial^2 w}{\partial x \partial y} \end{Bmatrix}, \tag{14}$$

where ε_{xx} and ε_{yy} are the normal strains in the x and y directions, respectively, while, ε_{xy} is the in-plane shear strain.

The nonlocal constitutive relation for isotropic materials is given as

$$\begin{Bmatrix} \sigma_{xx} \\ \sigma_{yy} \\ \sigma_{xy} \end{Bmatrix} - (e_0 a)^2 \left(\frac{\partial^2}{\partial x^2} + \frac{\partial^2}{\partial y^2} \right) \begin{Bmatrix} \sigma_{xx} \\ \sigma_{yy} \\ \sigma_{xy} \end{Bmatrix} = \begin{bmatrix} C_{11} & \nu C_{11} & 0 \\ \nu C_{22} & C_{22} & 0 \\ 0 & 0 & C_{66} \end{bmatrix} \begin{Bmatrix} \varepsilon_{xx} \\ \varepsilon_{yy} \\ \varepsilon_{xy} \end{Bmatrix}, \tag{15}$$

where σ_{xx} and σ_{yy} are the normal stresses in the x and y directions, respectively, and σ_{xy} is the in-plane shear stress. For the case of an isotropic plate, the expressions for C_{ij} in terms of the Young's modulus E and Poisson's ratio ν are given as $C_{11} = C_{22} = E/(1 - \nu^2)$ and $C_{66} = E/(2(1 + \nu))$.

The total strain energy (Π) and kinetic energy (Γ) are calculated as

$$\Pi = \frac{1}{2} \int_{-h/2}^{+h/2} \int_A (\sigma_{xx}\varepsilon_{xx} + \sigma_{yy}\varepsilon_{yy} + \sigma_{xy}\varepsilon_{xy} + 2K^{\text{elastic}} w^2)\, dz\, dA, \tag{16}$$

$$\Gamma = \frac{1}{2} \int_{-h/2}^{+h/2} \int_A \rho(\dot{u}^2 + \dot{v}^2 + \dot{w}^2)\, dz\, dA. \tag{17}$$

Substituting (14) and (15) in (16) and (17) and using Hamilton's principle,

$$\int_{t_1}^{t_2} (\delta\Pi - \delta\Gamma)\, dt = 0, \tag{18}$$

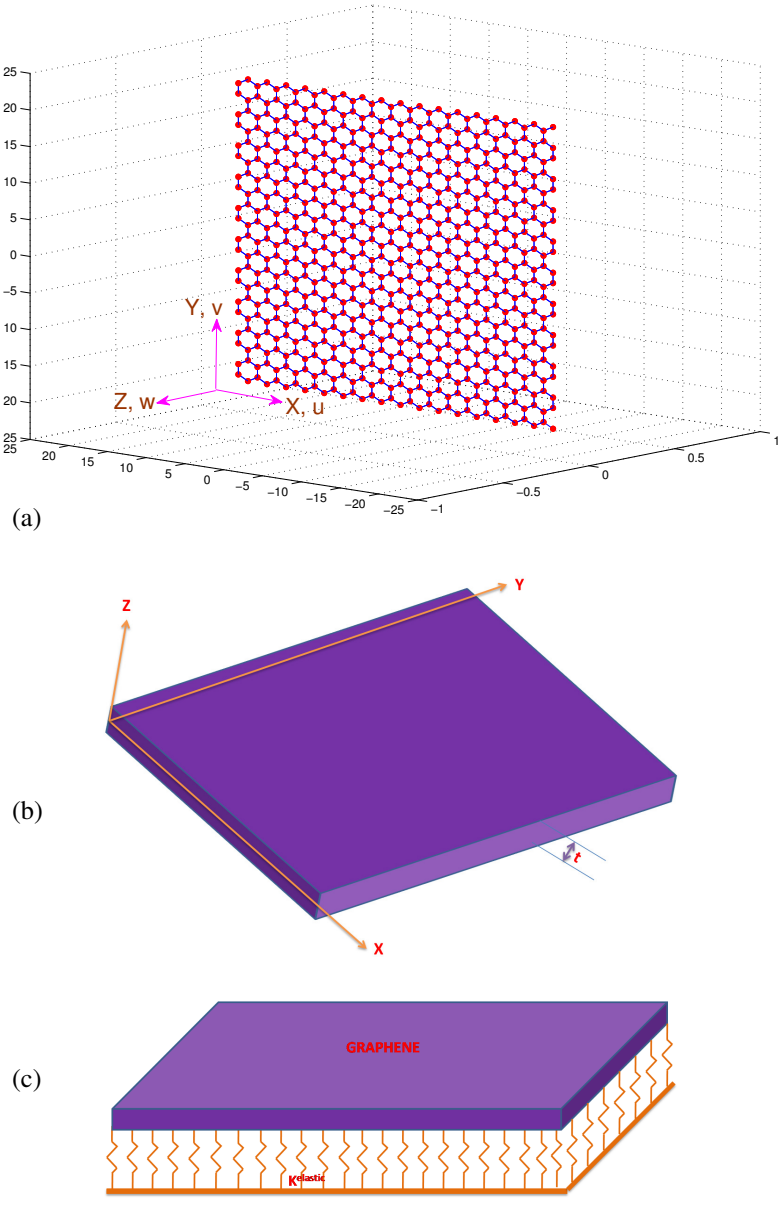

Figure 1. Single-layered GS: (a) discrete model (a monolayer graphene of 40 Å × 40 Å, consisting of 680 carbon atoms arranged in hexagonal array), (b) equivalent continuum model, and (c) continuum equivalent model of monolayer graphene embedded in an elastic medium, where K^{elastic} denotes the modulus parameter of the surrounding medium.

the minimization of the strain and kinetic energies with respect to the three degrees of freedom (u^o, v^o, w) will give three governing partial differential equations for the assumed system (graphene embedded in

matrix) as

$$\delta u^o: \quad -J_0\frac{\partial^2 u^o}{\partial t^2}+J_0(e_0a)^2\left(\frac{\partial^4 u^o}{\partial x^2\partial t^2}+\frac{\partial^4 u^o}{\partial y^2\partial t^2}\right)-I_0\left(C_{11}\frac{\partial^2 u^o}{\partial x^2}+C_{66}\frac{\partial^2 u^o}{\partial y^2}\right)+I_0(C_{12}+C_{66})\frac{\partial^2 v^o}{\partial x\,\partial y}$$
$$+J_1\frac{\partial^3 w}{\partial x\,\partial t^2}-J_1(e_0a)^2\left(\frac{\partial^5 w}{\partial x^3\partial t^2}+\frac{\partial^5 w}{\partial x\,\partial y^2\partial t^2}\right)-C_{11}I_1\frac{\partial^3 w}{\partial x^3}-I_1(C_{12}+2C_{66})\frac{\partial^3 w}{\partial x\,\partial y^2}=0, \quad (19)$$

$$\delta v^o: \quad -J_0\frac{\partial^2 v^o}{\partial t^2}+J_0(e_0a)^2\left(\frac{\partial^4 v^o}{\partial x^2\partial t^2}+\frac{\partial^4 v^o}{\partial y^2\partial t^2}\right)-I_0\left(C_{22}\frac{\partial^2 v^o}{\partial y^2}+C_{66}\frac{\partial^2 v^o}{\partial x^2}\right)+I_0(C_{12}+C_{66})\frac{\partial^2 u^o}{\partial x\,\partial y}$$
$$+J_1\frac{\partial^3 w}{\partial y\,\partial t^2}-J_1(e_0a)^2\left(\frac{\partial^5 w}{\partial x^2\partial y\partial t^2}+\frac{\partial^5 w}{\partial y^3\partial t^2}\right)-C_{22}I_1\frac{\partial^3 w}{\partial y^3}-I_1(C_{12}+2C_{66})\frac{\partial^3 w}{\partial x^2\partial y}=0, \quad (20)$$

$$\delta w: \quad -J_0\frac{\partial^2 w}{\partial t^2}+J_2\left(\frac{\partial^4 w}{\partial x^2\partial t^2}+\frac{\partial^4 w}{\partial y^2\partial t^2}\right)+J_0(e_0a)^2\left(\frac{\partial^4 w}{\partial x^2\partial t^2}+\frac{\partial^4 w}{\partial y^2\partial t^2}\right)$$
$$-J_2(e_0a)^2\left(\frac{\partial^6 w}{\partial x^4\partial t^2}+2\frac{\partial^6 w}{\partial x^2\partial y^2\partial t^2}+\frac{\partial^6 w}{\partial y^4\partial t^2}\right)+2K^{\text{elastic}}(e_0a)^2\left(\frac{\partial^2 w}{\partial x^2}+\frac{\partial^2 w}{\partial y^2}\right)$$
$$-2K^{\text{elastic}}w-I_2\left(C_{11}\frac{\partial^4 w}{\partial x^4}+C_{22}\frac{\partial^4 w}{\partial y^4}\right)-2I_2(C_{11}+2C_{66})\frac{\partial^4 w}{\partial x^2\partial y^2}-J_1\frac{\partial^3 u^o}{\partial x\,\partial t^2}$$
$$+J_1(e_0a)^2\left(\frac{\partial^5 u^o}{\partial x^3\partial t^2}+\frac{\partial^5 u^o}{\partial x\,\partial y^2\partial t^2}\right)+C_{11}I_1\frac{\partial^3 u^o}{\partial x^3}+I_1(C_{12}+2C_{66})\frac{\partial^3 u^o}{\partial x\,\partial y^2}$$
$$-J_1\frac{\partial^3 v^o}{\partial y\,\partial t^2}+J_1(e_0a)^2\left(\frac{\partial^5 v^o}{\partial x^2\partial y\partial t^2}+\frac{\partial^5 v^o}{\partial y^3\partial t^2}\right)+I_1(C_{12}+2C_{66})\frac{\partial^3 v^o}{\partial x^2\partial y}+C_{22}I_1\frac{\partial^3 v^o}{\partial y^3}=0, \quad (21)$$

where K^{elastic} is the force constant of the bond between the GS and the elastic matrix and

$$I_p=\int_{-h/2}^{h/2}z^p\,dz, \quad J_p=\int_{-h/2}^{h/2}\rho z^p\,dz, \quad p=0,1,2. \quad (22)$$

If the nonlocal scaling parameter e_0a is zero, then the above three governing differential equations of motion become classical governing equations.

3.2. ***Ultrasonic wave dispersion and band gap analysis.*** For harmonic wave propagation in a GS, the displacement field can be written in complex form as [Zhou and Li 2001]

$$\begin{aligned} u^o(x,y,t)&=\hat{u}e^{-jk_xx}e^{-jk_yy}e^{j\omega t},\\ v^o(x,y,t)&=\hat{v}e^{-jk_xx}e^{-jk_yy}e^{j\omega t},\\ w^o(x,y,t)&=\hat{w}e^{-jk_xx}e^{-jk_yy}e^{j\omega t}, \end{aligned} \quad (23)$$

where $\hat{u}$, $\hat{v}$, and $\hat{w}$ are the frequency amplitudes, k_x and k_y are the wavenumbers in the x and y-directions, respectively, ω is the frequency of the wave motion, and $j=\sqrt{-1}$.

The nonlocal governing partial differential equations of the graphene embedded in an elastic matrix model are given in (19)–(21). The next step is to analyze the ultrasonic type of wave propagation in these GSs. For this, substitute the displacement assumed as a harmonic type given in (23) in the governing

partial differential equations of the graphene and write the resultant equations in matrix form as (for nontrivial solutions of $\hat{u}$, $\hat{v}$, and $\hat{w}$)

$$\mathbf{S}_4 k_x^4 + \mathbf{S}_3 k_x^3 + \mathbf{S}_2 k_x^2 + \mathbf{S}_1 k_x + \mathbf{S}_0 = 0, \tag{24}$$

where

$$\begin{aligned}
\mathbf{S}_4 &= \begin{bmatrix} 0 & 0 & 0 \\ 0 & 0 & 0 \\ 0 & 0 & J_2(e_0a)^2\omega^2 - C_{11}I_2 \end{bmatrix}, \\
\mathbf{S}_3 &= \begin{bmatrix} 0 & 0 & jJ_1\omega^2(e_0a)^2 - jC_{11}I_1 \\ 0 & 0 & 0 \\ -jJ_1\omega^2(e_0a)^2 + jC_{11}I_1 & 0 & 0 \end{bmatrix}, \\
\mathbf{S}_2 &= \begin{bmatrix} J_0\omega^2(e_0a)^2 - C_{11}I_0 & 0 & 0 \\ 0 & J_0\omega^2(e_0a)^2 - C_{66}I_0 & S_2^{(23)} \\ 0 & S_2^{(32)} & S_2^{(33)} \end{bmatrix}, \\
\mathbf{S}_1 &= \begin{bmatrix} 0 & -(C_{11}+C_{66})I_0k_y & S_1^{(13)} \\ -(C_{11}+C_{66})I_0k_y & 0 & 0 \\ S_1^{(31)} & 0 & 0 \end{bmatrix}, \\
\mathbf{S}_0 &= \begin{bmatrix} S_0^{(11)} & 0 & 0 \\ 0 & S_0^{(22)} & S_0^{(23)} \\ 0 & S_0^{(32)} & S_0^{(33)} \end{bmatrix},
\end{aligned} \tag{25}$$

where the elements $S_r^{(pq)}$ ($p, q = 1, 2, 3$ and $r = 0, 1, 2$) are given in the Appendix.

Equation (24) is in the form of polynomial eigenvalue problem in wavenumber k_x and is solved for the wavenumbers. This method is very generalized and efficient. The resulting wavenumbers are functions of wave frequency and are shown in Figures 2 and 3, obtained from both local and nonlocal elasticities, with and without the effect of the elastic matrix, respectively. The figures also show the effect of the substrate on the ultrasonic wave characteristics of graphene at $k_y = 0$, 2, and 5 nm^{-1}. In the wavenumber dispersion curves, the frequency at which the imaginary part of the wavenumber becomes real is called the frequency band gap region (0 to ω_c). The expressions for the frequency band gap are obtained by setting $k_x = 0$ in dispersion relation, (24). For the present case of a polynomial eigenvalue problem (PEP) one can solve $\mathrm{Det}(\mathbf{S}_0) = 0$ as

$$\omega_c^{\text{in-plane}} = k_y \sqrt{\frac{I_0 C_{66}}{J_0(1 + (e_0a)^2 k_y^2)}}, \quad \omega_c^{\text{flexural}} = \sqrt{\frac{1}{2H_0}\sqrt{H_1 + H_2}}, \tag{26}$$

where H_0, H_1, and H_2 are given in the Appendix.

The frequency band gap ($0 - \omega_c$, cut-off frequency) for all the fundamental modes (longitudinal, lateral, and flexural) for $k_y \neq 0$ in graphene with and without substrate effect. These cut-off frequencies are functions of the material properties of graphene, the y-direction wavenumber k_y, and the nonlocal scaling parameter e_0a.

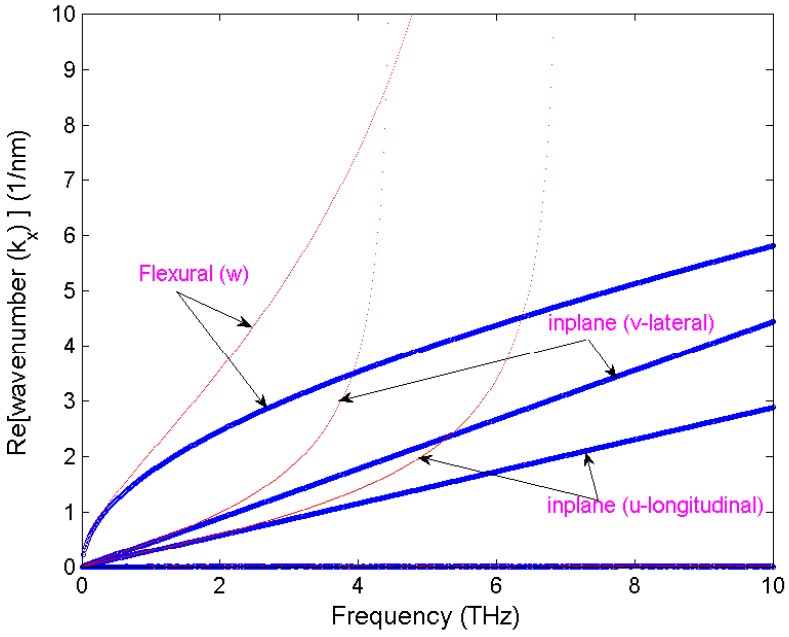

Figure 2. Wavenumber dispersion with wave frequency in the GS without considering the elastic matrix obtained from the local and nonlocal elasticity; here the y-directional wavenumber $k_y = 0$ and the nonlocal scaling parameter is $e_0 a = 0.5$ nm.

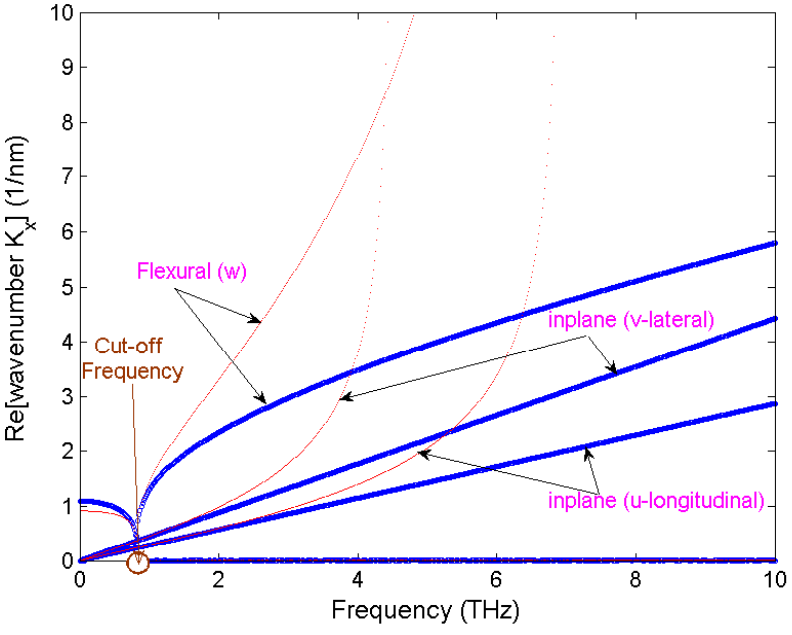

Figure 3. Wavenumber dispersion with wave frequency in the GS with considering the elastic matrix obtained from the local and nonlocal elasticity; here the y-directional wavenumber $k_y = 0$ and the nonlocal scaling parameter is $e_0 a = 0.5$ nm.

In the present work, it has been observed that the nonlocal scale parameter introduces a certain band gap region in the in-plane and flexural wave modes where no wave propagation occurs. This is manifest in the wavenumber plots as the region where the wavenumber tends to infinity or the wave speed tends to zero. The frequency at which this phenomenon occurs is called the *escape frequency*. The escape frequencies are obtained by solving $\mathrm{Det}(\mathbf{S}_4) = 0$. It can be noticed that $\mathbf{S}_4$ is singular, thus the lambda matrix $\Phi(k_x) = \mathbf{S}_4 k_x^4 + \mathbf{S}_3 k_x^3 + \mathbf{S}_2 k_x^2 + \mathbf{S}_1 k_x + \mathbf{S}_0$ is not regular [Fleck and Hutchinson 1997] and admits infinite eigenvalues [Yang et al. 2002]. So, the escape frequencies of these fundamental wavemodes can also obtained by substituting $k_x \to \infty$ in the expanded dispersion relation, (24), that is, a polynomial in k_x, and solving for the frequencies. The obtained escape frequencies of these three fundamental wave modes are

$$\omega_e^{\text{longitudinal}} = \frac{1}{e_0 a}\sqrt{\frac{C_{11} I_2}{J_2}}, \quad \omega_e^{\text{lateral}} = \frac{1}{e_0 a}\sqrt{\frac{C_{66} I_0}{J_0}}, \quad \omega_e^{\text{flexural}} = \frac{1}{e_0 a}\sqrt{\frac{C_{11} I_0}{J_0}}. \tag{27}$$

Here the suffix e represents the escape frequency. It can be seen that the escape frequencies are purely functions of the nonlocal scaling parameter and are not affected by the dimensions of the GS. Also, the escape frequencies are independent of the effect of the elastic matrix.

The wave speeds (phase speed $C_p = \omega/k_x$ and group speed $C_g = \partial\omega/\partial k_x$) can be computed from (24).

We differentiate the PEP with respect to wave frequency, to get a PEP in terms of group speed as

$$\mathbf{G}_1 C_g + \mathbf{G}_0 = 0, \tag{28}$$

where

$$\begin{aligned} \mathbf{G}_1 &= \left[k_x^4 \frac{\partial \mathbf{S}_4}{\partial \omega} + k_x^3 \frac{\partial \mathbf{S}_3}{\partial \omega} + k_x^2 \frac{\partial \mathbf{S}_2}{\partial \omega} + k_x \frac{\partial \mathbf{S}_1}{\partial \omega} + \frac{\partial \mathbf{S}_0}{\partial \omega} \right], \\ \mathbf{G}_0 &= 4\mathbf{S}_4 k_x^3 + 3\mathbf{S}_3 k_x^2 + 2\mathbf{S}_2 k_x + \mathbf{S}_1, \end{aligned} \tag{29}$$

where $C_g = (\partial\omega/\partial k_x)$ is the group speed of waves in the graphene and the matrices $\mathbf{S}_4$, $\mathbf{S}_3$, $\mathbf{S}_2$, $\mathbf{S_1}$, and $\mathbf{S}_0$ are given in (25). This is also a PEP, and one can solve it for the group speeds (as a function of wave frequency, wavenumbers, and nonlocal scaling parameter) of respective modes (that is, for in-plane-u, v, and flexural-w) of the graphene.

We will discuss the phase speed dispersion with wave frequency, as shown in Figures 4–7, obtained from both local and nonlocal elasticity and taken with and without the effect of the elastic matrix. The phase speed dispersion shown is for both with and without the elastic matrix effects at $k_y = 0$ and $2\,\mathrm{nm}^{-1}$.

3.3. ***Numerical experiments, results and discussion.*** For the present analysis, the Young's modulus of the graphene is taken as 1.06 TPa, the density is $2300\,\mathrm{kg/m}^3$, and the size 40×40 Å. The stiffness of the bond between the graphene and the matrix is $0.2694\,\mathrm{N/m}$ and this has to be divided by the number of atoms per unit area of the graphene (38×10^{18}).

The wavenumber dispersion with wave frequency in the graphene without and with the elastic matrix, respectively, are shown in Figures 2 and 3, obtained from both the local and nonlocal elasticity. Figure 2 shows the wavenumber dispersion obtained from the local and nonlocal elasticity theory (where $e_0 a = 0$ and $e_0 a = 0.5\,\mathrm{nm}$). Figures 2 and 3 are shown for $k_y = 0$ (which represents 1D wave propagation). In Figures 8 and 9 were have $k_y = 2\,\mathrm{nm}^{-1}$. The frequency band gap of the flexural waves is small

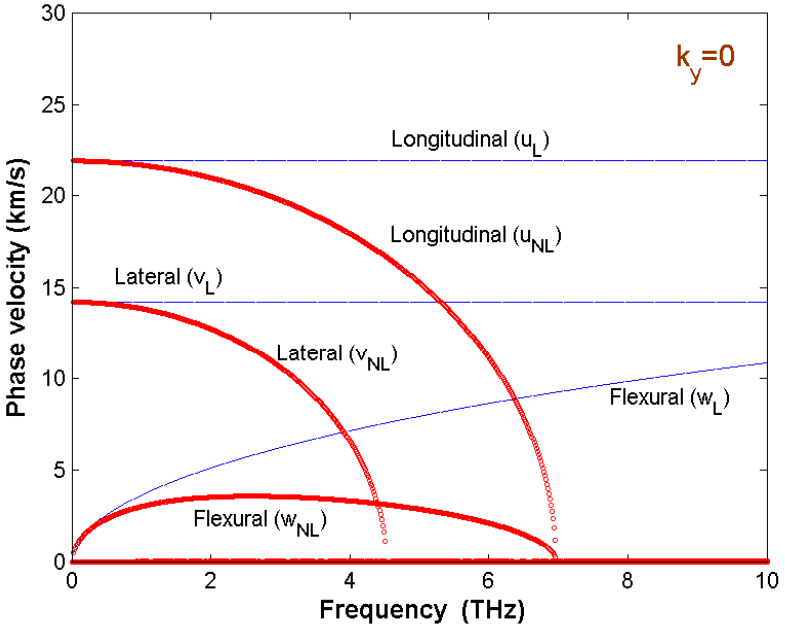

Figure 4. Phase velocity dispersion with wave frequency in the GS without considering the elastic matrix obtained from the local and nonlocal elasticity; here the y-directional wavenumber $k_y = 0$ and the nonlocal scaling parameter is $e_0a = 0.5$ nm.

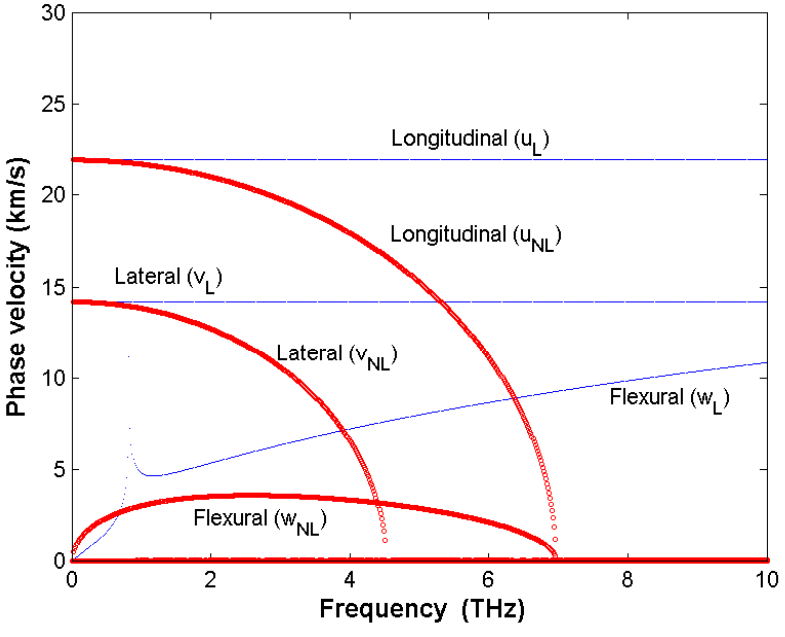

Figure 5. Phase velocity dispersion with wave frequency in the GS with considering the elastic matrix obtained from the local and nonlocal elasticity; here the y-directional wavenumber $k_y = 0$ and the nonlocal scaling parameter is $e_0a = 0.5$ nm.

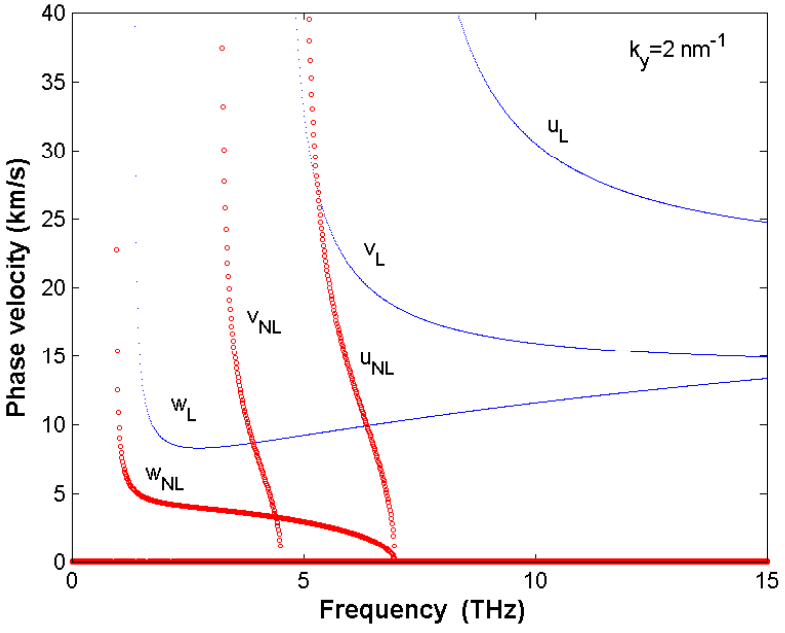

Figure 6. Phase velocity dispersion with wave frequency in the GS without considering the elastic matrix obtained from the local and nonlocal elasticity; here the y-directional wavenumber $k_y = 2\,\mathrm{nm}^{-1}$ and the nonlocal scaling parameter is $e_0 a = 0.5\,\mathrm{nm}$.

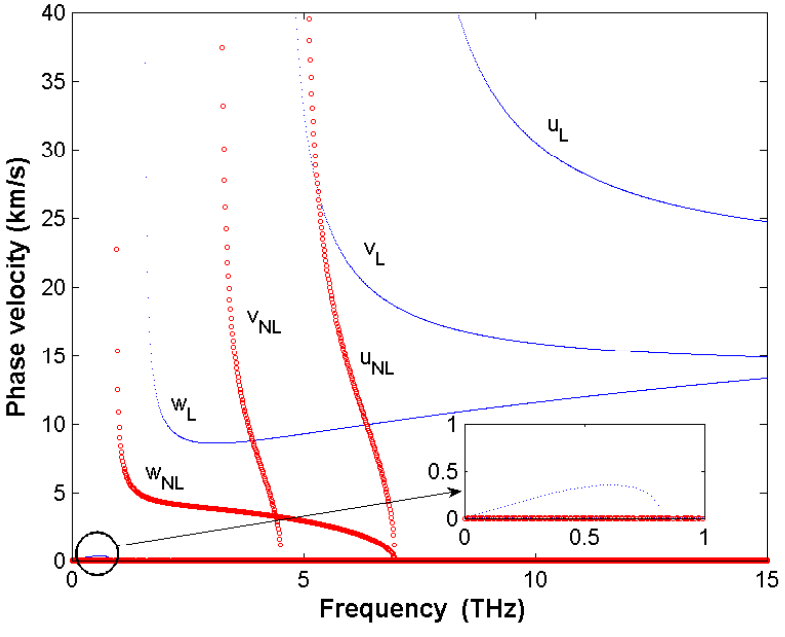

Figure 7. Phase velocity dispersion with wave frequency in the GS with considering the elastic matrix obtained from the local and nonlocal elasticity; here the y-directional wavenumber $k_y = 2\,\mathrm{nm}^{-1}$ and the nonlocal scaling parameter is $e_0 a = 0.5\,\mathrm{nm}$.

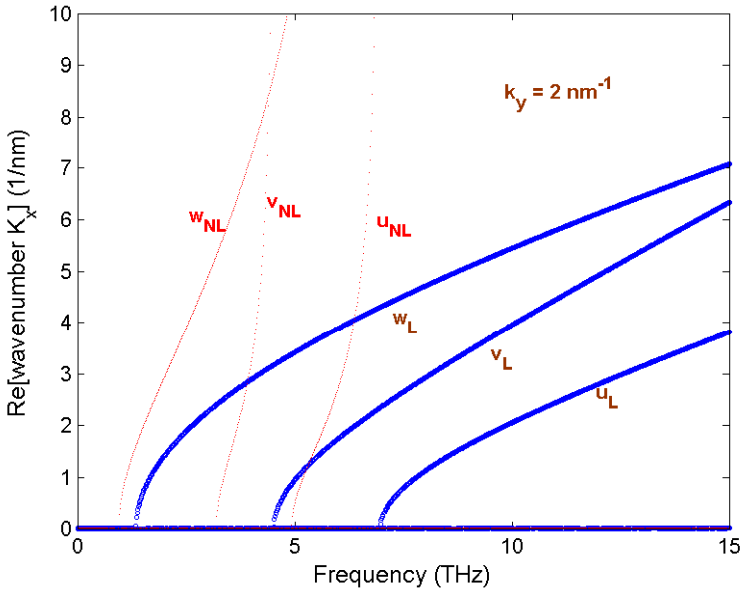

Figure 8. Wavenumber dispersion with wave frequency in the GS without considering the elastic matrix obtained from the local and nonlocal elasticity; here the y-directional wavenumber $k_y = 2\,\text{nm}^{-1}$ and the nonlocal scaling parameter is $e_0a = 0.5\,\text{nm}$.

as compared to that of the longitudinal and lateral (in-plane) waves for the case without the elastic matrix effect. As the y-directional wavenumber k_y increases the frequency band gap of all the three fundamental modes increases. If we consider the elastic matrix effect, then the flexural wave starts propagating after a high-frequency band gap as compared to that of no matrix effect. The local elasticity shows a linear variation of the axial wavenumbers with frequency for $k_y = 0$, that is, the longitudinal and lateral wavenumbers are nondispersive in nature. For $k_y = 0$ the flexural wavenumber shows a nonlinear variation at low values of wave frequency; at higher values of wave frequency it varies linearly as shown in Figure 2. As k_y increases all the wavenumbers are dispersive in nature. In Figures 3 and 9 one can observe the matrix effect on flexural waves.

Wavenumber dispersion with frequency for nonlocal elasticity ($e_0a = 0.5\,\text{nm}$) is shown in Figures 2–9. The observations made for local elasticity are still valid for nonlocal elasticity. The only difference is that because of nonlocal elasticity the wavenumbers (for both in-plane and flexural) become highly nonlinear at higher wave frequencies. The frequency band gap variation is the same as we move from local to nonlocal elasticity with and without the elastic matrix effects.

Local elasticity shows that the wave will propagate even at higher frequencies. But nonlocal elasticity predicts that the waves can only propagate up to certain frequencies (called escape frequencies), after which it will stand, that is, there will be no propagation. The wavenumber dispersion curves obtained for nonlocal elasticity are shown up to the nonlocal limit only. The phenomena discussed at the beginning of this paragraph occurs above the nonlocal limit.

Phase speed dispersion with the wave frequency is shown in Figures 4–7 for local and nonlocal elasticity, for y-directional wavenumbers of $k_y = 0$ and $k_y = 2\,\text{nm}^{-1}$. Figure 4 shows that (for $k_y = 0$) the

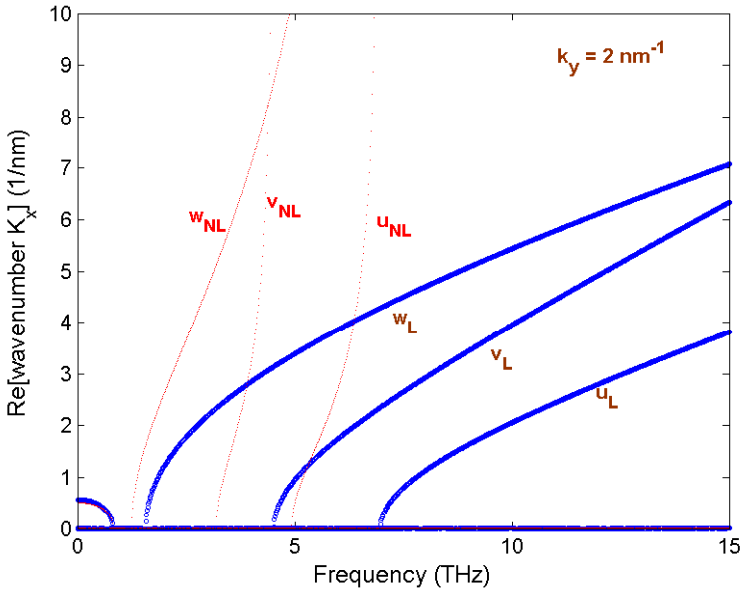

Figure 9. Wavenumber dispersion with wave frequency in the GS with considering the elastic matrix obtained from the local and nonlocal elasticity; here the y-directional wavenumber $k_y = 2\,\mathrm{nm}^{-1}$ and the nonlocal scaling parameter is $e_0a = 0.5\,\mathrm{nm}$.

in-plane (u, v) wave speeds are constant with wave frequency, while flexural wave speeds increase from low frequency, after which they are constant for higher values of wave frequency. The magnitudes of the flexural phase speeds are higher compared to the axial wave group speeds. As k_y increases from 0 to $2\,\mathrm{nm}^{-1}$ the axial/in-plane wave speeds also show a dispersive nature. We can also observe the effect of the elastic matrix on the flexural wave phase speeds.

As we move to nonlocality, the phase speeds of the in-plane and flexural waves stop propagating at certain frequencies as shown in Figures 4–7. The phase speeds of the in-plane waves are the same for with or without the elastic matrix effect. The effect is only on the flexural wave speeds. There are two cut-off frequencies for the flexural waves with substrate effects from nonlocal elasticity. As k_y increases the flexural wave speeds retain the shape shown for local elasticity and the extra frequency band gap also vanishes.

From these results we can observe that only flexural waves are affected by the elastic matrix whether under local or nonlocal elasticity.

The variation of the cut-off frequencies of in-plane and flexural waves is shown in Figures 10 and 11, without and with the elastic matrix effect, respectively, and with y-directional wavenumbers of $k_y = 0, 2$ and $5\,\mathrm{nm}^{-1}$. The figures show that as we increase the nonlocal scaling parameter the cut-off frequencies of all the fundamental wave modes will decrease. For a given e_0a, as we increase the y-directional wavenumber, the cut-off frequencies will increase. Because of the matrix, only the flexural wave mode cut-off frequencies are affected, as can be clearly seen from Figures 10 and 11.

The variation of the escape frequency with the nonlocal scaling parameter is shown in Figure 12. It can be seen that the escape frequencies of the longitudinal and flexural wave modes have equal values, and the latter wave has lower escape frequencies compared to that of longitudinal/flexural waves.

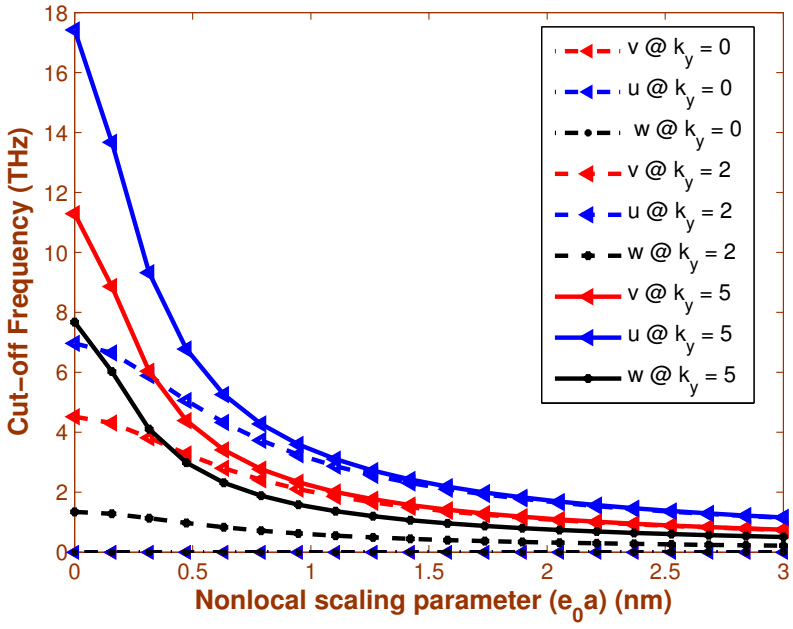

Figure 10. Cut-off frequency variation of longitudinal, lateral, and flexural waves obtained from the local and nonlocal elasticity without considering the effect of the matrix; k_y are in $1/\text{nm}$.

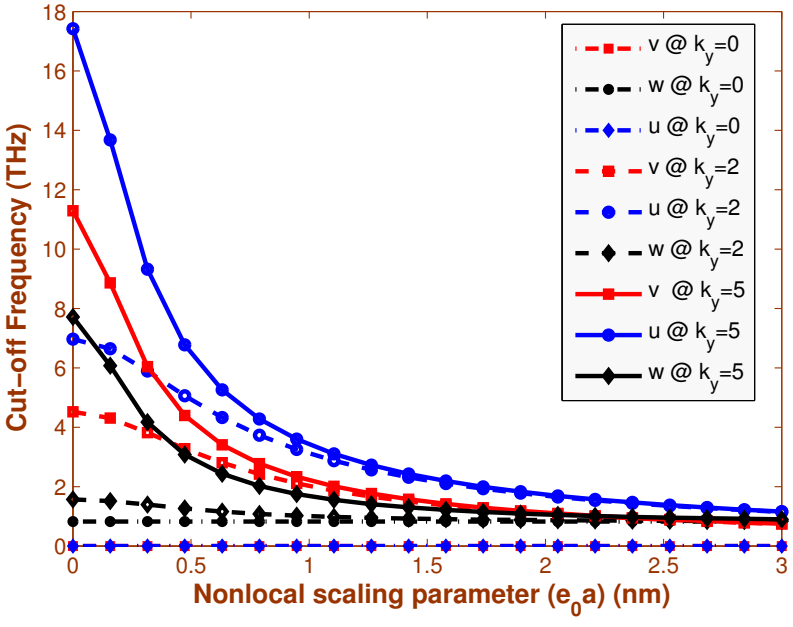

Figure 11. Cut-off frequency variation of longitudinal, lateral, and flexural waves obtained from the local and nonlocal elasticity with considering the effect of the matrix; k_y are in $1/\text{nm}$.

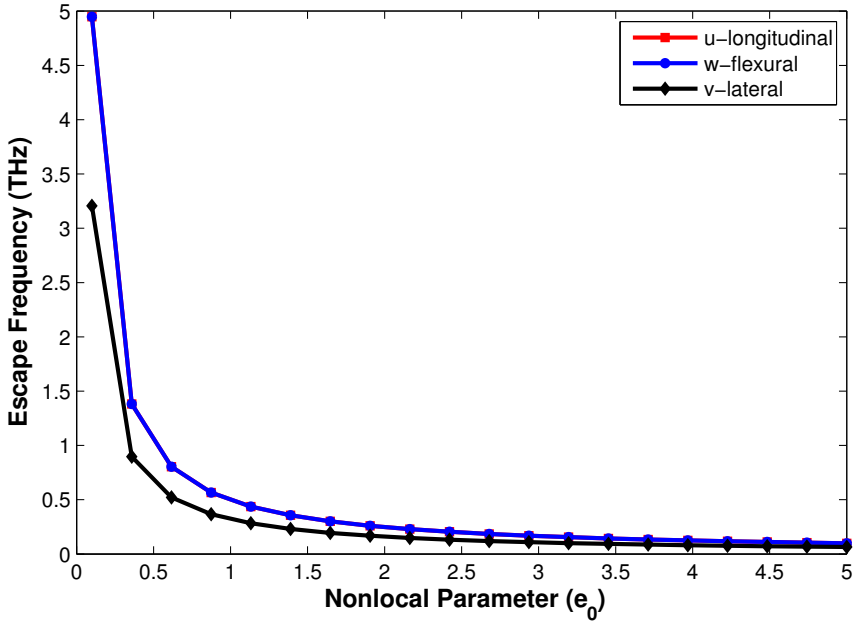

Figure 12. Cut-off frequency variation of longitudinal, lateral, and flexural waves obtained from the local and nonlocal elasticity with considering the effect of the matrix.

4. Conclusion

Ultrasonic wave propagation in a graphene sheet (GS), which is embedded in an elastic medium, was studied using a nonlocal elasticity theory incorporating small-scale effects. The GS was modeled as an one-atom thick isotropic plate and the elastic medium/substrate was modeled as distributed springs. For this model, the nonlocal governing differential equations of motion were derived from the minimization of the total potential energy of the entire system. After that, an ultrasonic type of wave propagation model was also derived. The explicit expressions for the cut-off and escape frequencies were also obtained as functions of the nonlocal scaling parameter and the y-directional wavenumber (k_y). The results of the wave dispersion analysis were shown for both local and nonlocal elasticity. From this analysis we showed that the elastic medium affected only the flexural wave mode in the GS. The present results can provide useful guidance for the design of next-generation nanodevices in which graphene-based composites act as major elements.

Appendix

Some of the elements of the matrices $[S_2]$, $[S_1]$, and $[S_0]$ are given in the following:

$$S_2^{(23)} = jJ_1k_y(e_0a)^2\omega^2 - j(C_{11}+2C_{66})I_1k_y,$$
$$S_2^{(32)} = -jJ_1k_y(e_0a)^2\omega^2 + j(C_{11}+2C_{66})I_1k_y,$$
$$S_2^{(33)} = J_2\omega^2\left(1+(e_0a)^2k_y^2\right) - J_0\omega^2(e_0a)^2 - (C_{11}+2C_{66})I_2k_y^2 - K^{\text{elastic}}(e_0a)^2;$$

$$S_1^{(13)} = jJ_1\omega^2\big(1+(e_0a)^2k_y^2\big) - j(C_{11}+2C_{66})I_1k_y^2,$$
$$S_1^{(31)} = -jJ_1\omega^2\big(1+(e_0a)^2k_y^2\big) + j(C_{11}+2C_{66})I_1k_y^2;$$

$$S_0^{(11)} = J_0\omega^2\big(1+(e_0a)^2k_y^2\big) - C_{66}I_0k_y^2,$$
$$S_0^{(22)} = J_0\omega^2\big(1+(e_0a)^2k_y^2\big) - C_{22}I_0k_y^2,$$
$$S_0^{(23)} = jJ_1k_y\omega^2\big(1+(e_0a)^2k_y^2\big) - jC_{22}I_1k_y^3,$$
$$S_0^{(32)} = -jJ_1k_y\omega^2\big(1+(e_0a)^2k_y^2\big) + jC_{22}I_1k_y^3,$$
$$S_0^{(33)} = J_2\omega^2k_y^2\big(1+(e_0a)^2k_y^2\big) + J_0\omega^2\big(1+(e_0a)^2k_y^2\big) - C_{22}I_2k_y^4 - K^{sub}\big(1+(e_0a)^2k_y^2\big);$$

$$H_0 = (J_0J_2 - J_1^2)k_y^4(e_0a)^2 + J_0^2\big(1+(e_0a)^2k_y^2\big) + (J_0J_2 - J_1^2)k_y^2,$$
$$H_1 = J_0K^{\text{elastic}}\big(1+(e_0a)^2k_y^2\big) + (J_0+J_2)C_{22}I_2k_y^4 + (I_0J_0 - 2I_1J_2)C_{22}k_y^4;$$

$$\begin{aligned}H_2 = {}& [J_0^2(e_0a)^4k_y^4 + 2J_0^2(e_0a)^2k_y^2 + J_0^2]K^{\text{elastic}^2}\big[(2J_0^2I_2 - 2J_0I_0J_2 - 4J_0J_1I_1 + 4J_1^2I_0)C_{22}(e_0a)^2k_y^6\\ &-\big(2J_0^2(e_0a)^2I_0 + 2J_0^2I_2 - 2J_0I_0J_2 - 4J_0J_1I_1 + 4J_1^2I_0\big)C_{22}k_y^4 - 2C_{22}I_0J_0^2k_y^2\big]K^{\text{elastic}}\\ &+[J_0^2I_2^2 + I_0^2J_2^2 - 4J_0I_2J_1I_1 - 2J_0I_2I_0J_2 - 4J_1I_1I_0J_2 + 4J_0J_2I_1^2 + 4J_1^2I_0I_2]C_{22}^2k_y^8\\ &+[4J_0^2I_1^2 - 2J_0^2I_2I_0 - 4I_0J_0J_1I_1 + 2I_0^2J_0J_2]C_{22}^2k_y^6 + I_0^2J_0^2C_{22}^2k_y^4.\end{aligned}$$

References

[Adali 2008] S. Adali, "Variational principles for multi-walled carbon nanotubes undergoing buckling based on nonlocal elasticity theory", *Phys. Lett. A* **372**:35 (2008), 5701–5705.

[Aydogdu 2009a] M. Aydogdu, "Axial vibration of the nanorods with the nonlocal continuum rod model", *Physica E* **41**:5 (2009), 861–864.

[Aydogdu 2009b] M. Aydogdu, "A general nonlocal beam theory: its application to nanobeam bending, buckling and vibration", *Physica E* **41**:9 (2009), 1651–1655.

[Behfar and Naghdabadi 2005] K. Behfar and R. Naghdabadi, "Nanoscale vibrational analysis of a multi-layered graphene sheet embedded in an elastic medium", *Compos. Sci. Technol.* **65**:7–8 (2005), 1159–1164.

[Behfar et al. 2006] K. Behfar, P. Seifi, R. Naghdabadi, and J. Ghanbari, "An analytical approach to determination of bending modulus of a multi-layered graphene sheet", *Thin Solid Films* **496**:2 (2006), 475–480.

[Chen et al. 2004] Y. Chen, J. D. Lee, and A. Eskandarian, "Atomistic viewpoint of the applicability of microcontinuum theories", *Int. J. Solids Struct.* **41**:8 (2004), 2085–2097.

[Dabbousi et al. 1997] B. O. Dabbousi, J. RodriguezViejo, F. V. Mikulec, J. R. Heine, H. Mattoussi, R. Ober, K. F. Jensen, and M. G. Bawendi, "(CdSe) ZnS core-shell quantum dots: synthesis and characterization of a size series of highly luminescent nanocrystallites", *J. Phys. Chem. B* **101** (1997), 9463–9475.

[Duan and Wang 2007] W. H. Duan and C. M. Wang, "Exact solutions for axisymmetric bending of micro/nanoscale circular plates based on nonlocal plate theory", *Nanotechnology* **18**:38 (2007), Article ID #385704.

[Duan et al. 2007] W. H. Duan, C. M. Wang, and Y. Y. Zhang, "Calibration of nonlocal scaling effect parameter for free vibration of carbon nanotubes by molecular dynamics", *J. Appl. Phys.* **101**:2 (2007), Article ID #024305.

[Ece and Aydoydu 2007] M. C. Ece and M. Aydoydu, "Nonlocal elasticity effect on vibration of in-plane loaded double-walled carbon nano-tubes", *Acta Mech.* **190** (2007), 185–195.

[Eringen 1972] A. C. Eringen, "Linear theory of nonlocal elasticity and dispersion of plane waves", *Int. J. Eng. Sci.* **10** (1972), 425–435.

[Eringen 1976] A. C. Eringen, *Continuum physics, IV: Polar and non-local field theories*, Academic Press, New York, 1976.

[Eringen 1983] A. C. Eringen, "On differential equations of nonlocal elasticity and solutions of screw dislocation and surface waves", *J. Appl. Phys.* **54**:9 (1983), 4703–4710.

[Eringen and Edelen 1972] A. C. Eringen and D. G. B. Edelen, "On nonlocal elasticity", *Int. J. Eng. Sci.* **10** (1972), 233–248.

[Fleck and Hutchinson 1997] N. A. Fleck and J. W. Hutchinson, "Strain gradient plasticity", *Adv. Appl. Mech.* **33** (1997), 295–361.

[Geim and Novoselov 2007] A. K. Geim and K. S. Novoselov, "The rise of graphene", *Nat. Mater.* **6**:3 (2007), 183–191.

[Gómez-Navarro et al. 2007] C. Gómez-Navarro, R. T. Weitz, A. M. Bittner, M. Scolari, A. Mews, M. Burghard, and K. Kern, "Electronic transport properties of individual chemically reduced graphene oxide sheets", *Nano Lett.* **7**:11 (2007), 3499–3503.

[Horiuchi et al. 2004] S. Horiuchi, T. Gotou, and M. Fujiwara, "Single graphene sheet detected in a carbon nanofilm", *Appl. Phys. Lett.* **84**:13 (2004), 2403–2405.

[Kroto et al. 1985] H. W. Kroto, J. R. Heath, S. C. O'Brien, R. F. Curl, and R. E. Smalley, "C_{60}: Buckminsterfullerene", *Nature* **318**:6042 (1985), 162–163.

[Kumar et al. 2008] D. Kumar, C. Heinrich, and A. M. Waas, "Buckling analysis of carbon nanotubes modeled using nonlocal continuum theories", *J. Appl. Phys.* **103**:7 (2008), Article ID #073521.

[Lazar et al. 2006] M. Lazar, G. A. Maugin, and E. C. Aifantis, "On a theory of nonlocal elasticity of bi-Helmholtz type and some applications", *Int. J. Solids Struct.* **43**:6 (2006), 1404–1421.

[Li et al. 2008] X. L. Li, X. R. Wang, L. Zhang, S. W. Lee, and H. J. Dai, "Chemically derived, ultrasmooth graphene nanoribbon semiconductors", *Science* **319**:5867 (2008), 1229–1232.

[Lim and Wang 2007] C. W. Lim and C. M. Wang, "Exact variational nonlocal stress modeling with asymptotic higher-order strain gradients for nanobeams", *J. Appl. Phys.* **101**:5 (2007), Article ID #054312.

[Love 1944] A. E. H. Love, *A treatise on the mathematical theory of elasticity*, 4th ed., Dover, New York, 1944.

[Lu 2007] P. Lu, "Dynamic analysis of axially prestressed micro/nanobeam structures based on nonlocal beam theory", *J. Appl. Phys.* **101**:7 (2007), Article ID #073504.

[Lu et al. 2006] P. Lu, H. P. Lee, C. Lu, and P. Q. Zhang, "Dynamic properties of flexural beams using a nonlocal elasticity model", *J. Appl. Phys.* **99**:7 (2006), Article ID #073510.

[Lu et al. 2007] P. Lu, H. P. Lee, C. Lu, and P. Q. Zhang, "Application of nonlocal beam models for carbon nanotubes", *Int. J. Solids Struct.* **44**:16 (2007), 5289–5300.

[Luo and Chung 2000] X. Luo and D. D. L. Chung, "Vibration damping using flexible graphite", *Carbon* **38**:10 (2000), 1510–1512.

[Martin 1996] C. R. Martin, "Membrane-based synthesis of nanomaterials", *Chem. Mater.* **8**:8 (1996), 1739–1746.

[Murmu and Pradhan 2009] T. Murmu and S. C. Pradhan, "Vibration analysis of nano-single-layered graphene sheets embedded in elastic medium based on nonlocal elasticity theory", *J. Appl. Phys.* **105**:6 (2009), Article ID #064319.

[Narendar and Gopalakrishnan 2009a] S. Narendar and S. Gopalakrishnan, "Nonlocal scale effects on wave propagation in multi-walled carbon nanotubes", *Comput. Mater. Sci.* **47**:2 (2009), 526–538.

[Narendar and Gopalakrishnan 2009b] S. Narendar and S. Gopalakrishnan, "Scale effects on wave propagation in carbon nanotubes", pp. 549–558 in *IISc Centenary International Conference and Exhibition on Aerospace Engineering* (*ICEAE*) (Bangalore, 2009), Indian Institute of Science, Bangalore, 2009.

[Narendar and Gopalakrishnan 2010a] S. Narendar and S. Gopalakrishnan, "Nonlocal scale effects on ultrasonic wave characteristics of nanorods", *Physica E* **42**:5 (2010), 1601–1604.

[Narendar and Gopalakrishnan 2010b] S. Narendar and S. Gopalakrishnan, "Terahertz wave characteristics of a single-walled carbon nanotube containing a fluid flow using the nonlocal Timoshenko beam model", *Physica E* **42**:5 (2010), 1706–1712.

[Narendar and Gopalakrishnan 2010c] S. Narendar and S. Gopalakrishnan, "Theoretical estimation of length dependent in-plane stiffness of single walled carbon nanotubes using the nonlocal elasticity theory", *J. Comput. Theor. Nanosci.* **7**:11 (2010), 2349–2354.

[Narendar and Gopalakrishnan 2010d] S. Narendar and S. Gopalakrishnan, "Ultrasonic wave characteristics of nanorods via nonlocal strain gradient models", *J. Appl. Phys.* **107**:8 (2010), Article ID #084312.

[Narendar et al. 2010] S. Narendar, D. R. Mahapatra, and S. Gopalakrishnan, "Investigation of the effect of nonlocal scale on ultrasonic wave dispersion characteristics of a monolayer graphene", *Comput. Mater. Sci.* **49**:4 (2010), 734–742.

[Novoselov et al. 2004] K. S. Novoselov, A. K. Geim, S. V. Morozov, D. Jiang, Y. Zhang, S. V. Dubonos, I. V. Grigorieva, and A. A. Firsov, "Electric field effect in atomically thin carbon films", *Science* **306**:5696 (2004), 666–669.

[Obraztsov et al. 2007] A. N. Obraztsov, E. A. Obraztsova, A. V. Tyurnina, and A. A. Zolotukhin, "Chemical vapor deposition of thin graphite films of nanometer thickness", *Carbon* **45**:10 (2007), 2017–2021.

[Ohta et al. 2006] T. Ohta, A. Bostwick, T. Seyller, K. Horn, and E. Rotenberg, "Controlling the electronic structure of bilayer graphene", *Science* **313**:5789 (2006), 951–954.

[Oshima and Nagashima 1997] C. Oshima and A. Nagashima, "Ultra-thin epitaxial films of graphite and hexagonal boron nitride on solid surfaces", *J. Phys. Condens. Matter* **9**:1 (1997), 1–20.

[Peddieson et al. 2003] J. Peddieson, G. R. Buchanan, and R. P. McNitt, "Application of nonlocal continuum models to nanotechnology", *Int. J. Eng. Sci.* **41**:3–5 (2003), 305–312.

[Reddy 2007] J. N. Reddy, "Nonlocal theories for bending, buckling and vibration of beams", *Int. J. Eng. Sci.* **45**:2–8 (2007), 288–307.

[Reddy and Pang 2008] J. N. Reddy and S. D. Pang, "Nonlocal continuum theories of beams for the analysis of carbon nanotubes", *J. Appl. Phys.* **103**:2 (2008), Article ID #023511.

[Sakhaee-Pour and Ahmadian 2008] A. Sakhaee-Pour and M. T. Ahmadian, "Potential application of single-layered graphene sheet as strain sensor", *Solid State Comm.* **147**:7–8 (2008), 336–340.

[Sakhaee-Pour et al. 2008a] A. Sakhaee-Pour, M. T. Ahmadian, and R. Naghdabadi, "Vibrational analysis of single-layered graphene sheets", *Nanotechnology* **19**:8 (2008), Article ID #085702.

[Sakhaee-Pour et al. 2008b] A. Sakhaee-Pour, M. T. Ahmadian, and A. Vafai, "Applications of single-layered graphene sheets as mass sensors and atomistic dust detectors", *Solid State Comm.* **145**:4 (2008), 168–172.

[Senturia 2001] S. D. Senturia, *Microsystem design*, Kluwer, Boston, 2001.

[Tomanek and Enbody 2000] D. Tomanek and R. Enbody, *Science and application of nanotubes*, Kluwer/Plenum, New York, 2000.

[Tounsi et al. 2008] A. Tounsi, H. Heireche, H. M. Berrabah, A. Benzair, and L. Boumia, "Effect of small size on wave propagation in double-walled carbon nanotubes under temperature field", *J. Appl. Phys.* **104**:10 (2008), Article ID #104301.

[Vossen and Kern 1978] J. L. Vossen and W. Kern, *Thin film processes*, Academic Press, New York, 1978.

[Wang 2005] Q. Wang, "Wave propagation in carbon nanotubes via nonlocal continuum mechanics", *J. Appl. Phys.* **98**:12 (2005), Article ID #124301.

[Wang and Duan 2008] C. M. Wang and W. H. Duan, "Free vibration of nanorings/arches based on nonlocal elasticity", *J. Appl. Phys.* **104**:1 (2008), Article ID #014303.

[Wang and Hu 2005] L. Wang and H. Hu, "Flexural wave propagation in single-walled carbon nanotubes", *Phys. Rev. B* **71**:19 (2005), Article ID #195412.

[Wang and Liew 2007] Q. Wang and K. M. Liew, "Application of nonlocal continuum mechanics to static analysis of micro- and nano-structures", *Phys. Lett. A* **363**:3 (2007), 236–242.

[Yakobson et al. 1997] B. I. Yakobson, M. P. Campbell, C. J. Brabec, and J. Bernholc, "High strain rate fracture and C-chain unraveling in carbon nanotubes", *Comput. Mater. Sci.* **8**:4 (1997), 341–348.

[Yang et al. 2002] F. Yang, A. C. M. Chong, D. C. C. Lam, and P. Tong, "Couple stress based strain gradient theory for elasticity", *Int. J. Solids Struct.* **39**:10 (2002), 2731–2743.

[Yang et al. 2008] J. Yang, X. L. Jia, and S. Kitipornchai, "Pull-in instability of nano-switches using nonlocal elasticity theory", *J. Phys. D Appl. Phys.* **41**:3 (2008), Article ID #035103.

[Zhou and Li 2001] S. J. Zhou and Z. Q. Li, *J. Shandong Univ. Technol.* **31** (2001), 401–407.

Received 13 Dec 2010. Revised 6 Apr 2012. Accepted 7 Apr 2012.

SAGGAM NARENDAR: snarendar@aero.iisc.ernet.in
Defence Research and Development Laboratory, Kanchanbagh, Hyderabad 500 058, India

SRINIVASAN GOPALAKRISHNAN: krishnan@aero.iisc.ernet.in
Department of Aerospace Engineering, Indian Institute of Science, Bangalore 560 012, India
http://www.aero.iisc.ernet.in/krishnan

JOURNAL OF MECHANICS OF MATERIALS AND STRUCTURES
Vol. 7, No. 5, 2012
dx.doi.org/10.2140/jomms.2012.7.435

NONLINEAR CREEP RESPONSE OF REINFORCED CONCRETE BEAMS

EHAB HAMED

The nonlinear viscoelastic behavior of reinforced concrete beams under sustained loading is investigated in this paper. A theoretical model is developed, which is based on the viscoelastic modified principle of superposition, and accounts for cracking, nonlinear behavior in compression, shrinkage, aging, and the creep rupture phenomenon of concrete. A nonlinear form of the relaxation modulus is presented, which is introduced into the constitutive relations and the corresponding nonlinear rheological Maxwell model, to account for damage. The governing equations are solved through time-stepping numerical integration, which yields an exponential algorithm following the expansion of the relaxation modulus into a Dirichlet series. The determination of the section-equivalent rigidities and creep strains along the cracked and uncracked regions is achieved through an iterative procedure at each time step. The capabilities of the model are demonstrated through numerical examples and parametric studies including comparison with test results available in the literature. The results show that creep has various and different influences on the structural response, and in some cases it may lead to a reduction of the load-carrying capacity of the member by creep rupture-type of failures.

1. Introduction

The creep behavior of reinforced concrete (RC) members in general and RC beams in particular has been intensively studied. Normally, the long-term effects of creep and shrinkage lead to a progressive increase in the deformations and a change of the cracking pattern over time, which are assumed to only affect the serviceability of RC members. Nevertheless, in some cases, structural members may be subjected to high levels of sustained loads, as is the case with dams, retaining walls, beam-columns, arches, containment vessels, cooling towers, and others. In such cases, the creep and shrinkage effects may put the structure out of service, may reduce the residual load-carrying capacity of the member over time (and hence reduce the factor of safety for failure), or may even lead to premature failures. This paper deals with the nonlinear viscoelastic behavior of RC members including the phenomenon of creep rupture, with special focus on RC beams.

The nonlinear viscoelastic response of RC beams exhibits a number of physical phenomena that require special attention. Among those is the time-dependent variation of the internal stresses with time, which results from the linear brittle behavior of concrete in tension and the nonlinear behavior in compression, and also from the restraint of the long-term effects by the steel reinforcement. This stress redistribution is combined with the shifting of the neutral axis with time. The prediction of these two effects becomes very

The work reported in this paper was supported by the Australian Research Council (ARC) through a Discovery Project (DP0987939).

Keywords: cracking, creep, long-term, nonlinear, reinforced concrete, viscoelasticity.

challenging under high levels of sustained loads due to the nonlinearity of stresses and their influence on the creep response, which cannot be described using the well-known linear viscoelastic models [Neville and Dilger 1970; Gilbert 1988]. Another phenomenon that results from the long-term effects is the propagation and widening of flexural cracks with time, as a result of the combined effects of creep, restrained shrinkage, and creep rupture in tension, in which the tensile capacity of concrete decreases over time. As a result of the latter effect, long-term cracking of points that are under sustained tensile stresses greater than about 70% of the tensile strength may occur [Zhou 1994]. Similar response occurs also in compression, where creep rupture of material points under sustained stress that is greater than about 80% of the compressive strength may occur [Carol and Murcia 1989; CEB-FIP 1990; Mazzotti and Savoia 2003], reducing the load-carrying capacity and the factor of safety of RC flexural members. Some experimental results regarding creep rupture in flexural plain concrete beams with notches were reported in [Omar et al. 2009], and it was revealed that tertiary creep and rupture occurred at load levels greater than 70% of the maximum load-carrying capacity. Understanding and clarifying these aspects, as well as the development of suitable and reliable theoretical models for their prediction, are essential for the safety assessment of existing structures and the design of new ones.

Bažant and Asghari [1977] combined the endochronic theory with a linear Maxwell chain model for investigating the nonlinear creep response of plain concrete under compression, but without considering the behavior of flexural members. In another study, Bažant and Chern [1985] developed a model suitable for finite element analysis of plain concrete using a strain softening element connected in series to a generalized Maxwell chain that describes the uncracked response. Yet, the response of RC flexural members and the incorporation of the material nonlinearity in compression were not considered. Papa et al. [1998] proposed an approach to model the progressive microcracking and creep acceleration of plain concrete under tension and compression, by gradually varying the Maxwell constants based on a damage variable. Mazzotti and Savoia [2003] combined the solidification theory of [Bažant and Prasannan 1989] with a damage model for the description of the nonlinear creep response of plain concrete under compression. Fernández Ruiz et al. [2007] proposed a simplified plasticity-damage model for plain concrete under compression. The nonlinear relation between creep strains and the stress level was introduced in their study through a stress-dependent creep coefficient (see also [CEB-FIP 1990]).

The studies mentioned above and many others [Carol and Murcia 1989; Santhikumar et al. 1998; Di Luzio 2009] focused on the creep response of plain concrete, while the nonlinear creep behavior of RC members has received less attention. The only studies that could be found in the literature regarding the nonlinear creep response of RC beams are those of [Bažant and Oh 1984; Li and Qian 1989]. The former was based on the effective elastic modulus approach and the linear principle of superposition, which are more appropriate for linear material response, and it did not include the effects of creep rupture and shrinkage-induced deformations. The latter included only a section analysis based on a creep damage model that depends on a number of parameters determined empirically. Limited results that include the time variation of the curvature were presented in [Li and Qian 1989], without the description of stresses, their relaxation and redistribution with time, propagation of cracking, creep rupture, and other effects.

In this paper, the nonlinear viscoelastic response of RC beams is investigated through a full nonlinear viscoelastic model that is based on the modified principle of superposition [Leaderman 1943]. This modeling approach also provides a potential alternative to most existing nonlinear creep models for plain concrete, which are based on combinations of linear viscoelastic rheological models with nonlinear

sliders, to model either cracking or material softening. The single-integral nonlinear viscoelastic model used here is converted into a differential-type relation after the expansion of the nonlinear relaxation modulus into a Dirichlet series. This yields a nonlinear generalized Maxwell model with the damage being modeled as strain-dependent spring and dashpot constants. The model uses beam theory with first-order shear deformations (Timoshenko beam), and it accounts for creep rupture under both tension and compression, shrinkage, aging, and yielding of the steel reinforcement, through an incremental time-stepping analysis. The mathematical model is applicable for any stress loading history, and any geometry, boundary conditions, and material properties. The assumptions made in the material and structural modeling are included in the mathematical formulation, which is followed by a numerical study and a comparison of the proposed model with experimental results.

2. Mathematical formulation

The mathematical formulation presented here focuses on RC beams, but it provides a basis for modeling further related structural members. The constitutive relations at the concrete material level and at the section level are presented first. They are followed by the formulation of the governing incremental equations and a description of the solution procedure. A smeared cracking modeling approach with full bonding between the concrete and the steel reinforcement is adopted, along with a distinction between the cracked and uncracked regions along the beam. It has been shown in many research studies [Rots and Blaauwendraad 1989] that the smeared cracking model, which assumes that stresses and strains are averaged over a representative length to span several cracks and microcracks, is an effective approach for predicting the cracking and post-cracking response of RC flexural members. This is mainly because it describes an integrated effect of the localized flexural cracks and microcracks, which are characterized by some levels of uncertainty regarding their real distribution. There is no doubt, however, that a discrete cracking model with a bond-slip law between the concrete and the steel will present a more comprehensive and accurate description of the localized structural behavior, but this effect is not described here. The sign conventions for the coordinates, deformations, loads, stresses, and stress resultants of a typical RC beam appear in Figure 1.

2.1. ***Constitutive relations at the material level.*** The constitutive relations are assumed to be independent of temperature and other environmental effects in order to clarify and highlight the time-dependent effects of creep and shrinkage. A superposition between the nonlinear viscoelastic strain $\varepsilon_{xx}^{\mathrm{v}}$ (equal to the instantaneous strain $\varepsilon_{xx}^{\mathrm{ins}}$ plus the creep strain $\varepsilon_{xx}^{\mathrm{cp}}$) and the stress-independent shrinkage strain $\varepsilon_{\mathrm{sh}}$ is assumed, that is, $\varepsilon_{xx} = \varepsilon_{xx}^{\mathrm{v}} + \varepsilon_{\mathrm{sh}}$, with ε_{xx} being the total strain. The instantaneous strain is related to the applied stress via a nonlinear short-term constitutive relation that accounts for cracking and material softening in compression, and it can refer to the elastic, inelastic, or cracking strains. The short-term constitutive relation provides the basis for developing the nonlinear relaxation function (as discussed in Section 3.1), which is used in the nonlinear viscoelastic model to describe the effects of cracking and damage produced by the creep strain as well. The formulation presented here is used to describe the creep and the short-term response; whereas the latter is obtained by choosing a number of fairly small time steps between $t = 10^{-9}$ to $t = 10^{-8}$ days, for example.

As mentioned earlier, the modified principle of superposition is adopted here for the nonlinear viscoelastic constitutive relations of concrete, which was first developed in [Leaderman 1943], and has been

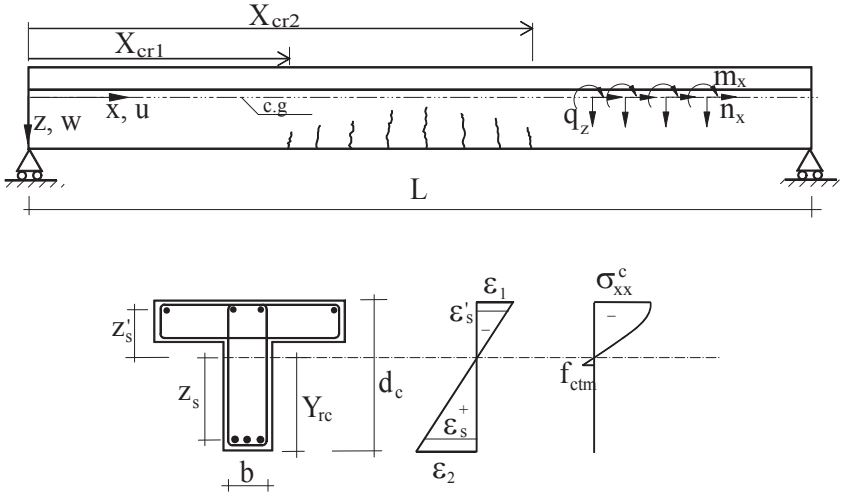

Figure 1. Geometry, loads, and sign conventions.

widely used for studying the nonlinear viscoelastic response of polymers and other materials [Pipkin and Rogers 1968; Findley et al. 1976], but with no reported application for reinforced concrete (to the best of the author's knowledge). Among other nonlinear viscoelastic models, it is chosen here as it skips over the difficulties associated with multiple integral representations (that is, evaluation of a large number of kernel functions) while still predicting the response of many materials with sufficient accuracy [Findley et al. 1976]. Following this principle, and assuming a differentiable strain history, the normal stress in concrete (σ_{xx}) takes the form

$$\sigma_{xx}(t) = \int_0^t \frac{\partial f(\varepsilon^{\mathrm{v}}_{xx}(t'), t-t')}{\partial \varepsilon^{\mathrm{v}}_{xx}(t')} \frac{d\varepsilon^{\mathrm{v}}_{xx}(t')}{dt'} dt', \tag{1}$$

where f is a nonlinear function of strain, which represents the time-dependent stress relaxation under constant strain. Equation (1) can be rewritten in the form

$$\sigma_{xx}(t) = \int_0^t R_{xx}(\varepsilon^{\mathrm{v}}_{xx}(t'), t-t') \frac{d\varepsilon^{\mathrm{v}}_{xx}(t')}{dt'} dt', \tag{2}$$

with R_{xx} as the nonlinear relaxation modulus of concrete under normal strains, which introduces the effects of time-dependent cracking and material softening into the model. Under short-term loading with no creep ($t = t'$), f corresponds to the instantaneous stress as a function of the strain level, while R_{xx} actually refers to the tangent elastic modulus. Due to the lack of data on the creep behavior of concrete in shear, the formulation focuses on the concrete response under normal stresses (tension and compression), from which the response in shear is estimated. To avoid storing the entire strain history, a differential-type constitutive relation is developed, following the same concepts presented in [Taylor et al. 1970; Bažant and Wu 1974], which are further extended to the nonlinear case. To do so, the relaxation modulus needs

to be expanded into a Dirichlet series including the effect of aging of the concrete, as follows:

$$R_{xx}(\varepsilon_{xx}^{\mathrm{v}}, t, t') \approx \bar{R}_{xx}(\varepsilon_{xx}^{\mathrm{v}}, t, t') = \sum_{\mu=1}^{N} E_{\mu}(\varepsilon_{xx}^{\mathrm{v}}, t') e^{-(t-t')/T_{\mu}} + E_{N+1}(\varepsilon_{xx}^{\mathrm{v}}, t'), \tag{3}$$

where $\bar{R}_{xx}$ is the approximated relaxation modulus, $E_{\mu}(\varepsilon_{xx}, t')$ is the modulus of the μ-th term in the series, N is the number of terms, and T_{μ} is the relaxation time of the μ-th term. Note that the moduli depend on the level of strain and the age of the concrete.

Following the Dirichlet series expansion, the total stress becomes the sum of the stresses of each term in the series as follows:

$$\sigma_{xx}(t) = \sum_{\mu=1}^{N} \sigma_{\mu}(t) + E_{N+1}(\varepsilon_{xx}^{\mathrm{v}}, t)\varepsilon_{xx}^{\mathrm{v}}(t). \tag{4}$$

Substitution of (3) into (2) for each term leads to

$$\sigma_{\mu}(t) = \int_{0}^{t} E_{\mu}(\varepsilon_{xx}^{\mathrm{v}}, t') e^{-(t-t')/T_{\mu}} \frac{d\varepsilon_{xx}^{\mathrm{v}}(t')}{dt'} dt'. \tag{5}$$

Differentiation of (5) with respect to t and rearranging the result leads to the differential equation

$$\frac{d\sigma_{\mu}}{dt} + \frac{\sigma_{\mu}}{T_{\mu}} = E_{\mu}(\varepsilon_{xx}^{\mathrm{v}}, t) \frac{d\varepsilon_{xx}^{\mathrm{v}}}{dt}. \tag{6}$$

Equation (6) actually describes the stress-strain relation in a Maxwell unit with age and strain-dependent spring modulus $E_{\mu}(\varepsilon_{xx}^{\mathrm{v}}, t)$ and a dashpot constant $\eta(\varepsilon_{xx}^{\mathrm{v}}, t) = E_{\mu}(\varepsilon_{xx}^{\mathrm{v}}, t)T_{\mu}$, while the entire nonlinear viscoelastic response is described by a nonlinear rheological generalized Maxwell model following (4). This formulation means that with the evolution of damage, the effects of cracking and material nonlinearity are introduced via the dependent of the spring and dashpot constants at each point through the depth of the RC section on the corresponding strain level, with unchanged relaxation times. Mathematically, it means that the concepts used for the development of the incremental algorithms in [Bažant and Wu 1974; Sorvari and Hämäläinen 2010] and other studies for linear cases can basically be applied here with special consideration of the strain and age dependency of the constants.

However, it was shown in many studies [Bažant and Prasannan 1989] that the calculation of the time-dependent (due to aging) spring constants is associated with numerical difficulties that may lead to results that violate basic thermodynamic laws (negative spring constants). For this, Bažant and Prasannan [1989] have developed a solidification theory for creep to overcome these difficulties. Nevertheless, it was shown in [Carol and Bažant 1993] that the solidification model is equivalent to the well-known rheologic Maxwell or Kelvin models but with spring constants that increase proportionally to the same function $v(t)$, which actually describes the increase in the macroscopic elastic modulus over time, and guarantees continuously increasing positive values for the spring constants. In the linear (strain-independent) case considered in [Carol and Bažant 1993], the age-dependent spring moduli are defined by $E_{\mu}(t) = v(t)E_{\mu}$. However, in the nonlinear case considered here, the aging function represents the time variation of the macroscopic tangent modulus; apart from its normal variation with time due to aging, it depends on the level of stress or its corresponding instantaneous strain. The spring moduli in this case are given by $E_{\mu}(\varepsilon_{xx}^{\mathrm{v}}, t) = v(\varepsilon_{xx}^{\mathrm{ins}}, t)E_{\mu}(\varepsilon_{xx}^{\mathrm{v}})$ for any given pair of instantaneous and viscoelastic strains which

varies with time due to creep and stress redistribution. The derivation of the aging function is given in Section 3.3. For completeness of the formulation and for clarity, the basic steps undertaken in the derivation of the incremental procedure, which follow [Bažant and Wu 1974; Sorvari and Hämäläinen 2010], are presented here.

Assuming that the time of concern is subdivided into n_t discrete times with $\Delta t = t_r - t_{r-1}$ $(r = 1, 2, n_t)$, the exact solution of (6) with initial condition $\sigma_\mu(t) = \sigma_\mu(t_{r-1})$ at $t = t_{r-1}$ is given by

$$\sigma_\mu(t_r) = e^{-\Delta t/T_\mu}\sigma_\mu(t_{r-1}) + \int_{t_{r-1}}^{t_r} e^{-(t_r-t')/T_\mu} v(\varepsilon_{xx}^{\text{ins}}(t'), t') E_\mu(\varepsilon_{xx}^{\text{v}}(t')) \frac{d\varepsilon_{xx}^{\text{v}}(t')}{dt'} dt'. \tag{7}$$

In order to evaluate the integral in (7), the strain rate, the aging function, and the spring modulus are assumed constant within the time interval provided that sufficiently small time steps that guarantee small changes of these parameters within the time interval are used. Equation (7) then becomes

$$\sigma_\mu(t_r) = e^{-\Delta t/T_\mu}\sigma_\mu(t_{r-1}) + E_\mu(\varepsilon_{xx}^{\text{v}}(t_r)) v(\varepsilon_{xx}^{\text{ins}}(t_r), t_r) \frac{\Delta\varepsilon_{xx}^{\text{v}}}{\Delta t} T_\mu[1 - e^{-\Delta t/T_\mu}]. \tag{8}$$

Using (4) and (8), the following incremental constitutive relation can be obtained for the response at $t = t_r$:

$$\Delta\varepsilon_{xx} = \frac{\Delta\sigma_{xx}}{E_c''(\varepsilon_{xx}^{\text{v}}(t_r))} + \Delta\varepsilon_c''(\varepsilon_{xx}^{\text{v}}(t_r)), \tag{9}$$

where E_c'' is the pseudonormal modulus, and $\Delta\varepsilon_c''$ is the incremental prescribed normal strain that includes both the effects of creep and shrinkage. These are given as follows:

$$E_c''(\varepsilon_{xx}^{\text{v}}(t_r)) = v(\varepsilon_{xx}^{\text{ins}}(t_r), t_r)\left[\sum_{\mu=1}^{N} [1 - e^{-\Delta t/T_\mu}] \frac{T_\mu}{\Delta t} E_\mu(\varepsilon_{xx}^{\text{v}}(t_r)) + E_{N+1}(\varepsilon_{xx}^{\text{v}}(t_r))\right], \tag{10}$$

$$\Delta\varepsilon_c''(\varepsilon_{xx}^{\text{v}}(t_r)) = \frac{1}{E_c''(\varepsilon_{xx}^{\text{v}}(t_r))} \sum_{\mu=1}^{N} [1 - e^{-\Delta t/T_\mu}]\sigma_\mu(t_{r-1}) + \Delta\varepsilon_{\text{sh}}. \tag{11}$$

For brevity, the incremental constitutive relation in shear is not given here, but it follows the same procedure outlined above with G_c'' as the pseudoshear modulus and γ_c'' as the prescribed creep engineering shear strain. The next section describes the constitutive relations at the section level of the RC beam, while the determination of the spring constants and other parameters appears in Section 3.

2.2. ***Constitutive relations at the section level.*** Following Timoshenko beam theory, the incremental kinematic relations are given as follows assuming small displacements:

$$\Delta\varepsilon_{xx}(x, z) = \frac{d}{dx}(\Delta u) - z\frac{d}{dx}(\Delta\phi), \tag{12}$$

$$\Delta\gamma_{xz}(x) = \frac{d}{dx}(\Delta w) - \Delta\phi, \tag{13}$$

where γ_{xz} is the engineering shear strain and w, u, and ϕ are the vertical displacement, the in-plane displacement at the reference line, and the rotation of the cross section, respectively.

The constitutive relations at the cross-section level are determined using the classical definition of the stress resultants and (9) as follows:

$$\Delta N_{xx} = \int_{Y_c - d_c}^{Y_c} bE_c''[\Delta\varepsilon_{xx} - \Delta\varepsilon_c'']\,\mathrm{d}z + E_s\Delta\varepsilon_s A_s + E_s'\Delta\varepsilon_s' A_s', \tag{14}$$

$$\Delta M_{xx} = \int_{Y_c - d_c}^{Y_c} bE_c''[\Delta\varepsilon_{xx} - \Delta\varepsilon_c'']\,z\,\mathrm{d}z + E_s\Delta\varepsilon_s A_s z_s + E_s'\Delta\varepsilon_s' A_s' z_s', \tag{15}$$

$$\Delta V_{xx} = \kappa \int_{Y_c - d_c}^{Y_c} bG_c''[\Delta\gamma_{xz} - \Delta\gamma_c'']\,\mathrm{d}z, \tag{16}$$

where b, Y_c, and d_c are the width, centroid, and depth of the RC beam, respectively (see Figure 1); E_s, ε_s, and A_s are the tangent modulus of elasticity, strain, and area of the tensioned reinforcement, respectively; E_s', ε_s', and A_s' are the tangent modulus of elasticity, strain, and area of the compressed reinforcement; z_s and z_s' are the distances of the steel reinforcement from the centroid of the uncracked beam (see Figure 1); and κ is the shear correction factor. E_c'', G_c'', $\Delta\varepsilon_c''$, and $\Delta\gamma_c''$ actually depend on the strain level at each material point based on (10) and (11); hence, they vary through the depth and length of the RC beam and introduce the effects of cracking and material nonlinearity at the section level. For brevity, the notation of the dependency of these parameters on the strain level is omitted. Also E_s and E_s' depend on the strain level and introduce the effect of yielding of the steel reinforcement into the model.

Substitution of the kinematic relations, (12) and (13), into (14)–(16) yields

$$\begin{bmatrix} \Delta N_{xx} \\ \Delta M_{xx} \\ \Delta V_{xx} \end{bmatrix} = \begin{bmatrix} A_{11} & B_{11} & 0 \\ B_{11} & D_{11} & 0 \\ 0 & 0 & \kappa A_{55} \end{bmatrix} \begin{bmatrix} \dfrac{d}{dx}(\Delta u) \\ -\dfrac{d}{dx}(\Delta\phi) \\ \dfrac{d}{dx}(\Delta w) - \Delta\phi \end{bmatrix} - \begin{bmatrix} \Delta\overline{N} \\ \Delta\overline{M} \\ \Delta\overline{V} \end{bmatrix}, \tag{17}$$

where A_{11}, B_{11}, D_{11}, and A_{55} are the extensional, extensional-bending, flexural, and shear viscoelastic rigidities of the RC beam, and $\overline{N}$, $\overline{V}$, and $\overline{M}$ are incremental effective forces and bending moment due to creep and shrinkage. The viscoelastic rigidities take the form

$$\begin{aligned} A_{11} &= \int_{Y_c - d_c}^{Y_c} bE_c''\,\mathrm{d}z + E_s A_s + E_s' A_s', & B_{11} &= \int_{Y_c - d_c}^{Y_c} bE_c''z\,\mathrm{d}z + E_s A_s z_s + E_s' A_s' z_s', \\ D_{11} &= \int_{Y_c - d_c}^{Y_c} bE_c''z^2\,\mathrm{d}z + E_s A_s z_s^2 + E_s' A_s' (z_s')^2, & A_{55} &= \int_{Y_c - d_c}^{Y_c} bG_c''\,\mathrm{d}z. \end{aligned} \tag{18}$$

The incremental effective forces due to creep and shrinkage are obtained by substitution of (11) into (14)–(16) and by assuming a constant shrinkage strain profile over the depth of the RC section as follows:

$$\Delta\overline{N} = \int_{Y_c - d_c}^{Y_c} b \sum_{\mu=1}^{N} [1 - e^{-\Delta t/T_\mu}]\sigma_\mu^c(t_{r-1})\,\mathrm{d}z + [A_{11} - E_s A_s - E_s' A_s']\Delta\varepsilon_{\mathrm{sh}}, \tag{19}$$

$$\Delta\overline{M} = \int_{Y_c - d_c}^{Y_c} b \sum_{\mu=1}^{N} [1 - e^{-\Delta t/T_\mu}]\sigma_\mu^c(t_{r-1})z\,\mathrm{d}z + [B_{11} - E_s A_s z_s - E_s' A_s' z_s']\Delta\varepsilon_{\mathrm{sh}}, \tag{20}$$

$$\Delta \overline{V} = \kappa \int_{Y_c - d_c}^{Y_c} b \sum_{\mu=1}^{N} [1 - e^{-\Delta t / T_\mu}] \tau_\mu^c(t_{r-1})\, dz. \tag{21}$$

2.3. ***Incremental governing equations.*** The incremental equilibrium equations of the RC beam, which can be found in any textbook of structural mechanics, take the form

$$\frac{d}{dx}(\Delta N_{xx}) = -\Delta n_x, \quad \frac{d}{dx}(\Delta V_{xx}) = -\Delta q_z, \quad \frac{d}{dx}(\Delta M_{xx}) - \Delta V_{xx} = \Delta m_x, \tag{22}$$

where N_{xx}, V_{xx}, and M_{xx} are the axial force, shear force, and bending moment, respectively, and q_z, n_x, and m_x are external distributed loads and bending moments, respectively. Substitution of the constitutive relations, (17), into the incremental equilibrium equations, (22), leads to the following first-order incremental governing differential equations in terms of the unknown deformations and internal forces:

$$\frac{d}{dx}(\Delta w) = (A_{55}\Delta\phi + \Delta \overline{V} + \Delta V_{xx})/A_{55}, \tag{23}$$

$$\frac{d}{dx}(\Delta \phi) = [B_{11}(\Delta N_{xx} + \Delta \overline{N}) - A_{11}(\Delta M_{xx} + \Delta \overline{M})]/(A_{11}D_{11} - B_{11}^2), \tag{24}$$

$$\frac{d}{dx}(\Delta M_{xx}) = \Delta m_x + \Delta V_{xx}, \quad \frac{d}{dx}(\Delta V_{xx}) = -\Delta q_z, \quad \frac{d}{dx}(\Delta N_{xx}) = -\Delta n_x, \tag{25}$$

$$\frac{d}{dx}(\Delta u) = [D_{11}(\Delta N_{xx} + \Delta \overline{N}) - B_{11}(\Delta M_{xx} + \Delta \overline{M})]/(A_{11}D_{11} - B_{11}^2). \tag{26}$$

2.4. ***Solution procedure.*** At each time step, (23)–(26) present a spatial set of nonlinear differential equations due to the dependency of the rigidities on the unknown deformations via (18). In general, these rigidities may vary along the uncracked and cracked regions due to the material nonlinearity. Here, a piecewise uniform distribution of the rigidities is assumed along the cracked (smeared cracking) and uncracked regions. Thus, the rigidities along the cracked region are determined based on analysis of the critical cross section, while the rigidities at the uncracked region are assumed strain-independent. This defines two types of parameters that need to be determined at each time step, namely: the rigidities at the critical section, and the start and end locations of the cracked region (X_{cr1} and X_{cr2}; see Figure 1). An iterative procedure is used for the determination of these parameters at each time step, while due to the piecewise variation of the rigidities and the continuous variation along the beam of the incremental effective forces due to creep and shrinkage, a numerical technique that is based on the multiple shooting method [Stoer and Bulirsch 2002] is adopted for the solution of the equations at each iteration. The iterative procedure basically follows [Rabinovitch and Frostig 2001; Hamed and Rabinovitch 2008] but it is slightly modified here to account for the viscoelastic response, as follows:

Step 1. Initial guess. At the first iteration of the first increment of instantaneous loading, the beam is assumed uncracked. However, for the progressive time steps (load increment), the solution from the previous time step is used as the initial guess for the current step.

Step 2. Analysis of the structure. Using the rigidities calculated in the initial guess or in the previous iteration (Step 3.3), as well as the calculated locations of the start and end points of the cracked region, the incremental governing equations become linear ones with variable coefficients in space, which are solved numerically.

Step 3. Analysis of the critical section (at the location of maximum moment). Based on the solution obtained in Step 2, the equivalent rigidities of the critical section are determined as follows:

3.1 A linear distribution of the incremental total strain is assumed:

$$\Delta\varepsilon_{xx} = \frac{\Delta\varepsilon_1 + \Delta\varepsilon_2}{2} - \frac{\Delta\varepsilon_1 - \Delta\varepsilon_2}{d_c} z, \tag{27}$$

where $\Delta\varepsilon_1$ and $\Delta\varepsilon_2$ are the incremental strains at the upper and lower faces of the RC beam, as shown in Figure 1.

3.2 Based on the incremental internal forces obtained in Step 2, two nonlinear algebraic equations are stated in terms of the two unknowns $\Delta\varepsilon_1$ and $\Delta\varepsilon_2$, which are based on equilibrium of forces and moments at the current time step, as follows:

$$\Delta N_{xx} = \int_{Y_c - d_c}^{Y_c} b\Delta\sigma_{xx}\,\mathrm{d}z + E_s\Delta\varepsilon_s A_s + E'_s\Delta\varepsilon'_s A'_s, \tag{28}$$

$$\Delta M_{xx} = \int_{Y_c - d_c}^{Y_c} b\Delta\sigma_{xx} z\,\mathrm{d}z + E_s\Delta\varepsilon_s A_s z_s + E'_s\Delta\varepsilon'_s A'_s z'_s, \tag{29}$$

where $\Delta\sigma_{xx}$ is defined via (9). As creep in RC beams tends to shift the neutral axis downwards [Gilbert 1988], the tensile capacity of already-cracked material points under instantaneous loading is set to zero in solving (28) and (29) with time.

3.3 Once the normal strain distribution is determined in Step 3.2, as well as the corresponding normal and shear stresses, the spring moduli of each point through the depth of the RC beam are determined. Consequently, the viscoelastic rigidities and the incremental effective forces due to creep and shrinkage are determined through (18) and (19)–(21), respectively.

Step 4. Convergence criterion. If the norm of the relative difference between the magnitudes of the viscoelastic rigidities, as well as X_{cr1} and X_{cr2}, in two successive iterations is sufficiently small, the iterative procedure stops. Otherwise, the procedure returns to Step 2 with the updated rigidities of Step 3.3.

3. Material properties and model parameters

The incremental mathematical model developed in Section 2 is valid for any desired creep model and material properties provided that the strain-dependent relaxation modulus and the corresponding spring moduli of the Maxwell model are known. Here, the specific viscoelastic models that are adopted in the numerical study, and which can be used for the analysis of most RC structures, are discussed, along with the determination of the model parameters (that is, relaxation modulus and spring and dashpot constants).

3.1. ***Nonlinear relaxation modulus of concrete.*** Before the characterization of the nonlinear relaxation modulus, the instantaneous stress-strain law, from which the viscoelastic constitutive relations are derived, is presented. The material properties and material models are taken from [CEB-FIP 1990; 1999] with

the following instantaneous stress-strain relation that is also shown in Figure 2:

$$\sigma_{xx} = \begin{cases} \dfrac{E_0\varepsilon_{xx}^{\text{ins}} + f_{\text{cm}}\dfrac{(\varepsilon_{xx}^{\text{ins}})^2}{\varepsilon_c^2}}{1-\left(\dfrac{E_0\varepsilon_c}{f_{\text{cm}}}+2\right)\dfrac{\varepsilon_{xx}^{\text{ins}}}{\varepsilon_c}} & \text{for } \varepsilon_{\text{lim}}^c \le \varepsilon_{xx}^{\text{ins}} \le \varepsilon_{\text{cr}}, \\ f_{\text{ctm}} + E_d(\varepsilon_{xx}^{\text{ins}} - \varepsilon_{\text{cr}}) & \text{for } \varepsilon_{\text{cr}} < \varepsilon_{xx}^{\text{ins}} \le \varepsilon_{\text{lim}}^t, \\ 0 & \text{for } \varepsilon_{\text{lim}}^t < \varepsilon_{xx}^{\text{ins}}, \end{cases} \tag{30}$$

where f_{cm} is the mean compressive strength that equals $f_{\text{ck}} + 8$ (in MPa) with f_{ck} being the characteristic strength, E_0 is the modulus of elasticity, ε_c is the strain at peak compressive stress, ε_{cr} is the cracking strain (determined based on the mean tensile strength as f_{ctm}/E_0), and $\varepsilon_{\text{lim}}^c$ is the strain that corresponds to a stress of $0.5 f_{\text{cm}}$ at the descending part of the diagram; further, $E_d = -0.483E_0/(0.393 + f_{\text{ctm}})$ describes the tension-softening effect [Bažant and Oh 1984], and $\varepsilon_{\text{lim}}^t = \varepsilon_{\text{cr}} - f_{\text{ctm}}/E_d$.

The stress-strain curve of the steel is based on a linear elastic-perfectly plastic behavior with ε_y as the yielding strain as follows:

$$\sigma_s = \begin{cases} E_s\varepsilon_s & \text{for } -\varepsilon_y \le \varepsilon_s \le \varepsilon_y, \\ E_s\varepsilon_y & \text{otherwise.} \end{cases} \tag{31}$$

The failure criteria in tension and compression are based on limit strains in order to account for the creep rupture effects. Under instantaneous loading, cracking occurs once $\varepsilon_{xx}^{\text{ins}}$ becomes greater than ε_{cr}. For simplicity, the strain-softening effect is ignored and the stresses are assumed to drop immediately to zero upon cracking. Many studies show that the effects of tension-softening and tension-stiffening are mostly dominant in lightly reinforced structures, which is not the case in most RC beams [Gilbert 2007]. Under sustained loading, on the other hand, it is assumed that creep rupture in tension occurs when the viscoelastic strain (creep curve) intersects the descending part of the stress-strain curve [Zhou 1994], allowing $\varepsilon_{xx}^{\text{v}}$ to exceed ε_{cr} without immediate failure as observed in some experimental studies and shown in Figure 2. In other words, it is assumed that the instantaneous stress-strain curve serves

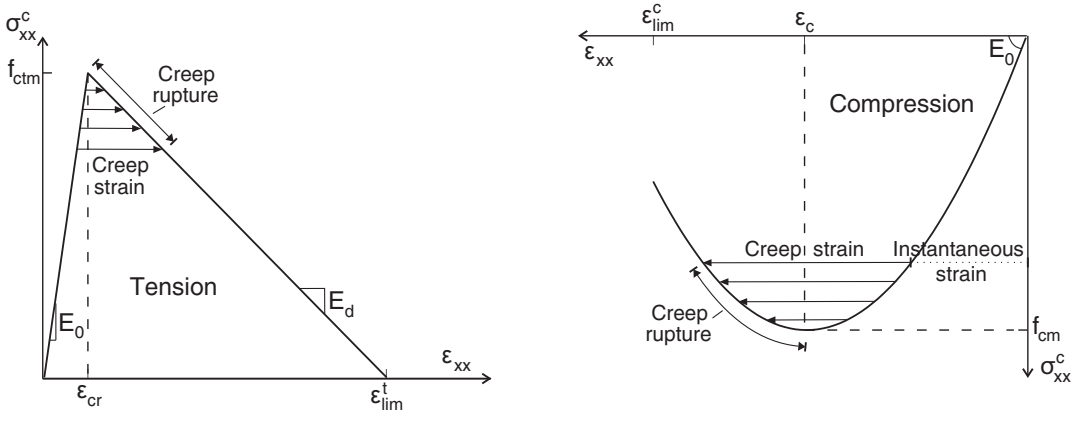

Figure 2. Stress-strain curves of concrete under tension and compression.

as an envelope failure criterion. Following this procedure, the failure strain envelope in tension ε_f^t is given by

$$\varepsilon_f^t = \frac{\sigma_{xx}^c - f_{\text{ctm}}}{E_d} + \varepsilon_{\text{cr}}. \tag{32}$$

Thus, the relaxation modulus of any point through the depth of the RC beam, for which its viscoelastic strain exceeds its corresponding failure strain, is set to zero to simulate the creep rupture effect. Note that due to aging, the failure envelope changes with time.

As the paper focuses on the nonlinear creep response rather than the behavior under short-term loading, which is well known, failure in compression under instantaneous loading is not accounted for. Thus, it is assumed that the level of instantaneous compressive strains is smaller than ε_c (in absolute value). Nevertheless, in order to account for the creep rupture failure in compression, a limit strain failure criterion should be used. In general, the creep rupture failure envelope in compression is a descending curve from the peak static strength to a horizontal line at about (0.7–0.8) f_{cm} [Carol and Murcia 1989; Omar et al. 2009]. Here, it is assumed that this descending curve is similar to the descending (strain softening) part of the stress-strain curve given in (30), indicating that also under compression, creep rupture occurs once the viscoelastic strain intersects the stress-strain diagram as shown in Figure 2 [Fernández Ruiz et al. 2007]. Such similarity between the modeling of damage due to creep and material nonlinearity under short term loading is owned to the similarities in their sources, which correspond to interfacial bond microcracks between the aggregates and the mortar, and microcracking of the mortar material itself [Bažant and Asghari 1977; Li and Qian 1989]. Using the strain-softening part of (30) in compression, the failure strain envelope in compression ε_f^c takes the form

$$\varepsilon_f^c = \frac{-E_0 - \dfrac{E_0\sigma_{xx}}{f_{\text{cm}}} - \dfrac{2\sigma_{xx}}{\varepsilon_c} - \left[\left(E_0 + \dfrac{E_0\sigma_{xx}}{f_{\text{cm}}} + \dfrac{2\sigma_{xx}}{\varepsilon_c}\right)^2 + 4\dfrac{f_{\text{cm}}\sigma_{xx}}{\varepsilon_c^2}\right]^{1/2}}{2f_{\text{cm}}/\varepsilon_c^2}. \tag{33}$$

Based on these assumptions, the nonlinear relaxation functions should be defined for the uncracked material points with $\varepsilon_c \le \varepsilon_{xx}^{\text{ins}} \le \varepsilon_{\text{cr}}$ while $\varepsilon_{xx}^{\text{v}}$ can be greater than ε_{cr} or ε_c (in absolute value) as shown in Figure 2.

The determination of the relaxation modulus is based on the compliance modulus because of the limited experimental data available for its calibration. Nevertheless, the well-known convolution integral relation between the relaxation and compliance moduli is not valid for nonlinear materials [Findley et al. 1976]. This introduces some difficulties in the determination of the nonlinear relaxation modulus, also because, as shown in [Oza et al. 2003], a separable nonlinear compliance (between time and stress) normally leads to a nonseparable form of a relaxation modulus. Oza et al. [2003] provided closed-form expressions of the nonlinear relaxation modulus for some specific compliance moduli of ligaments and metals based on a single integral nonlinear superposition method. Other numerical approaches for obtaining the nonlinear relaxation modulus from the compliance modulus at each time step were developed in [Brueller and Steiner 1993; Touati and Cederbaum 1997]. Here, the relaxation modulus is estimated based on a trial and error method seeking a closed-form expression. This is based on the physical meaning of the kernels in (1) and the corresponding creep equation given below (see [Findley

et al. 1976]):

$$\varepsilon_{xx}^{\mathrm{v}}(t) = \int_0^t \frac{\partial g(\sigma_{xx}(t'), t-t')}{\partial \sigma_{xx}(t')} \frac{d\sigma_{xx}(t')}{dt'} dt', \tag{34}$$

where g is a nonlinear function of stress, which represents the time-dependent viscoelastic strain under constant stress, and $\partial g/\partial \sigma_{xx}$ is the nonlinear compliance modulus. The problem actually reduces to finding a general stress history $\sigma_{xx}(t) = \sigma_h(t)$, such that when inserted into (34), then the obtained viscoelastic strain $\varepsilon_{xx}^{\mathrm{v}}(t)$ becomes constant with time and equals to a desired value (ε_{xx}^0). In other words, since creep and relaxation are two aspects of the same viscoelastic material behavior, then the time-dependent stress (function f in (1)) that will be obtained in a relaxation test under a certain value of strain is exactly the same one that needs to be used in a stress-varying creep test ($\sigma_{xx}(t) = \sigma_h(t)$ in (34)) to obtain the same constant strain value.

Using the ascending part (in absolute value) of the short-term stress-strain relation of the concrete, (30), the function g in (34) takes the following separable form for $f_{\mathrm{cm}} \le \sigma_{xx} \le f_{\mathrm{ctm}}$:

$$g = \frac{-E_0 - \dfrac{E_0\sigma_{xx}}{f_{\mathrm{cm}}} - \dfrac{2\sigma_{xx}}{\varepsilon_c} + \left[\left(E_0 + \dfrac{E_0\sigma_{xx}}{f_{\mathrm{cm}}} + \dfrac{2\sigma_{xx}}{\varepsilon_c}\right)^2 + 4\dfrac{f_{\mathrm{cm}}\sigma_{xx}}{\varepsilon_c^2}\right]^{1/2}}{2f_{\mathrm{cm}}/\varepsilon_c^2}(1+\varphi(t)), \tag{35}$$

where $\varphi(t)$ is the creep coefficient that is evaluated based on [CEB-FIP 1990]. Note that in this simplified formulation, the nonlinearity between stresses and creep strains is modeled through the constitutive law only [Bockhold and Petryna 2008] and not through a stress-dependent creep coefficient [CEB-FIP 1990; Fernández Ruiz et al. 2007].

Following the procedure outlined above, different potential stress histories ($\sigma_{xx}(t) = \sigma_h(t)$) need to be introduced into (34). The one that leads to constant strain values with time at different levels of initial strain is the one that corresponds to the function f in (1), which will be used for the derivation of the relaxation modulus. The basis for choosing such stress histories is that they should actually be decreasing functions with time and have to fulfill the instantaneous stress-strain relation at $t = 0$. The following general form is proposed with ε_{xx}^0 being the desired constant strain value:

$$\sigma_h(t) = \frac{\dfrac{1}{(1+\varphi(t))^{\alpha}}\left(E_0\varepsilon_{xx}^0 + \dfrac{f_{\mathrm{cm}}}{(1+\varphi(t))^{\zeta}}\dfrac{(\varepsilon_{xx}^0)^2}{\varepsilon_c^2}\right)}{1 - \left(\dfrac{E_0\varepsilon_c}{f_{\mathrm{cm}}} + 2\right)\dfrac{\varepsilon_{xx}^0}{\varepsilon_c}}. \tag{36}$$

Figure 3 shows the normalized time variation of the strain at different levels obtained from different stress histories with different values of α and ζ (see (36)). For this illustration, f_{cm} is taken as 38 MPa, $\varepsilon_c = -0.224\%$, and $E_0 = 33.5$ GPa. The creep coefficient is assumed to follow [CEB-FIP 1990] as $\varphi(t) = \varphi_u t^{0.3}/(t+\beta_H)^{0.3}$ with $\varphi_u = 2.11$ and $\beta_H = 459$. The integration of (34) is achieved using an incremental time-stepping numerical integration, assuming a constant compliance function (averaged over two consecutive times) during each time interval following a nonlinear superposition approach [Oza et al. 2003; Hamed et al. 2011]. It can be seen that at the low level of initial strain ($0.05\varepsilon_c$), all stress histories reveal a very small change of the normalized strain with time (a deviation of less than 2%). However, under higher levels of initial strains where material nonlinearity becomes significant ($0.25\varepsilon_c$ and $0.45\varepsilon_c$, that correspond to stresses of $0.43 f_{\mathrm{cm}}$ and $0.7 f_{\mathrm{cm}}$, respectively), only the stress history with

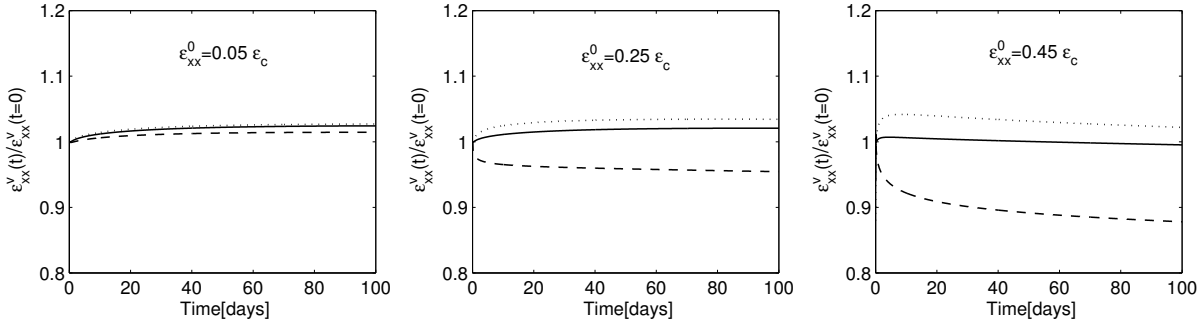

Figure 3. Variation of strain in time under different decreasing stress histories at different levels of initial strain (the solid line indicates $\alpha = 1$, $\zeta = 1$; the dashed $\alpha = 1$, $\zeta = 0$; and the dotted $\alpha = 1$, $\zeta = 2$).

$\alpha = \zeta = 1$ still yields a very small change, while stress histories achieved with other values of α and ζ reveal significantly varying strains with time. Hence, the function f is assumed to take the form of (36) with $\alpha = \zeta = 1$ and replacing ε^0_{xx} with $\varepsilon^{\mathrm{v}}_{xx}$. It has to be mentioned that the exercise outlined in Figure 3 has been implemented at various material properties to verify the validity of the chosen function f. No doubt a more accurate method to evaluate the function f would be one based on minimization of the error at each time step [Brueller and Steiner 1993; Touati and Cederbaum 1997], but the method outlined above is chosen as it provides a closed-form solution with an acceptable accuracy.

Once the function f is defined, the nonlinear strain-dependent relaxation modulus can be obtained by differentiating f with respect to $\varepsilon^{\mathrm{v}}_{xx}$ (see (1) and (2)) to yield a closed nonseparable form of the nonlinear relaxation modulus of concrete as follows:

$$R_{xx} = \frac{E_0}{\bar{a}(1+\varphi(t))} + \frac{E_0\varepsilon^{\mathrm{v}}_{xx}}{\bar{a}(1+\varphi(t))}\left[\frac{2f_{\mathrm{cm}}}{E_0\varepsilon_c^2} + \frac{E_0}{\bar{a}\,f_{\mathrm{cm}}} + \frac{2}{\bar{a}\varepsilon_c}\right] + \frac{E_0(\varepsilon^{\mathrm{v}}_{xx})^2}{[\bar{a}(1+\varphi(t))]^2}\left[\frac{1}{\varepsilon_c} + \frac{2f_{\mathrm{cm}}}{E_0\varepsilon_c^3}\right], \tag{37}$$

where $\bar{a} = 1 - E_0\varepsilon^{\mathrm{v}}_{xx}/f_{\mathrm{cm}} - 2\varepsilon^{\mathrm{v}}_{xx}/\varepsilon_c$. For relatively small strains (that is, $0.15\varepsilon_c \le \varepsilon^{\mathrm{v}}_{xx} \le \varepsilon_{\mathrm{cr}}$), the second and third terms are relatively small and $\bar{a} \approx 1$; thus, (37) yields the classical approximated form of the relaxation modulus of a linear viscoelastic material as $\approx 1/J_{xx}$ (with J_{xx} as the compliance function). Also note that for $\varphi(t) = 0$, (37) yields the strain-dependent tangent modulus of concrete.

The effect of aging on the nonlinear relaxation modulus is introduced through the development of f_{cm}, E_0, and ε_c with time as follows [CEB-FIP 1990; 1999]:

$$f_{\mathrm{cm}}(t) = (f_{\mathrm{ck}} + 8)\exp\left\{0.25\left[1 - \left(\frac{28}{t}\right)^{1/2}\right]\right\}, \tag{38}$$

$$E_0(t) = \sqrt{\frac{f_{\mathrm{cm}}(t)}{f_{\mathrm{cm}}(28)}}\,E_0(28), \tag{39}$$

$$\varepsilon_c(t) = -0.0017 - 0.001(f_{\mathrm{cm}}(t))/70, \tag{40}$$

where t refers to the age of concrete in days, and f_{ck} and f_{cm} are in MPa. The development of the tensile

strength f_{ctm} with time is assumed to follow that of the compressive strength, which is given by

$$f_{\text{ctm}} = \frac{f_{\text{cm}}(t)}{f_{\text{cm}}(28)} 1.4 \left(\frac{f_{\text{ck}}}{10} \right)^{2/3}. \tag{41}$$

3.2. ***Springs and dashpot constants in Maxwell model.*** Given the strain and age-dependent relaxation modulus appears in (37) and the relation $E_\mu(\varepsilon^{\text{v}}_{xx}, t) = v(\varepsilon^{\text{ins}}_{xx}, t) E_\mu(\varepsilon^{\text{v}}_{xx})$ described earlier, the strain-dependent spring and dashpot constants of the Maxwell model can be obtained by a least squares or other curve-fitting method following (3). Thus, for any given strain level, the relaxation function given in (37) is expanded into a Dirichlet series, (3), and the Maxwell constants are determined. For this, the relaxation times and the number of units are chosen in advance considering the time of interest [Bažant and Wu 1974], and the moduli of the springs become the only unknowns in the generalized Maxwell chain. A least squares method that was proposed in [Bažant and Wu 1974] is used here for the determination of the spring moduli, which is based on minimization the following expression ($d\Phi/dE_u$):

$$\begin{aligned} \Phi = \sum_{i}^{N_t} [\bar{R}_{xx}(\varepsilon^{\text{v}}_{xx}, t_i) - R_{xx}(\varepsilon^{\text{v}}_{xx}, t_i)]^2 + \omega_1 \sum_{\mu=1}^{N-1} [E_{\mu+1}(\varepsilon^{\text{v}}_{xx}) - E_\mu(\varepsilon^{\text{v}}_{xx})]^2 \\ + \omega_2 \sum_{\mu=1}^{N-2} [E_{\mu+2}(\varepsilon^{\text{v}}_{xx}) - 2E_{\mu+1}(\varepsilon^{\text{v}}_{xx}) + E_\mu(\varepsilon^{\text{v}}_{xx})]^2 \\ + \omega_3 \sum_{\mu=1}^{N-3} [E_{\mu+3}(\varepsilon^{\text{v}}_{xx}) - 3E_{\mu+2}(\varepsilon^{\text{v}}_{xx}) + 3E_{\mu+1}(\varepsilon^{\text{v}}_{xx}) - E_\mu(\varepsilon^{\text{v}}_{xx})]^2, \end{aligned} \tag{42}$$

where N_t is the number of selected times for which minimization of the error is conducted, and ω_1, ω_2, and ω_3 are weight functions that are determined to achieve best fitting.

Nevertheless, in order to avoid calculation of the spring moduli via minimization of (42) at each strain level, the calculation is made here at a number of selected strain levels (N_ε) along with the use of an interpolation function for each spring modulus to obtain a continuous variation. The following interpolation function is used for the μ-th spring modulus:

$$E_\mu(\varepsilon^{\text{v}}_{xx}) \approx \bar{E}_\mu(\varepsilon^{\text{v}}_{xx}) = c_{1\mu} + c_{2\mu}\varepsilon^{\text{v}}_{xx} + c_{3\mu}(\varepsilon^{\text{v}}_{xx})^2 + c_{4\mu}(\varepsilon^{\text{v}}_{xx})^3 + c_{5\mu}(\varepsilon^{\text{v}}_{xx})^4. \tag{43}$$

Note that after the minimization of (42) at N_ε strain levels, a series of N_ε values is obtained for every spring modulus, from which the interpolation function that appears in (43) is determined. Also here, the constants $c_{1\mu}$ to $c_{5\mu}$ are determined by traditional least squares or other curve-fitting methods.

However, due to the creep rupture phenomenon of concrete, the spring moduli actually follow (43) up to certain levels of strains. The final expression for the spring moduli under normal stresses takes the form

$$E^c_\mu(\varepsilon^{\text{v}}_{xx}) = \begin{cases} \bar{E}_\mu(\varepsilon^{\text{v}}_{xx}) & \text{for } \varepsilon^c_f \le \varepsilon^{\text{v}}_{xx} \le \varepsilon^t_f, \\ 0 & \text{otherwise.} \end{cases} \tag{44}$$

Thus, the spring moduli of any point through the depth of the RC beam, for which its viscoelastic strain exceeds its corresponding failure strain, is set to zero to simulate the creep rupture failure.

The spring moduli in shear are estimated from (44) assuming that Poisson's ratio ν and the shear retention factor β, which simulates the shear resistance at the cracked interfaces owing to the aggregate interlock and dowel action [Rots and de Borst 1987], are constant with time and independent upon the stress level. Thus, using the same relaxation times and number of units as in the normal direction, the spring moduli in shear take the form

$$G_\mu^c(\varepsilon_{xx}^{\mathrm{v}}) = \begin{cases} \dfrac{\bar{E}_\mu(\varepsilon_{xx}^{\mathrm{v}})}{2(1+\nu)} & \text{for } \varepsilon_f^c \le \varepsilon_{xx}^{\mathrm{v}} \le \varepsilon_f^t, \\ \dfrac{\beta \bar{E}_\mu(\varepsilon_f^t)}{2(1+\nu)} & \text{for } \varepsilon_f^t < \varepsilon_{xx}^{\mathrm{v}}, \\ 0 & \text{otherwise.} \end{cases} \tag{45}$$

3.3. ***Aging function.*** As mentioned earlier, the effect of aging is introduced through the function $v(\varepsilon_{xx}^{\mathrm{ins}}, t)$, which is evaluated based on the time-variation of the tangent elastic modulus with respect to its magnitude at the time of initial loading. Setting $\varphi(t) = 0$ in (37) along with replacing the viscoelastic strain ($\varepsilon_{xx}^{\mathrm{v}}$) by the instantaneous one ($\varepsilon_{xx}^{\mathrm{ins}}$) as a result, and the use of (38)–(40), lead to a closed-form expression for the time-dependent tangent elastic modulus $E_t(\varepsilon_{xx}^{\mathrm{ins}}, t) = R_{xx}$, which for brevity is not presented here. Then $v(\varepsilon_{xx}^{\mathrm{ins}}, t)$ can be evaluated as $E_t(\varepsilon_{xx}^{\mathrm{ins}}, t)/E_t(\varepsilon_{xx}^{\mathrm{ins}}, t_0)$, where t_0 corresponds to the age of the concrete at the time of initial loading.

4. Numerical study

The numerical study includes two numerical examples and parametric studies that highlight and clarify the nonlinear creep response of RC beams, and exhibit the capabilities of the proposed model. A comparison of the model with test results available in the literature is also included.

4.1. ***First example: Beam under bending only.*** A simply supported RC beam, 4.0 m long and with a rectangular cross-section 200 mm wide and 400 mm high is used for the investigation. The beam includes two bars of 24 mm diameter (a reinforcement ratio of $\rho_s = 1.2\%$) located at 30 mm from the bottom ($z_s = 170$ mm) with $E_s = 200$ GPa, and is subjected to a uniformly distributed sustained load of 60 kN/m. The modulus of elasticity and mean compressive strength of the concrete are taken as $E_0 = 33.5$ GPa and $f_{\mathrm{cm}} = 38$ MPa, while the tensile strength and peak compressive strain are $f_{\mathrm{ctm}} = 2.91$ MPa and $\varepsilon_c = -0.22\%$ following (40) and (41). The development in time of the creep coefficient and shrinkage strain follows [CEB-FIP 1990] with ultimate values of $\varphi_u = 2.11$ and $\varepsilon_{\mathrm{sh}}(t = \infty) = -0.042\%$. The Poisson's ratio, the shear retention factor, and the shear correction factor are taken as 0.17, 0.2, and 0.833, respectively. In order to highlight the effect of creep only, the effects of shrinkage and compressive reinforcement are not considered at this stage, but are separately investigated in the subsequent. The analysis is conducted up to 3 years from first loading where the creep coefficient reaches a magnitude of 1.9. Seven Maxwell units are used in the material model along with the use of (43) to account for the nonlinear variation of the Maxwell constants with the strain level. The relaxation times are chosen as $T_\mu = 0.1 \times 5^{\mu-1}$ days, for $\mu = 1, \ldots, 6$, and the spring moduli take the following strain-dependent form

(in GPa) following (43):

$$\begin{bmatrix} \bar{E}_1 \\ \bar{E}_2 \\ \bar{E}_3 \\ \bar{E}_4 \\ \bar{E}_5 \\ \bar{E}_6 \\ \bar{E}_7 \end{bmatrix} = \begin{bmatrix} 5.337 & 9.962 & -0.295 & -0.757 & -0.505 \\ 1.881 & -2.916 & -0.863 & -0.289 & 0.75 \\ 3.346 & 0.026 & -0.149 & -0.32 & -0.104 \\ 4.03 & -4.88 & -0.145 & -0.388 & 0.283 \\ 3.843 & -3.736 & -0.11 & -0.446 & 0.103 \\ 3.607 & -2.491 & -0.745 & -0.282 & -0.142 \\ 11.483 & -3.509 & -0.104 & -0.308 & 0.232 \end{bmatrix} \begin{bmatrix} 1 \\ \varepsilon_{xx}^{\mathrm{v}} \\ (\varepsilon_{xx}^{\mathrm{v}})^2 \\ (\varepsilon_{xx}^{\mathrm{v}})^3 \\ (\varepsilon_{xx}^{\mathrm{v}})^4 \end{bmatrix}. \tag{46}$$

Figure 4 shows the distribution of the instantaneous and long-term normal strains and stresses at midspan through the depth of the beam. The results show the nonlinear stress distribution at $t = 0$, with a maximum compressive stress of -26.8 MPa ($\approx 0.7 f_{\mathrm{cm}}$). Due to creep, an increase in the tension force of the elastic reinforcement occurs as it tends to restrain the creep deformations. As a result, a compressive force in the concrete of equal magnitude has to develop to maintain equilibrium. Yet, because the bending moment is unchanged, the lever arm between the steel and concrete must decrease by a shifting down of the neutral axis from $z_0 = -68.9$ mm to $z_0 = -17.6$ mm as shown in Figure 4. Due to this significant shifting, the loaded area of the concrete is increased resulting in a release and redistribution of the stresses with time. Note that as this shifting occurs, the neutral axis passes through points, which were already cracked under instantaneous loading, and for which their tensile capacity is set to zero, as can be seen in the distribution of stresses 3 years after loading. These stress and strain redistributions with time, which also occur in the linear case [Gilbert 1988], are well captured and explained by the proposed model in the nonlinear range of stresses.

The time variation of the central deflection, peak curvature (defined as $\chi = d\phi/dx$), peak force in the reinforcement, and peak compressive stress in the concrete appear in Figure 5 with and without the inclusion of the aging effect in the analysis. The results are normalized with respect to the instantaneous

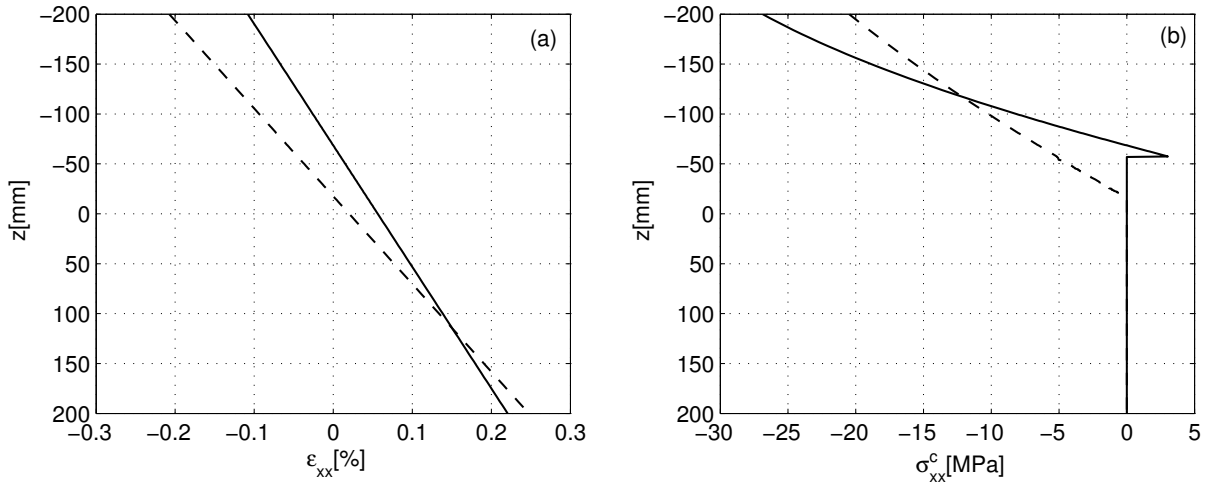

Figure 4. Normal stress and strain distributions at midspan (example 1): (a) strains and (b) stresses (the solid line is $t = 0$ and the dashed is $t = 3$ years).

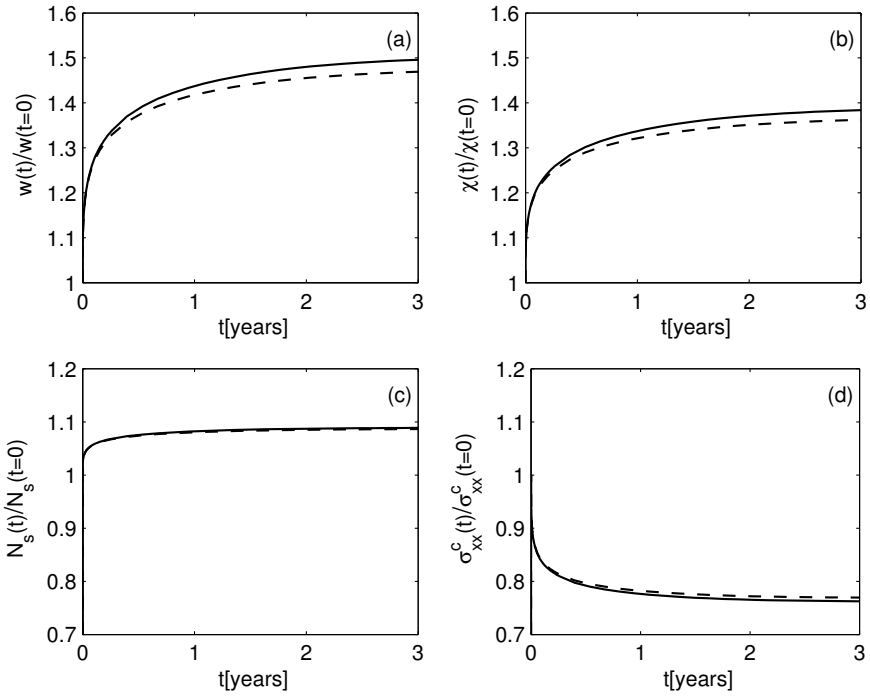

Figure 5. Normalized creep response at midspan: (a) vertical deflection, (b) curvature, (c) axial force in the reinforcement, and (d) maximum compressive stress in the concrete (the solid line indicates no aging and the dashed with aging).

response which reveal a central deflection of $w(t=0) = 13.19\,\text{mm}$, a curvature of $\chi(t=0) = 0.0082\,1/\text{m}$ and a peak steel force of $N_s(t=0) = 354.6\,\text{kN}$. The results show that the normalized increase of the deflection is larger than that of the curvature, which in turn is much larger than the increase in the reinforcement force. Thus, creep has different effects on the structural response, which requires careful attention especially when material nonlinearity is included. Nevertheless, due to cracking and the restrain of creep by the steel reinforcement, the creep amplification of the deformations and forces is much less than 2.9, which is the case in a linear homogeneous material (other than reinforced concrete) with a creep coefficient of 1.9 after 3 years. The results also show that aging has a small effect on the deformations, along with a negligible effect on the forces and stresses. In both cases, the cracked region slightly propagates along the beam due to tensile creep rupture, and its left edge moves from $X_{\text{cr1}} = 166.7\,\text{mm}$ to $X_{\text{cr1}} = 150\,\text{mm}$ after 3 years.

To further clarify the structural response, the effects of the load level as well as the shrinkage strains are examined in Figure 6. Aging is accounted for, and all other reference parameters including the loading and material properties are kept unchanged. The instantaneous failure load of the beam is calculated as $q_z^u = 76\,\text{kN/m}$, for which yielding of the steel reinforcement occurs. The results show that increasing the load level leads to a decrease in the normalized peak deflection and steel force, and consequently to a smaller release of the peak compressive stresses. A similar conclusion was also reported in [Tan and Saha 2006], yet mainly for RC beams strengthened with composite materials. No creep rupture in

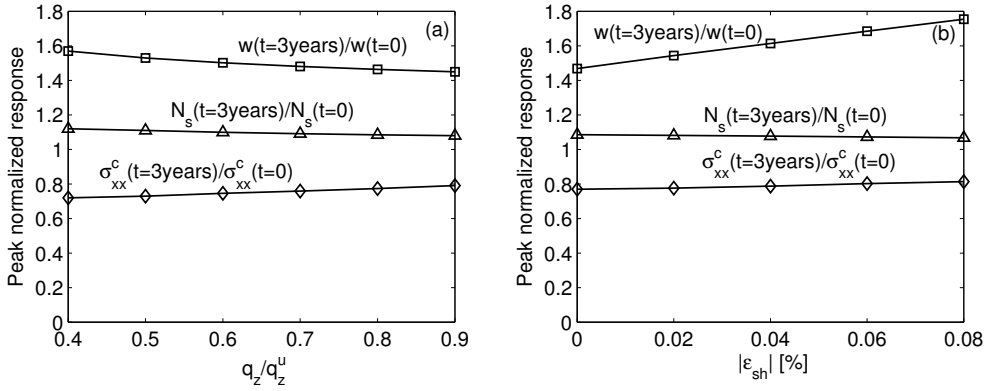

Figure 6. Effect of (a) load level and (b) shrinkage strain on the long-term response.

compression is observed in all cases examined here due to the rapid release of the peak compressive stresses a short time after loading as can be seen in Figure 5d. This is believed to be the case in most RC beams under bending only.

On the other hand, shrinkage seems to significantly increase the deflections but with much smaller effect on the axial force and stresses. The normalized long-term deflection is increased due to shrinkage from 1.47 the instantaneous deflection for $\varepsilon_{\rm sh} = 0$ to about 1.76 the instantaneous deflection for $\varepsilon_{\rm sh} = -0.08\%$; this is a significant increase of 62% in the long-term effects. Shrinkage also leads to further shifting down of the neutral axis and to a smaller increase of the reinforcement axial force and less release of the stresses as the magnitude of the shrinkage strain increases. In addition, the long-term cracking length is also affected by shrinkage, and its left edge decreases from $X_{\rm cr1} = 150\,$mm for $\varepsilon_{\rm sh} = 0$ to $X_{\rm cr1} = 0$ for $\varepsilon_{\rm sh} \le -0.06\%$.

The effect of the reinforcement ratio of both the compressed and tensioned steel is investigated in Figure 7. Also here, aging is accounted for, and all other reference parameters are kept unchanged; z'_s is taken as $-170\,$mm. As indicated in many studies [Washa and Fluck 1952; Neville and Dilger 1970], the results show that the compressed steel reinforcement significantly restrains the creep effects and leads to

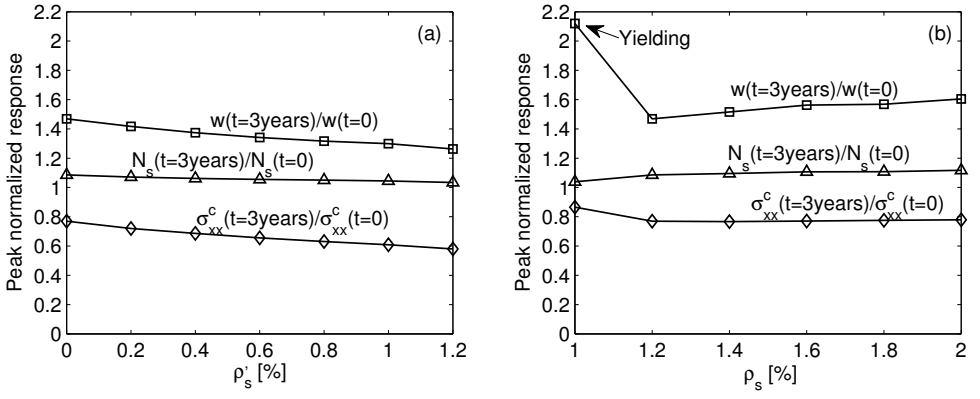

Figure 7. Effect of (a) compressed and (b) tensioned reinforcement ratios.

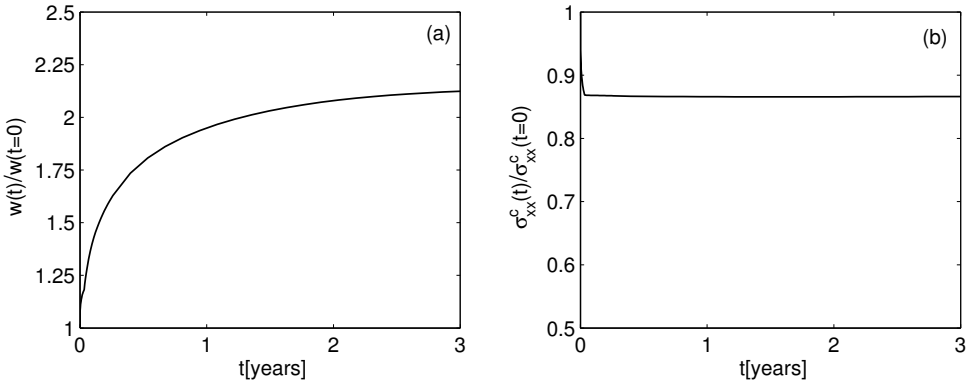

Figure 8. Normalized creep response at midspan with yielding of the reinforcement: (a) vertical deflection and (b) maximum compressive stress in the concrete.

smaller long-term deflections. The proposed model, which is able to quantitatively predict this effect for the nonlinear case, also shows that this is associated with a slight decrease of the normalized axial force, as well as a considerable release of the peak compressive stresses in the concrete.

Figure 7b shows that for $1.2\% \leq \rho_s$, increasing the tensioned reinforcement ratio leads to an increase in the normalized deflection and axial forces, and a further release of the stresses. The reason for that is the increase in the area of the cross-section under compression with the increase of the reinforcement ratio. As creep is proportional to the level of stresses, which are much larger in compression than in tension, the larger the area under compression the more creep deformations develop. The relatively high normalized deflection observed with $\rho_s = 1.0\%$ is a result of yielding with time of the tensioned reinforcement. To clarify this, the time variation of the central deflection and peak compressive stress in the concrete appear in Figure 8 for this case. After yielding of the steel reinforcement at $t = 14$ days after loading, the concrete starts to creep freely without the restrain of the reinforcement. As a result, the neutral axis remains unchanged and no further stress relaxation occurs; hence we have the relatively high peak normalized deflection, which is about 2.12.

4.2. ***Second example: Beam under bending and compression.*** The RC beam examined in Section 4.1 is investigated here under a combination of both vertical and axial compression loadings (which may simulate a beam-column or a prestressed beam). The vertical load is as earlier while the axial compression load equals 1200 kN. Aging is accounted for while no compressed reinforcement and no shrinkage effects are included in the analysis. The distributions of the instantaneous and long-term normal strains and stresses are shown in Figure 9. The results show that in this case there is a relatively small shifting of the neutral axis down as most of the beam cross-section is under compression. Consequently only a slight change in the stress distribution is observed over time. However, it can be seen that creep rupture in compression occurred at some points that were under high levels of instantaneous stresses. Although the model provides a description of the response beyond first creep rupture, unlike creep rupture in tension, the time for which first creep rupture in compression occurs can be defined as a critical time (t_{cr}) as it may initiate total failure of the structure. In this example it equals 155 days.

The time variations of the central deflection and peak force in the reinforcement are shown in Figure 10. The results are normalized with respect to the instantaneous response which reveals a central deflection of

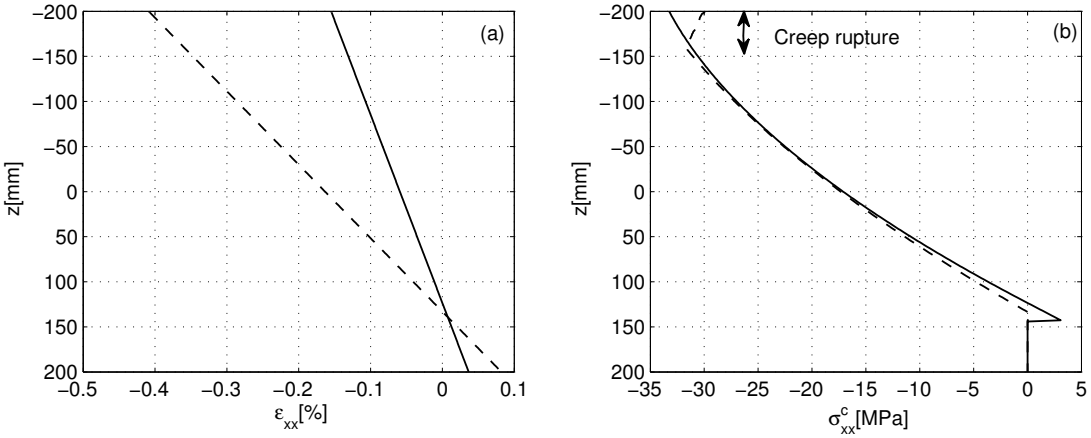

Figure 9. Normal stress and strain distributions at midspan (example 2): (a) strains and (b) stresses (the solid line is $t = 0$ and the dashed $t = 3$ years).

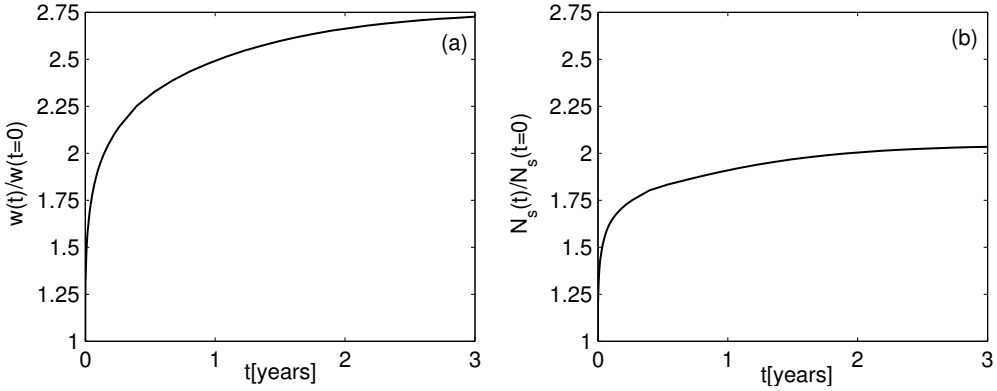

Figure 10. Normalized creep response at midspan (example 2): (a) vertical deflection and (b) axial force in the reinforcement.

$w(t = 0) = 7.5$ mm and a peak steel force of $N_s(t = 0) = 40.3$ kN. It can be seen that the normalized long-term amplifications of the deflection and reinforcement force due to creep are much larger than the ones obtained in Figure 5, due to the fact that the majority of the beam cross-section is under compression.

The dependence of the critical time to cause first creep rupture in compression on the level of the applied vertical load is shown in Figure 11. As expected, the critical time significantly decreases with the increase of the applied load. However, it is interesting to see that the logarithm of the critical time is almost linearly proportional to the level of the applied load. For $q_z < 0.7q_z^u$, no creep rupture is observed even 50 years after first loading. These observations are important for the design and the safety assessment of RC beams under high levels of sustained lateral and axial loadings, as creep may actually reduce the design life of such structures.

4.3. ***Comparison with test results.*** Only few detailed test results are available on the creep behavior of RC beams in general, and their nonlinear creep behavior in particular. Here, the test results reported in [Washa and Fluck 1952; Bakoss et al. 1982; Tan and Saha 2006] are used. Although the first two studies

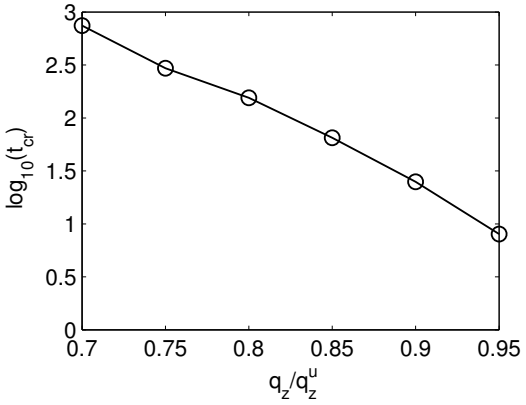

Figure 11. Variation of the critical time versus the initially applied vertical load.

focus on the creep behavior under linear stress levels, they provide a level of verification to the proposed model.

Bakoss et al. [1982] describe creep testing of a RC beam including experimental characterization of the creep and shrinkage material properties. The beam is simply supported with a span of 3504 mm, and is loaded in four points bending with sustained loads of 2.6 kN each applied at the third-points of the span. The beam has a rectangular cross section of 100/150 mm, and includes two 12 mm diameter deformed bars located at 20 mm from the bottom face of the beam. The reported compressive strength and modulus of elasticity are 39 MPa and 31.2 GPa, respectively, while following [CEB-FIP 1990], f_{ctm} and ε_c are taken as 3.47 MPa and -0.237%, respectively. The reported creep coefficient at $t = 560$ days and the shrinkage strain at $t = 775$ days that were measured from separate small specimens are 2.5 and -700×10^{-6}, respectively. It is assumed here that their development with time follows [CEB-FIP 1990]. Also here, seven Maxwell units are used with $T_\mu = 0.1 \times 5^{\mu-1}$ days, for $\mu = 1, \ldots, 6$. For brevity, only the strain-independent parts of the spring moduli are reported here, as they are also the dominant parts due to the low level of sustained loading with linear stresses. Thus, $\bar{E}_\mu = \left[7.088 \;\; 2.132 \;\; 3.726 \;\; 3.947 \;\; 3.417 \;\; 2.877 \;\; 7.982\right]$ GPa.

Figure 12 shows the predicted and the measured time variation of the central deflection. Despite the unexpected sharp increase of the experimental deflection around $t = 250$ days, which can be due to environmental or other effects, the comparison reveals a reasonably good correlation between the results. The instantaneous deflection reported in the test is 8.94 mm, while the predicted one is 9.07 mm. The differences in the long-term deflections can be due to many factors including the different creep behavior of concrete in tension, compression, and bending, the use of a smeared cracking model, temperature and humidity changes, and other related factors.

Six beams (three pairs: A1, A4; A2, A5; and A3, A6) from the experimental investigation [Washa and Fluck 1952] are selected for the comparison. The beams were simply supported with a span of 6100 mm, and were loaded by concrete blocks to simulate a uniformly distributed load of 5.512 kN/m. All beams (A1–A6) have a rectangular cross section of 203/305 mm and include three bars of 19 mm diameter in tension. In addition, beams A2 and A5 include two 16 mm bars in compression, while beams A1 and A4 have symmetric reinforcement with three bars of 19 mm in compression. The reported

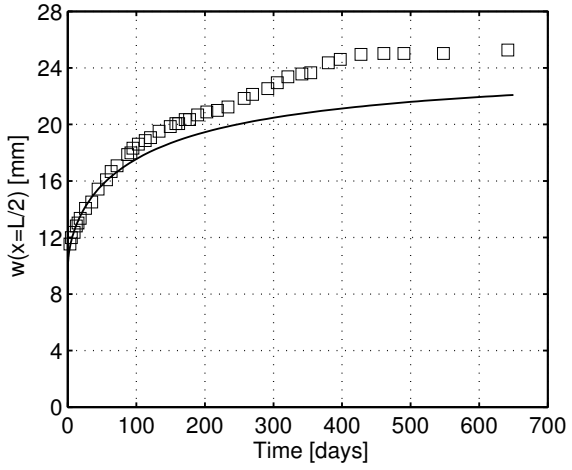

Figure 12. Theoretical versus experimental [Bakoss et al. 1982] results (the solid line is the proposed model and the squares the experimental results).

compressive strengths and moduli of elasticity vary between the different specimens in the range of $f_{ck} = 20.7$–29.3 MPa and $E_0 = 20.7$–23.8 GPa. For the numerical comparison, average values of $f_{ck} = 25.82$ MPa and $E_0 = 22.17$ GPa are chosen due to the low level of sustained loading where material nonlinearity has small influence. The creep coefficient and the shrinkage strain are estimated from the measured gross and net plastic flow in a cylinder prisms as 5 and -757×10^{-6}, respectively. Based on [CEB-FIP 1990], the following parameters are determined: $f_{ctm} = 3.15$ MPa and $\varepsilon_c = -0.218\%$. For brevity, only the strain-independent part of the spring moduli are reported with relaxation times taken as in the previous example. Thus, $\bar{E}_\mu = \begin{bmatrix} 7.44 & 1.671 & 2.945 & 2.639 & 2.046 & 1.768 & 3.63 \end{bmatrix}$ GPa.

Table 1 shows the predicted w_{th} versus the measured w_{exp} instantaneous and long-term deflections 2.5 years after first loading. The experimental results are the average between the two similar beams. A good correlation between the results with a maximum difference of less than 16% can be observed. Additionally, it can be seen from the experimental results that the ratio between the long-term deflection and the instantaneous one significantly decreases with the addition of compressive reinforcement (2.63 for A3 and 1.75 for A1), as was discussed earlier (Figure 7). The predicted ratios are 3.18 for A3 and 1.57 for A1.

The experimental study reported in [Tan and Saha 2006] included testing of RC beams under high levels of sustained loads, that is, 70% and 80% of the ultimate load ($P_u = 26.8$ kN), which introduces a level of nonlinearity into the behavior. The beams were simply supported with a span of 1800 mm, and were symmetrically loaded by four point loads. The beams were 100/125 mm in cross-section and included

Beam	w_{exp} $(t = 0)$	w_{th} $(t = 0)$	w_{exp} $(t = 2.5$ years$)$	w_{th} $(t = 2.5$ years$)$
A1, A4	13.46	12.84	23.62	20.18
A2, A5	15.75	13.7	32.26	27.32
A3, A6	17	14.7	44.7	46.86

Table 1. Predicted versus measured [Washa and Fluck 1952] central deflection in mm.

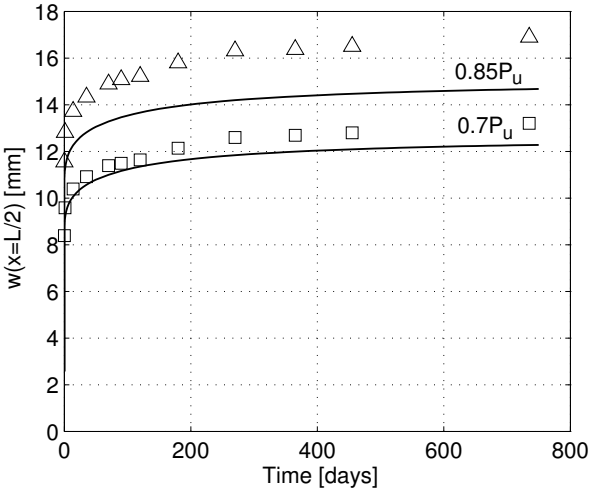

Figure 13. Theoretical versus experimental [Tan and Saha 2006] results (the solid line is the proposed model, the squares the experimental results under $0.7P_u$, and the triangles the experimental results under $0.85P_u$).

two bars of 10 mm diameter in tension and two bars of 6 mm in compression. The reported compressive strength, tensile strength, and modulus of elasticity are 40 MPa, 4.67 MPa, and 27.2 GPa, respectively, while ε_c was taken as -0.238%. The relaxation times were chosen as in the previous examples, while the spring moduli took the following strain-dependent form (in GPa) following (43):

$$\begin{bmatrix} \bar{E}_1 \\ \bar{E}_2 \\ \bar{E}_3 \\ \bar{E}_4 \\ \bar{E}_5 \\ \bar{E}_6 \\ \bar{E}_7 \end{bmatrix} = \begin{bmatrix} 5.094 & -7.642 & -5.382 & -2.307 & -3.649 \\ 1.677 & -1.719 & -1.211 & -0.519 & -0.82 \\ 2.98 & -2.847 & -2.005 & -0.859 & -1.36 \\ 3.365 & -1.896 & -1.335 & -0.572 & -0.904 \\ 3.098 & -0.742 & -0.522 & -0.223 & -0.356 \\ 2.358 & 0.134 & 0.943 & 0.396 & 0.652 \\ 8.607 & 4.311 & 3.036 & 1.302 & 2.058 \end{bmatrix} \begin{bmatrix} 1 \\ \varepsilon_{xx}^{\mathrm{v}} \\ (\varepsilon_{xx}^{\mathrm{v}})^2 \\ (\varepsilon_{xx}^{\mathrm{v}})^3 \\ (\varepsilon_{xx}^{\mathrm{v}})^4 \end{bmatrix}. \tag{47}$$

The comparison between the theoretical and experimental results is shown in Figure 13, and reveals a reasonable agreement between the results (a maximum difference of less than 15%). It is not clearly seen in the figure, but the first day after loading is associated with a significant increase of the deflections of up to 14% of the instantaneous deflection, which is also predicted by the model. Additionally, the experimental observations confirm the results appearing in Figure 6 to some extent, where the ratio between the long-term deflection and the instantaneous one decreases with the increase of the level of the applied load (1.57 for $0.7P_u$ and 1.46 for $0.85P_u$).

5. Conclusions

The nonlinear creep response and the time-dependent cracking and creep rupture behavior of reinforced concrete (RC) beams have been discussed and investigated. A theoretical model has been developed,

which highlights the challenges associated with nonlinear creep modeling, and takes into account the effects of time-dependent cracking, creep rupture in compression, yielding of the reinforcement, shrinkage, and aging of the concrete material, via the nonlinear modified principle of superposition. The interaction between these parameters and their influence on the nonlinear creep response of RC beams have been highlighted through numerical and parametric studies.

The results have shown that due to the rapid release of the stresses after first loading, creep rupture in compression of flexural RC beams can rarely happen. However, with the existence of an axial compression force, creep rupture may dominate the structural behavior and reduce the load-carrying capacity of the member. In other words, under some circumstances, creep may continuously decrease the strength of RC beams. It has been shown that the critical time to cause creep rupture failure is very sensitive to the magnitude of the applied load, and it exponentially decreases with the increase of the load level. In addition, it has been observed that the amplifications due to creep of the deflection, curvature, and axial force in the reinforcement are different, and require detailed analysis for their assessment. Shrinkage and compressed reinforcement have been shown to play important roles in the long-term response, where the former tends to significantly increase the deformation and the cracked region, while the latter restrain these effects. A comparison with experimental results has been presented, which has revealed a reasonably good agreement between the results, and has provided a level of validation for the proposed model. Some of the test results observed in other studies have also been explained and clarified using the model.

Finally, it can be concluded that the nonlinear creep response of RC beams exhibits various physical phenomena that need to be fully understood and clarified. The analytical model developed in this paper explains some of these aspects, and provides a numerical tool and a theoretical basis for the nonlinear creep analysis of other RC members.

References

[Bakoss et al. 1982] S. L. Bakoss, R. I. Gilbert, K. A. Faulkes, and V. A. Pilmano, "Long-term deflections of reinforced concrete beams", *Mag. Concr. Res.* **34**:121 (1982), 203–212.

[Bažant and Asghari 1977] Z. P. Bažant and A. A. Asghari, "Constitutive law for nonlinear creep of concrete", *J. Eng. Mech. Div.* (*ASCE*) **103**:1 (1977), 113–124.

[Bažant and Chern 1985] Z. P. Bažant and J.-C. Chern, "Strain softening with creep and exponential algorithm", *J. Eng. Mech.* (*ASCE*) **111**:3 (1985), 391–415.

[Bažant and Oh 1984] Z. P. Bažant and B. H. Oh, "Deformation of progressively cracking reinforced concrete beams", *ACI J.* **81**:3 (1984), 268–278.

[Bažant and Prasannan 1989] Z. P. a. Bažant and S. Prasannan, "Solidification theory for concrete creep, I: Formulation", *J. Eng. Mech.* (*ASCE*) **115**:8 (1989), 1691–1703.

[Bažant and Wu 1974] Z. P. Bažant and S. T. Wu, "Rate-type creep law of aging concrete based on Maxwell chain", *Mater. Struct.* **7**:1 (1974), 45–60.

[Bockhold and Petryna 2008] J. Bockhold and Y. Petryna, "Creep influence on buckling resistance of reinforced concrete shells", *Comput. Struct.* **86**:7-8 (2008), 702–713.

[Brueller and Steiner 1993] O. S. Brueller and H. Steiner, "Creep-based characterization of nonlinear relaxation behavior of plastics", *Polym. Eng. Sci.* **33**:21 (1993), 1400–1403.

[Carol and Bažant 1993] I. Carol and Z. P. Bažant, "Viscoelasticity with aging caused by solidification of nonaging constituent", *J. Eng. Mech.* (*ASCE*) **119**:11 (1993), 2252–2269.

[Carol and Murcia 1989] I. Carol and J. Murcia, "A model for the non-linear time-dependent behaviour of concrete in compression based on a Maxwell chain with exponential algorithm", *Mater. Struct.* **22**:3 (1989), 176–184.

[CEB-FIP 1990] CEB-FIP, *Design Code*, Comité Euro-International du Beton, Thomas Telford House, London, 1990.

[CEB-FIP 1999] CEB-FIP, *Structural concrete. Textbook on behaviour, design and performance. Updated knowledge of the CEB/FIP Model Code 1990*, Comité Euro-International du Béton/Fédération International de la Précontrainte, Fib-bulletin no. 1, Lausanne, Switzerland, 1999.

[Di Luzio 2009] G. Di Luzio, "Numerical model for time-dependent fracturing of concrete", *J. Eng. Mech.* (*ASCE*) **135**:7 (2009), 632–610.

[Fernández Ruiz et al. 2007] M. Fernández Ruiz, A. Muttoni, and P. G. Gambarova, "Relationship between nonlinear creep and cracking of concrete under uniaxial compression", *J. Adv. Concr. Technol.* **5**:3 (2007), 383–393.

[Findley et al. 1976] W. N. Findley, J. S. Lai, and K. Onran, *Creep and relaxation of nonlinear viscoelastic materials, with an introduction to linear viscoelasticity*, North-Holland, Amsterdam, 1976.

[Gilbert 1988] R. I. Gilbert, *Time effects in concrete structures*, Elsevier, Amsterdam, 1988.

[Gilbert 2007] R. I. Gilbert, "Tension stiffening in lightly reinforced concrete slabs", *J. Struct. Eng.* (*ASCE*) **133**:6 (2007), 899–903.

[Hamed and Rabinovitch 2008] E. Hamed and O. Rabinovitch, "Nonlinear dynamic behavior of unreinforced masonry walls subjected to out-of-plane loads", *J. Struct. Eng.* (*ASCE*) **134**:11 (2008), 1743–1753.

[Hamed et al. 2011] E. Hamed, M. A. Bradford, R. I. Gilbert, and Z. T. Chang, "Analytical model and experimental study of failure behavior of thin-walled shallow concrete domes", *J. Struct. Eng.* (*ASCE*) **137**:1 (2011), 88–99.

[Leaderman 1943] H. Leaderman, *Elastic and creep properties of filamentous materials and other high polymers*, The Textile Foundation, Washington DC, 1943.

[Li and Qian 1989] Z. Li and J. Qian, "Creep damage analysis and its application to nonlinear creep of reinforced concrete beam", *Eng. Fract. Mech.* **34**:4 (1989), 851–860.

[Mazzotti and Savoia 2003] C. Mazzotti and M. Savoia, "Nonlinear creep damage model for concrete under uniaxial compression", *J. Eng. Mech.* (*ASCE*) **129**:9 (2003), 1065–1075.

[Neville and Dilger 1970] A. M. Neville and W. H. Dilger, *Creep of concrete: plain, reinforced, and prestressed*, North-Holland, Amsterdam, 1970.

[Omar et al. 2009] M. Omar, A. Loukili, G. Pijaudier-Cabot, and Y. Le Pape, "Creep-damage coupled effects: experimental investigation on bending beams with various sizes", *J. Mater. Civ. Eng.* (*ASCE*) **21**:2 (2009), 65–72.

[Oza et al. 2003] A. Oza, R. Vanderby, and R. S. Lakes, "Interrelation of creep and relaxation for nonlinearly viscoelastic materials: application to ligament and metal", *Rheol. Acta* **42**:6 (2003), 557–568.

[Papa et al. 1998] E. Papa, A. Taliercio, and E. Gobbi, "Triaxial creep behaviour of plain concrete at high stresses: a survey of theoretical models", *Mater. Struct.* **31**:7 (1998), 487–493.

[Pipkin and Rogers 1968] A. Pipkin and T. Rogers, "A non-linear integral representation for viscoelastic behaviour", *J. Mech. Phys. Solids* **16**:1 (1968), 59–72.

[Rabinovitch and Frostig 2001] O. Rabinovitch and Y. Frostig, "Nonlinear high-order analysis of cracked RC beams strengthened with FRP strips", *J. Struct. Eng.* (*ASCE*) **127** (2001), 381–389.

[Rots and Blaauwendraad 1989] J. G. Rots and J. Blaauwendraad, "Crack models for concrete: discrete or smeared? fixed, multi-directional or rotating?", *Heron* **34**:1 (1989), 1–59.

[Rots and de Borst 1987] J. G. Rots and R. de Borst, "Analysis of mixed-mode fracture in concrete", *J. Eng. Mech.* (*ASCE*) **113**:11 (1987), 1739–1758.

[Santhikumar et al. 1998] S. Santhikumar, B. L. Karihaloo, and G. Reid, "A model for ageing visco-elastic tension softening material", *Mech. Cohes. Frict. Mater.* **3** (1998), 27–39.

[Sorvari and Hämäläinen 2010] J. Sorvari and J. Hämäläinen, "Time integration in linear viscoelasticity: a comparative study", *Mech. Time-Depend. Mater.* **14**:3 (2010), 307–328.

[Stoer and Bulirsch 2002] J. Stoer and R. Bulirsch, *Introduction to numerical analysis*, Springer, 2002.

[Tan and Saha 2006] K. H. Tan and M. K. Saha, "Long-term deflections of reinforced concrete beams externally bonded with FRP system", *J. Compos. Constr.* (*ASCE*) **10**:6 (2006), 474–482.

[Taylor et al. 1970] R. Taylor, K. Pister, and G. Goudreau, "Thermomechanical analysis of viscoelastic solids", *Int. J. Numer. Methods Eng.* **2**:1 (1970), 45–59.

[Touati and Cederbaum 1997] D. Touati and G. Cederbaum, "Stress relaxation of nonlinear thermoviscoelastic materials predicted from known creep", *Mech. Time-Depend. Mater.* **1**:3 (1997), 321–330.

[Washa and Fluck 1952] G. W. Washa and P. G. Fluck, "Effect of compressive reinforcement on the plastic flow of reinforced concrete beams", *ACI J.* **49**:10 (1952), 89–108.

[Zhou 1994] F. P. Zhou, "Numerical modelling of creep crack growth and fracture in concrete", pp. 141–148 in *Localized damage III: computer-aided assessment and control*, edited by M. H. Aliabadi et al., Transactions on Engineering Sciences **6**, WIT Press, Ashurst Lodge, Southampton, 1994.

Received 24 Nov 2011. Revised 9 Feb 2012. Accepted 21 Feb 2012.

EHAB HAMED: e.hamed@unsw.edu.au
Centre for Infrastructure Engineering and Safety, The School of Civil and Environmental Engineering, The University of New South Wales, Sydney, NSW 2052, Australia

JOURNAL OF MECHANICS OF MATERIALS AND STRUCTURES
Vol. 7, No. 5, 2012
dx.doi.org/10.2140/jomms.2012.7.461

msp

NEW INVARIANTS IN THE MECHANICS OF DEFORMABLE SOLIDS

VIKTOR V. KUZNETSOV AND STANISLAV V. LEVYAKOV

A system of invariants of symmetric three-dimensional tensors of second order is proposed in a new form. The system contains three classical invariants of a tensor and three new invariants which depend on the components of two or three tensors. The system proposed allows one to express the strain energy density of a linear elastic anisotropic body and virtual work done by internal stresses in terms of the invariants for any constitutive law of the material. Application of the invariants to the derivation of the tetrahedron finite element of anisotropic solids is discussed.

1. Introduction

Invariants of the strain and stress tensors known as frame-indifferent (or objective) measures are considered in almost every book on the theory of elasticity (see, for example, [Sneddon and Berry 1958; Timoshenko and Goodier 1970; Antman 1995]). In contrast to the tensorial components whose values depend on the coordinate system chosen, the values of invariants remain unchanged regardless of the coordinate system used to evaluate them. In the theory of elasticity, invariants are introduced as coefficients of the characteristic polynomial equation of the standard eigenvalue problem to find the principal directions of the strain and stress tensors. Alternatively, the invariants can be obtained by decomposing the ratio of an elementary volume in a deformed state to that in the undeformed state into linear, quadratic, and cubic forms in the tensor components [Kuznetsov and Levyakov 2009].

In theoretical studies, invariants provide a convenient tool for a compact representation of constitution relations and strain energy density of a deformable solid. Since the strain energy is a scalar, it must be represented as a function of invariants of the tensors governing the stress-strain state of the solid. For an isotropic homogeneous material, this expression in terms of the stress or strain tensor invariants is known [Timoshenko and Goodier 1970]. But to the authors' best knowledge, no similar expression is available in the literature for anisotropic or even orthotropic materials.

In the present paper, the question of determining the strain energy density of an anisotropic solid in terms of invariants in the form different from [Timoshenko and Goodier 1970] is studied. Symmetric three-dimensional tensors of second order are considered and a system of invariants of the tensors is proposed. The system comprises three traditional invariants of the tensor and three new quantities called the combined invariants. It is shown that the strain energy density of a linear elastic anisotropic body can be represented as a function of these invariants.

The property of the invariants can be valuable in formulating computationally effective numerical algorithms for analysis of stresses and strain of deformable solids. In the finite element method, the stiffness equations are formulated in a local coordinate system introduced for each finite element of

Keywords: tensors, invariants, anisotropic material, strain, stress, tetrahedral finite element.

the structure. To construct the finite-element assemblage, these equations are transformed to global coordinate axes. The coordinate transformations can be eliminated using invariants, which can reduce computer time. The time reduction can be pronounced in the nonlinear analysis based on the Newton-Raphson type techniques where stiffness relations of each element are updated at each iteration. Below, application of the invariant based approach to the finite-element analysis of solids is briefly discussed.

2. Invariants of three-dimensional tensors

We consider a second-order three-dimensional tensor $\boldsymbol{S}$ with covariant components S_{ij} $(i, j = 1, 2, 3)$ determined in a convective coordinate system $\alpha^1, \alpha^2, \alpha^3$ characterized by metric tensor $\boldsymbol{A}$ with covariant components

$$A_{ij} = \frac{\partial \boldsymbol{R}}{\partial \alpha^i} \frac{\partial \boldsymbol{R}}{\partial \alpha^j},$$

where $\boldsymbol{R}$ is the position vector. The first, second, and third invariants of the tensor $\boldsymbol{S}$ in the metric $\boldsymbol{A}$ are given by

$$I_S = \frac{1}{2\Delta} \varepsilon_{ijk} \varepsilon_{pqr} S_{ip} A_{jq} A_{kr}, \tag{2-1}$$

$$I_{S^2} = \frac{1}{2\Delta} \varepsilon_{ijk} \varepsilon_{pqr} S_{ip} S_{jq} A_{kr}, \tag{2-2}$$

$$I_{S^3} = \frac{1}{6\Delta} \varepsilon_{ijk} \varepsilon_{pqr} S_{ip} S_{jq} S_{kr}, \tag{2-3}$$

where

$$\varepsilon_{ijk} = \tfrac{1}{2}(i - j)(j - k)(k - i) \tag{2-4}$$

is the Levi-Civita symbol and

$$\Delta = \det \|A_{ij}\| = \tfrac{1}{6} \varepsilon_{ijk} \varepsilon_{pqr} A_{ip} A_{jq} A_{kr} \tag{2-5}$$

is the discriminant of the metric tensor.

In these equations and below, summation is performed over repeated indices which run from 1 to 3. Formulas (2-1)–(2-3) are based on the results of [Kuznetsov and Levyakov 2009] and written here in a new unified manner to show the rule according to which the invariants are formed. Writing the invariants of the tensor $\boldsymbol{S}$ in terms of its principal values S_i, we obtain the well-known expressions [Timoshenko and Goodier 1970]

$$I_S = S_1 + S_2 + S_3, \quad I_{S^2} = S_1 S_2 + S_2 S_3 + S_3 S_1, \quad I_{S^3} = S_1 S_2 S_3. \tag{2-6}$$

Let the tensor $\boldsymbol{S}$ be decomposed into three symmetric tensors $\boldsymbol{U}$, $\boldsymbol{V}$, and $\boldsymbol{W}$ such that $\boldsymbol{S} = \boldsymbol{U} + \boldsymbol{V} + \boldsymbol{W}$. In this case, (2-1)–(2-3) become

$$I_S = I_U + I_V + I_W, \tag{2-7}$$

$$I_{S^2} = I_{U^2} + I_{V^2} + I_{W^2} + 2(I_{UV} + I_{UW} + I_{VW}), \tag{2-8}$$

$$I_{S^3} = I_{U^3} + I_{V^3} + I_{W^3} + 3(I_{UV^2} + I_{UW^2} + I_{VU^2} + I_{VW^2} + I_{WU^2} + I_{WV^2}) + 6I_{UVW}. \tag{2-9}$$

These expressions contain three known invariants determined by (2-1)–(2-3) and three new invariants given by

$$I_{UV} = \frac{1}{2\Delta}\varepsilon_{ijk}\varepsilon_{pqr}U_{ip}V_{jq}A_{kr}, \tag{2-10}$$

$$I_{UV^2} = \frac{1}{6\Delta}\varepsilon_{ijk}\varepsilon_{pqr}U_{ip}V_{jq}V_{kr}, \tag{2-11}$$

$$I_{UVW} = \frac{1}{6\Delta}\varepsilon_{ijk}\varepsilon_{pqr}U_{ip}V_{jq}W_{kr}. \tag{2-12}$$

We call these expressions, which depend on the components of two or three tensors, the combined invariants. One can easily show that decomposition of $\boldsymbol{S}$ into more than three symmetric tensors does not lead to any new invariants. Obviously, expressions (2-1)–(2-3) and (2-10)–(2-12) are valid for any symmetric three-dimensional tensors of second order. For this reason, we refer to them as templates.

The invariants determined by formulas (2-1)–(2-3) and (2-10)–(2-12) constitute a complete system that allows one to obtain invariant forms of the first, second, and third degrees containing components of any number of symmetric tensors. The invariant I_{UV} is the bilinear invariant of two tensors, I_{UV^2} is the linear-quadratic invariant of two tensors, and I_{UVW} is the trilinear invariant of three tensors. It should be noted that the invariant I_{UVW} is of general character: all the invariants mentioned above fall out as particular cases from (2-12), namely

$$I_S = 3I_{SAA}, \quad I_{S^2} = 3I_{SSA}, \quad I_{S^3} = I_{SSS}, \quad I_{UV} = 3I_{UVA}, \quad I_{UV^2} = I_{UVV}. \tag{2-13}$$

In Cartesian coordinates, where $A_{ij} = \delta_{ij}$ (the Kronecker symbol) and $\Delta = 1$, the invariants considered above become

$$I_U = \delta_{ij}U_{ij}, \qquad I_{U^2} = \tfrac{1}{2}\varepsilon_{ijk}\varepsilon_{iqr}U_{jq}U_{kr}, \qquad I_{U^3} = \tfrac{1}{6}\varepsilon_{ijk}\varepsilon_{pqr}U_{ip}U_{jq}U_{kr}, \tag{2-14}$$

$$I_{UV} = \tfrac{1}{2}\varepsilon_{ijk}\varepsilon_{iqr}U_{jq}V_{kr}, \quad I_{UV^2} = \tfrac{1}{6}\varepsilon_{ijk}\varepsilon_{pqr}U_{ip}V_{jq}V_{kr}, \quad I_{UVW} = \tfrac{1}{6}\varepsilon_{ijk}\varepsilon_{pqr}U_{ip}V_{jq}W_{kr}. \tag{2-15}$$

Let $\alpha'^1, \alpha'^2, \alpha'^3$ denote new convective curvilinear coordinates and assume that they are related to the coordinates $\alpha^1, \alpha^2, \alpha^3$ by

$$\alpha^i = \alpha^i(\alpha'^1, \alpha'^2, \alpha'^3) \quad (i = 1, 2, 3). \tag{2-16}$$

Now we show that the expressions (2-1)–(2-3) and (2-10)–(2-12) retain their form under general coordinate transformations (2-16). To this end, it suffices to prove the invariance of the expression for the trilinear invariant of three tensors

$$I_{U'V'W'} = I_{UVW} \tag{2-17}$$

or

$$\frac{1}{6\Delta'}\varepsilon_{ijk}\varepsilon_{pqr}U'_{ip}V'_{jq}W'_{kr} = \frac{1}{6\Delta}\varepsilon_{ijk}\varepsilon_{pqr}U_{ip}V_{jq}W_{kr}. \tag{2-18}$$

Here the primed quantities are evaluated in the coordinates α'^i. The components of any tensor considered above are transformed according to the well-known rule

$$U'_{ij} = U_{pq}\frac{\partial\alpha^p}{\partial\alpha'^i}\frac{\partial\alpha^q}{\partial\alpha'^j}. \tag{2-19}$$

We write the useful relation

$$\varepsilon_{ijk}\frac{\partial\alpha^p}{\partial\alpha'^i}\frac{\partial\alpha^q}{\partial\alpha'^j}\frac{\partial\alpha^r}{\partial\alpha'^k}=\varepsilon_{pqr}\det\boldsymbol{J}, \tag{2-20}$$

where $\boldsymbol{J}=\partial(\alpha^1,\alpha^2,\alpha^3)/\partial(\alpha'^1,\alpha'^2,\alpha'^3)$ is the Jacobian matrix of coordinate transformation.

Following (2-5), we write the discriminant of the metric tensor on the left side of (2-18) as

$$\Delta'=\tfrac{1}{6}\varepsilon_{ijk}\varepsilon_{pqr}A'_{ip}A'_{jq}A'_{kr}. \tag{2-21}$$

Expressing the components of the metric tensor A'_{ij} in terms of unprimed components according to the rule (2-19) and using relation (2-20), we obtain

$$\Delta'=(\det\boldsymbol{J})^2\Delta. \tag{2-22}$$

Performing similar manipulations for the nominator on the left side of (2-18), we find that

$$\varepsilon_{ijk}\varepsilon_{pqr}U'_{ip}V'_{jq}W'_{kr}=\varepsilon_{ijk}\varepsilon_{pqr}U_{ip}V_{jq}W_{kr}(\det\boldsymbol{J})^2. \tag{2-23}$$

Substituting (2-22) and (2-23) into the left side of (2-18), we prove the validity of (2-18).

3. Strain energy density

Now we use the results obtained above to express the stress energy density Π_V of a linear elastic anisotropic solid. In Cartesian coordinates referred to anisotropy axes of the material, we obtain

$$\Pi_V=\tfrac{1}{2}\sigma_{ij}S_{ij}, \tag{3-1}$$

where σ_{ij} and S_{ij} are the stress and strain tensors, respectively, which in general are related through 21 elastic constants. We note that the strain tensor components can be related to the displacements by linear or geometrically nonlinear relations. Expression (3-1) can be written in the invariant form as

$$\Pi_V=\tfrac{1}{2}(I_\sigma I_S-2I_{\sigma S}), \tag{3-2}$$

where I_σ and I_S are the first invariants of the stress and strain tensors, respectively, and $I_{\sigma S}$ is the combined invariant of these two tensors. These quantities can be calculated using $(2\text{-}14)_1$ and $(2\text{-}14)_4$, in which $\boldsymbol{U}$ and $\boldsymbol{V}$ are replaced with $\boldsymbol{\sigma}$ and $\boldsymbol{S}$. To prove the equivalence of (3-1) and (3-2), it suffices to employ the relation

$$\varepsilon_{ijk}\varepsilon_{iqr}=\delta_{jq}\delta_{kr}-\delta_{jr}\delta_{kq}. \tag{3-3}$$

The invariants on the right side of (3-2) imply that the strain energy density retains its value for any coordinate system. We note that the invariants appearing in (3-2) can be calculated in arbitrary curvilinear coordinates α^i $(i=1,2,3)$ using templates (2-1) and (2-10).

In a similar manner, one can easily show that the virtual work δW done by the internal stresses is invariant for any constitutive law:

$$\delta W=I_\sigma I_{\delta S}-2I_{\sigma(\delta S)}, \tag{3-4}$$

where invariants on the right side can be evaluated using templates (2-14) and (2-15) in Cartesian coordinates or (2-1) and (2-10) in curvilinear coordinates.

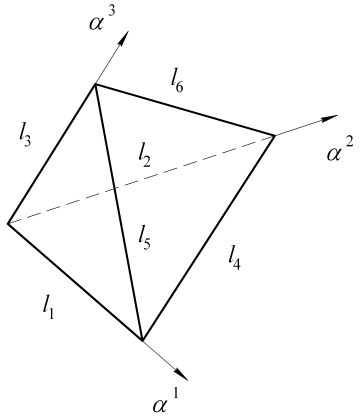

Figure 1. Tetrahedral finite element and notation.

4. Finite-element application

Let us determine the strain and stress invariants and the strain energy density for a tetrahedron finite element of a three-dimensional solid (Figure 1). The components of the metric tensor are expressed in terms of the squared lengths l_i of the elemental edges:

$$\begin{gathered} A_{11} = l_1^2, \quad A_{22} = l_2^2, \quad A_{33} = l_3^2, \quad A_{12} = A_{21} = \tfrac{1}{2}(l_1^2 + l_2^2 - l_4^2), \\ A_{13} = A_{31} = \tfrac{1}{2}(l_1^2 + l_3^2 - l_5^2), \quad A_{23} = A_{32} = \tfrac{1}{2}(l_2^2 + l_3^2 - l_6^2). \end{gathered} \tag{4-1}$$

As the physical strains and stresses, we use the normal strains S_i and stresses σ_i $(i = 1, \ldots, 6)$ in the direction of the elemental edges. Covariant components of the strain tensor are related to the physical strains by the expressions

$$\begin{gathered} S_{11} = l_1^2 S_1, \quad S_{22} = l_2^2 S_2, \quad S_{33} = l_3^2 S_3, \quad S_{12} = S_{21} = \tfrac{1}{2}(l_1^2 S_1 + l_2^2 S_2 - l_4^2 S_4), \\ S_{13} = S_{31} = \tfrac{1}{2}(l_1^2 S_1 + l_3^2 S_3 - l_5^2 S_5), \quad S_{23} = S_{32} = \tfrac{1}{2}(l_2^2 S_2 + l_3^2 S_3 - l_6^2 S_6). \end{gathered} \tag{4-2}$$

Similar relations can be written for the stress components.

Thus, the stress and strain invariants and the strain energy density can be determined by the normal components of the tensors. According to the terminology of [Argyris et al. 1979], these components are referred to as natural components which are in harmony with the tetrahedron geometry. The strain energy of the element can be evaluated by approximating the natural strains in terms of the nodal parameters and integrating over the element volume $V = \sqrt{\Delta}/6$.

Once the equilibrium state has been determined and the natural strains have been obtained, one can compute the principal values of the strain tensor as roots of the cubic equation

$$S^3 - I_S S^2 + I_{SS} S - I_{SSS} = 0. \tag{4-3}$$

The principal stresses can be obtained in a similar manner.

A complete system of invariants of two-dimensional tensors defined on a plane or a surface is given in the Appendix.

5. Concluding remarks

A system of invariants of symmetric three-dimensional tensors of second order has been proposed. The invariants have been determined by ratios of certain third-order determinants depending on the covariant components of the tensors. The system comprises the well-known three invariants of one tensor and three new combined invariants which depend on the components of two or three tensors. The first new invariant is a bilinear invariant of two tensors, the second is a linear-quadratic invariant of two tensors, and the third is a trilinear invariant of three tensors. These invariants have been expressed in a unified manner to show the rule according to which they are formed. The trilinear invariant of three tensors is of general structure in the sense that the other invariants considered in the paper fall out as particular cases. This implies that the system of invariants is complete. It can be used to form any invariant forms of the first, second, and third degrees which depend on the components of any number of tensors and also to prove the invariance of other expressions. It has been shown that the strain-energy density and virtual work of an anisotropic solid can be expressed in terms of invariants where the bilinear invariant of the strain and stress tensors plays a key role.

As an example of application of the invariants, relations have been given to evaluate the strain energy of a tetrahedron finite element of an anisotropic solid in terms of natural physical components of the strains and stresses in the direction of the element edges.

Appendix. Invariants of two-dimensional tensors

Let a symmetric two-dimensional tensor $\boldsymbol{E}$ with covariant components E_{ij} $(i, j = 1, 2)$ be determined in a convective curvilinear coordinate system α^1, α^2 on a plane or surface characterized by the metric tensor a with covariant components a_{ij}. The first and second invariants of the tensor $\boldsymbol{E}$ in metrics $\boldsymbol{a}$ are given by

$$I_E = \frac{1}{\Delta} e_{mp} e_{nq} a_{pq} E_{mn}, \quad I_{E^2} = \frac{1}{2\Delta} e_{mp} e_{nq} E_{pq} E_{mn}, \quad \Delta = \frac{1}{2} e_{mp} e_{nq} a_{pq} a_{mn}, \tag{A-1}$$

where e_{mp} is the permutation tensor whose components are given by $e_{11} = e_{22} = 0$ and $e_{12} = -e_{21} = 1$ and Δ is the discriminant of the metric tensor. In (A-1) and below, summation is performed over repeated indices running from 1 to 2.

We assume that the tensor $\boldsymbol{E}$ is a sum of two tensors $\boldsymbol{U}$ and $\boldsymbol{V}$. In this case, the invariants in (A-1) become

$$I_E = I_U + I_V, \quad I_{E^2} = I_{U^2} + I_{V^2} + 2I_{UV}. \tag{A-2}$$

Here I_{UV} is the combined invariant of two tensors written as

$$I_{UV} = \frac{1}{2\Delta} e_{mp} e_{nq} U_{pq} V_{mn}. \tag{A-3}$$

This invariant is of general nature since the first and second invariants can be obtained from (A-3) as particular cases:

$$I_E = 2I_{Ea}, \quad I_{E^2} = I_{EE}. \tag{A-4}$$

In Cartesian coordinates, where $a_{ij} = \delta_{ij}$ and $\Delta = 1$, the complete system of two-dimensional invariants becomes

$$I_E = \delta_{mn} E_{mn}, \quad I_{E^2} = \tfrac{1}{2} e_{mp} e_{nq} E_{pq} E_{mn}, \quad I_{UV} = \tfrac{1}{2} e_{mp} e_{nq} U_{pq} V_{mn}, \tag{A-5}$$

where $\boldsymbol{U}$ and $\boldsymbol{V}$ are symmetric two-dimensional tensors.

Now we consider an anisotropic linear elastic body under plane-stress conditions and denote the covariant components of the strain and stress tensors by S_{ij} and σ_{ij}, respectively. In this case, the strain energy density Π_V and the virtual work of stresses δW for any constitutive law of the material is written in Cartesian coordinates as

$$\Pi_V = \tfrac{1}{2} \sigma_{ij} S_{ij}, \quad \delta W = \sigma_{ij} \delta S_{ij}. \tag{A-6}$$

Using (A-4), one can easily show that (A-6) is equivalent to

$$\Pi_V = \tfrac{1}{2} (I_\sigma I_S - 2 I_{\sigma S}), \quad \delta W = I_\sigma I_{(\delta S)} - 2 I_{\sigma(\delta S)}. \tag{A-7}$$

As can be seen, relations (A-7) are invariants and retain their form in any coordinates. In curvilinear coordinates, the invariants in (A-7) can be determined by (A-1) and (A-3).

It is worth noting that in the theory of shells, the bending strain tensor $\boldsymbol{\kappa}$ and transverse shear strain tensor $\boldsymbol{\Gamma}$ are introduced. As a result, one obtains combined invariants like $I_{S\kappa}$, $I_{S\Gamma}$, $I_{\kappa\Gamma}$, and so on, which can be determined by the template relation (A-3). Invariants of two-dimensional tensors for triangular shell finite elements are discussed in [Kuznetsov and Levyakov 2009].

References

[Antman 1995] S. S. Antman, *Nonlinear problems of elasticity*, Applied Mathematical Sciences **107**, Springer, New York, 1995.

[Argyris et al. 1979] J. Argyris, H. Balmer, J. Doltsinis, P. Dunne, M. Haase, M. Kleiber, G. Malejannakis, H.-P. Mlejnek, M. Muller, and D. Scharpf, "Finite element method — the natural approach", *Comput. Methods Appl. Mech. Eng.* **17/18** (1979), 1–106.

[Kuznetsov and Levyakov 2009] V. V. Kuznetsov and S. V. Levyakov, "Phenomenological invariants and their application to geometrically nonlinear formulation of triangular finite elements of shear deformable shells", *Internat. J. Solids Structures* **46**:5 (2009), 1019–1032.

[Sneddon and Berry 1958] I. N. Sneddon and D. S. Berry, "The classical theory of elasticity", pp. 1–126 in *Elastizität und Plastizität*, Handbuch der Physik, herausgegeben von S. Flügge. Bd. 6, Springer, Berlin, 1958.

[Timoshenko and Goodier 1970] S. Timoshenko and J. N. Goodier, *Theory of elasticity*, McGraw-Hill, New York, 1970. 3rd ed.

Received 20 Jan 2012. Accepted 7 May 2012.

VIKTOR V. KUZNETSOV: vku1952@yandex.ru
Department of Engineering Mathematics, Novosibirsk State Technical University, Novosibirsk, 630092, Russia

STANISLAV V. LEVYAKOV: stan-levyakov@yandex.ru
Dapartment of Engineering Mathematics, Novosibirsk State Technical University, Novosibirsk, 630092, Russia

JOURNAL OF MECHANICS OF MATERIALS AND STRUCTURES
Vol. 7, No. 5, 2012
dx.doi.org/10.2140/jomms.2012.7.469

TWO CASES OF RAPID CONTACT ON AN ELASTIC HALF-SPACE: SLIDING ELLIPSOIDAL DIE, ROLLING SPHERE

LOUIS MILTON BROCK

In one case a rigid ellipsoidal die translates over the surface of a half-space. Because of friction, both compression and shear force are required. In the other, a rigid sphere rolls on the surface under a compressive force. Both motions occur along a straight path at constant subcritical speed. A dynamic steady state is treated, that is, the contact zone and its traction remain constant in the frame of the die or sphere. Exact solutions for contact zone traction are derived in analytic form, as well as formulas for the contact zone shape. Axial symmetry is not required in the solution process. Cartesian coordinates are used, but a system of quasipolar coordinates is introduced that allows problem reduction to singular integral equations similar in form to those found in 2D contact.

1. Introduction

Sliding and rolling contact arises in machining, mechanism operation, and vehicle travel [Barwell 1979; Bayer 1994; Blau 1996]. The literature on the mechanics of contact is vast, for example, [Ahmadi et al. 1983; Barber 1983; Johnson 1985; Kalker 1990; Hills et al. 1993]. An important category — e.g., [Craggs and Roberts 1967; Churilov 1978; Rahman 1996] — treats indentation of an elastic surface by a rigid die that also translates over the surface. If speed and resultant forces are constant, then a dynamic steady state may be achieved. In that instance, contact zone geometry and surface traction do not vary in the frame of the moving die. For the thermoelastic solid, Brock and Georgiadis [2000] treat sliding contact opposed by friction and Brock [2004] treats rolling contact without slip by a rigid cylinder. Sliding and rolling speeds are constant, and robust asymptotic solutions in analytic form are given for the dynamic steady state in 2D.

The aforementioned studies are adopted here for 3D isothermal problems of sliding by a rigid ellipsoid and rolling by a rigid sphere. Again sliding is resisted by friction, and rolling without slipping is assumed. Sliding and rolling speeds are constant and subcritical, that is, below the Rayleigh wave speed. Ignoring slipping in rolling is an idealization [Johnson 1985], and one that gives rise to rapid oscillations in thin strips along the contact zone edge. It is noted, however, that strip widths in [Brock 2004] prove to be orders of magnitude smaller than the contact zone radius.

The solution process is standard, e.g., [Hills et al. 1993]: a solution to the unmixed boundary value problem of specified surface traction reduces the mixed contact problem to the solution of integral equations. To this end, the governing equations for the elastic half-space, subjected to a translating zone of (somewhat) arbitrary traction over its surface, are given in the next section. Translation speed is constant and subcritical, and zone geometry and traction do not change during translation. Therefore, as in [Brock and Georgiadis 2000; Brock 2004], a dynamic steady state is assumed. Cartesian coordinates are used,

Keywords: sliding contact, ellipsoid, rolling contact sphere, quasipolar.

and an exact transform solution in the half-space surface spatial variables is obtained. In view of the 3D nature of the problem and the lack of axial symmetry for the ellipsoidal die, quasipolar coordinates, both in transform and spatial planes, are employed during the inversion process. These are defined by a polar angle that sweeps through 180° (π radians) and a radial coordinate that has both positive and negative directions. For points in the contact zone, the resulting displacement expressions reduce to double integrals whose limits are independent of the points. The imposed displacement conditions are then satisfied by requiring the integrands to be solutions of Cauchy singular integral equations that are similar in form to those in the 2D studies [Brock and Georgiadis 2000; Brock 2004]. The contact zone traction is then extracted as analytic functions of the quasipolar coordinates. The normal traction is required to vanish continuously on the contact zone boundary, and to render the resultant compression force as a stationary value for a given sliding/rolling speed. These requirements lead to expressions that define the contact zone geometry.

2. General equations

In terms of Cartesian coordinates $\mathbf{x}(x_k)$, an undisturbed, linear isotropic, homogeneous half-space occupies region $x_3 > 0$. A traction distribution is then applied to a finite, simply connected area C of the surface $x_3 = 0$. Boundary contour $\Im(x_1, x_2) = 0$ defines a continuous closed curve, with continuously varying tangent and normal directions and radius of curvature. The lattermost is always directed to the interior of C and the x_1-direction is an axis of symmetry. Area C is then translated in the positive x_1-direction at constant subcritical speed v. It does not change, and the traction distribution remains invariant with respect to it. A dynamic steady state ensues for which half-space response is invariant in the frame of translating C. It is therefore convenient to translate the Cartesian system with C, so that displacement $\mathbf{u}(u_k)$ and traction $\mathbf{T}(\sigma_{ik})$ vary only with $\mathbf{x}(x_k)$, where time differentiation becomes $-v\partial_1$ and ∂_k signifies x_k-differentiation. For $x_3 > 0$ the governing equations can be extracted from [Achenbach 1973] and modified for the dynamic steady state as

$$\mathbf{u} = \mathbf{u}_D + \mathbf{u}_S, \tag{1}$$

$$(\nabla^2 - c^2\partial_1^2)\mathbf{u}_S = 0, \qquad \nabla \cdot \mathbf{u}_S = 0, \tag{2}$$

$$(c_D^2\nabla^2 - c^2\partial_1^2)\mathbf{u}_D = 0, \qquad \nabla \times \mathbf{u}_D = 0, \tag{3}$$

$$\frac{1}{\mu}\mathbf{T} = (c_D^2 - 2)(\nabla \cdot \mathbf{u}_D)\mathbf{1} + 2(\nabla\mathbf{u} + \mathbf{u}\nabla). \tag{4}$$

Here $(\nabla, \mathbf{1}, \nabla^2)$ are the gradient, identity tensor, and Laplacian. Quantities (c, c_D) are, respectively, the contact area speed and dilatational wave speed (v, v_D) that are made dimensionless with respect to the isothermal shear (rotational) wave speed v_S, where

$$c_D = \sqrt{m+1}, \quad m = \frac{1}{1-2\nu}, \quad v_S = \sqrt{\frac{\mu}{\rho}}. \tag{5}$$

Here (ν, μ, ρ) are the Poisson's ratio, shear modulus, and mass density. The boundary conditions for $x_3 = 0$ are that surface traction vanishes for $(x_1, x_2) \notin C$, but

$$\sigma_{13} = \tau_1, \quad \sigma_{23} = \tau_2, \quad \sigma_{33} = \sigma, \quad (x_1, x_2) \in C. \tag{6}$$

Here (τ_1, τ_2, σ) are bounded and continuous functions of $(x_1, x_2) \in C$ but can be integrably singular on the contour $\Im(x_1, x_2) = 0$. In addition $(\mathbf{u}, \mathbf{T})$ should remain finite for $|\mathbf{x}| \to \infty$, $x_3 > 0$.

3. General transform solution

After [van der Pol and Bremmer 1950; Sneddon 1972] the double bilateral Laplace transform is defined as

$$\hat{F} = \iint F(x_1, x_2) \exp(-p_1 x_1 - p_2 x_2)\, dx_1 dx_2. \tag{7}$$

Integration is along the entire $\mathrm{Re}(x_1)$ and $\mathrm{Re}(x_2)$-axes. Application of (7) to (1)–(6) gives for $x_3 > 0$

$$\hat{\mathbf{u}}_D = (p_1, p_2, -\lambda_\pm) D \exp(-\lambda_\pm x_3), \tag{8a}$$

$$\hat{\mathbf{u}}_S = (S_1, S_2, S_3) \exp(-\lambda_S x_3), \quad \lambda_S S_3 = p_1 S_1 + p_2 S_2. \tag{8b}$$

Here coefficients (S_1, S_2, D) are given by

$$\mu Q_R S_1 = \frac{p_2}{\lambda_S} Q_N (p_2 \hat{\tau}_1 - p_1 \hat{\tau}_2) - \lambda_S (Q_K \hat{\tau}_1 + 2 p_1 \lambda_D \hat{\sigma}), \tag{9a}$$

$$\mu Q_R S_2 = \frac{p_1}{\lambda_S} Q_N (p_1 \hat{\tau}_2 - p_2 \hat{\tau}_1) - \lambda_S (Q_K \hat{\tau}_2 + 2 p_2 \lambda_D \hat{\sigma}), \tag{9b}$$

$$\mu Q_R D = Q_K \hat{\sigma} - 2\lambda_S (p_1 \hat{\tau}_1 + p_2 \hat{\tau}_2). \tag{9c}$$

In (8) and (9) quantities

$$Q_N = Q_K - 2\lambda_D \lambda_S, \quad Q_R = 4(p_1^2 + p_2^2)\lambda_D \lambda_S + Q_K^2, \quad Q_K = (c^2 - 2)p_1^2 - 2p_2^2, \tag{10a}$$

$$\lambda_S = \sqrt{(c^2 - 1)p_1^2 - p_2^2}, \quad \lambda_D = \sqrt{(s_D^2 c^2 - 1)p_1^2 - p_2^2}, \quad s_D = \frac{1}{c_D}. \tag{10b}$$

Equation (8) is bounded for $x_3 > 0$ only when $\mathrm{Re}(\lambda_S, \lambda_D) \geqslant 0$, so that branch cuts in the (p_1, p_2)-plane is required.

4. Inversion scheme

In view of (8)–(10) and [van der Pol and Bremmer 1950; Sneddon 1972], transform inversion for, say the contribution of σ to u_3, involves the operation

$$-\frac{1}{2\pi i} \int dp_1 \frac{1}{2\pi i} \int dp_2 \frac{\lambda_D}{\mu \Delta} U \iint d\xi_1\, d\xi_2\, \sigma \exp[p_1(x_1 - \xi_1) + p_2(x_2 - \xi_2)]. \tag{11}$$

In (11), $\sigma = \sigma(\xi_1, \xi_2)$ and $U = U(p_1, p_2)$, where

$$U(p_1, p_2) = 2(p_1^2 + p_2^2) \exp(-\lambda_S x_3) + Q_K \exp(-\lambda_D x_3). \tag{12}$$

Double integration is over C, and single integration is along the entire $\mathrm{Im}(p_1)$- and $\mathrm{Im}(p_2)$-axes. This

suggests definitions and transformations

$$p_1 = p\cos\psi, \qquad p_2 = p\sin\psi, \tag{13a}$$

$$x = x_1\cos\psi + x_2\sin\psi, \qquad y = x_2\cos\psi - x_1\sin\psi, \tag{13b}$$

$$\xi = \xi_1\cos\psi + \xi_2\sin\psi, \qquad \eta = \xi_2\cos\psi - \xi_1\sin\psi. \tag{13c}$$

In (13), $\mathrm{Re}(p) = 0+$, $-\infty < [\mathrm{Im}(p), x, y, \xi, \eta, \xi_1, \xi_2] < \infty$ and $|\psi| < \pi/2$. Parameters (p, ψ), $(x, \psi; y = 0)$, and $(\xi, \psi; \eta = 0)$ constitute quasipolar coordinate systems, that is,

$$dx_1\,dx_2 = |x|\,dx\,d\psi, \quad d\xi_1\,d\xi_2 = |\xi|\,d\xi d\psi, \quad dp_1\,dp_2 = |p|\,dp\,d\psi. \tag{14}$$

Thus (11) can be written as

$$\frac{1}{i\pi}\int_\Psi d\psi\frac{1}{2\pi i}\int|p|\,dp\frac{\omega_D}{\mu R}\frac{\sqrt{-p}}{p\sqrt{p}}U(p,\psi)\int_{\mathrm{N}}d\eta\int_\Xi d\xi\,\sigma(\xi,\eta)\exp p(x-\xi), \tag{15a}$$

$$U(p,\psi) = 2\exp(-\omega_S x_3\sqrt{-p}\sqrt{p}) + K\exp(-\omega_D x_3\sqrt{-p}\sqrt{p}). \tag{15b}$$

Integration with respect to p is along the positive side of the entire imaginary axis. Subscripts (Ψ, N, Ξ) signify integration over, respectively, the ranges $-\pi/2 < \psi < \pi/2$, $\eta_-(\psi) < \eta < \eta_+(\psi)$, and $x_-(\eta, \psi) < \xi < x_+(\eta, \psi)$. Limits $\eta_\pm(\psi)$ are points on the contour $\Im[\xi_1(\xi, \eta), \xi_2(\xi, \eta)] = 0$ where $d\eta/d\xi = 0$, and limits $x_\pm(\eta, \psi)$ locate the ends of a line parallel to the ξ-axis that spans C for a given η. The restrictions on $(C, \Im)$ imply that $(x_\pm, \eta_\pm)$ exist and are continuous in ψ. In (15) we also have

$$\omega_S = \sqrt{1 - c^2\cos^2\psi}, \quad \omega_D = \sqrt{1 - s_D^2 c^2\cos^2\psi}, \tag{16a}$$

$$N = K + 2\omega_S\omega_D, \quad R = 4\omega_S\omega_D - K^2, \quad K = c^2\cos^2\psi - 2. \tag{16b}$$

The exponential terms in (15b) are made bounded for $x_3 > 0$ by requiring that $\mathrm{Re}(\sqrt{\pm p}) \geqslant 0$ in the p-plane with, respectively, branch cuts $\mathrm{Im}(p) = 0, \mathrm{Re}(p) < 0$ and $\mathrm{Im}(p) = 0, \mathrm{Re}(p) > 0$. The p-integration is (15a) and can be obtained from Appendix A. The result is that (15a) and counterparts for (τ_1, τ_2) give u_3 for $x_3 > 0$:

$$u_3 = -\frac{1}{\pi^2}\int_\Psi d\psi\frac{\omega_D}{\mu R}\int_{\mathrm{N}}d\eta\int_\Xi d\xi\,\sigma(\xi,\eta)\frac{K(x-\xi)}{(x-\xi)^2+\omega_D^2x_3^2} + \frac{2\omega_S(x-\xi)}{(x-\xi)^2+\omega_S^2x_3^2} \tag{17}$$

$$-\frac{1}{\pi^2}\int_\Psi d\psi\frac{\omega_S}{\mu R}\int_{\mathrm{N}}d\eta\int_\Xi d\xi\,[\tau_1(\xi,\eta)\cos\psi + \tau_2(\xi,\eta)\sin\psi]\frac{2\omega_D^2x_3}{(x-\xi)^2+\omega_D^2x_3^2} + \frac{Kx_3}{(x-\xi)^2+\omega_S^2x_3^2}.$$

Here $x = x_1\cos\psi + x_2\sin\psi$, and for $x_3 = 0$, $(x_1, x_2) \in C$, (17) gives (see Appendix A):

$$u_3 = \frac{1}{\pi}\int_\Psi\frac{d\psi}{\mu R}\int_{\mathrm{N}}d\eta\left[c^2\omega_D\cos^2\psi\frac{(vp)}{\pi}\int_\Xi\sigma(\xi,\eta)\frac{d\xi}{\xi-x} - N\mathrm{T}(x,\eta)\right], \tag{18a}$$

$$\mathrm{T}(x,\eta) = \tau_1(x,\eta)\cos\psi + \tau_2(x,\eta)\sin\psi. \tag{18b}$$

Here (vp) signifies principal value integration. Similar results can be obtained for (u_1, u_2). When $\psi = 0$, the term R in (16b) is the 2D Rayleigh function. It can be shown that $R \geqslant 0$ $(0 \leqslant c^2 < c_R^2)$ and $R \leqslant 0$ $(c_R^2 < c^2 < 1)$, where root c_R^2 defines the Rayleigh wave speed $v = c_R v_S$. Vanishing R can be associated with critical behavior [Georgiadis and Barber 1993]. Here of course $R = 0$ when $v = v_R$ only for $\psi = 0$.

5. Sliding contact with friction

Consider that (σ, τ_1, τ_2) result from the sliding of a rigid die at subcritical speed v in the positive x_1-direction. The die is an ellipsoid that, when it touches but does not indent the surface $x_3 = 0$, can be described in the translating **x**-coordinate by

$$C_1 x_1^2 + C_2 x_2^2 + C_3\left(x_3 + \frac{1}{\sqrt{C_3}}\right)^2 = 1. \tag{19}$$

Here (C_1, C_2, C_3) are positive constants, their inverses have dimensions of length squared, and (19) is consistent with the symmetry assumed for C, which of course is now a contact zone. If a rigid body motion U_3 into the surface accompanies translation, indentation occurs. This requires compressive force F_3 in the x_3-direction. For small deformations indentation is defined by $u_3 = u_3^C$, $(x_1, x_2) \in C$, where

$$u_3^C = U_3 - \frac{1}{2\sqrt{C_3}}(C_1 x_1^2 + C_2 x_2^2). \tag{20}$$

It is noted that $|\mathbf{x}|$ is now the distance from the surface point in the contact zone that undergoes the largest normal displacement. That is, the validity of the asymptotic expressions increases with this distance. If sliding is resisted by friction with kinetic coefficient γ, die translation also requires a shear force $F_1 = \gamma F_3$ in the positive x_1-direction. It is assumed that die translation and die/surface slip essentially coincide, that is, $(\tau_2 \approx 0, \tau_1 = \gamma\sigma)$. In view of (18) the contact problem must then satisfy for $(x_1, x_2) \in C$ the equation

$$\frac{1}{\pi}\int_\Psi d\eta \int_\mathrm{N} d\eta \left[\frac{c^2\omega_D \cos^2\psi}{\pi\mu R}(vp)\int_\Xi \sigma(\xi,\eta)\frac{d\xi}{\xi - x} - \frac{N}{\mu R}\Gamma\sigma(x,\eta)\right] = u_3^C, \quad \Gamma = \gamma\cos\psi. \tag{21}$$

In light of (7), (20), and Appendix A, u_3^C can be written as

$$u_3^C = -\frac{1}{\pi}\int_\Psi d\eta \int_\mathrm{N} d\eta \int_\Xi d\xi \frac{d}{dx}\delta(x-\xi)u_3^C(\xi,\eta), \tag{22a}$$

$$u_3^C(\xi,\eta) = U_3 - \frac{C_1}{2\sqrt{C_3}}(\xi\cos\psi - \eta\sin\psi)^2 - \frac{C_2}{2\sqrt{C_3}}(\eta\cos\psi + \xi\sin\psi)^2. \tag{22b}$$

Here δ is the Dirac function. Equation (21) thereby reduces to matching the integrands of double integration in (ψ, η). Parameter ξ in $\sigma(\xi, \eta)$ is an integration variable representing parameter x that itself depends on coordinate (x_1, x_2) and integration variable ψ. However, as noted in light of (13) for $y = 0$, (x_1, x_2) can be replaced by quasipolar coordinates (x, ψ). Thus traction σ itself can be found by dropping η, and (21) and (22) are reduced to

$$-c^2\omega_D\cos^2\psi\frac{(vp)}{\pi}\int_\Xi \sigma(\xi,\psi)\frac{d\xi}{\xi - x} + \Gamma N\sigma(x,\psi) = \mu R G(x,\psi), \tag{23a}$$

$$G(x,\psi) = \frac{-Ax}{\sqrt{C_3}}, \quad A = C_1\cos^2\psi + C_2\sin^2\psi. \tag{23b}$$

In view of Appendix B we introduce unknowns $g(x)$ and Ω in the representation

$$\frac{1}{\mu}\sigma(x) = g(x)\cos\pi\Omega + \mathrm{I}(g; x)\sin\pi\Omega \quad (x_- < x < x_+). \tag{24}$$

Experience [Brock and Georgiadis 2000; Brock 2004] with 2D analysis indicates that $\Omega \neq \Omega(x)$. Dependence of $(\sigma, g, \Omega, x_\pm)$ on ψ is implicit in (25). Use of (25), (B3a), (B3b), and (B4) in (24) gives a classical [Erdogan 1985] linear relation in (g, I):

$$[\Gamma N \sin\pi\Omega - c^2\omega_D \cos^2\psi \cos\pi\Omega]\mathrm{I}(g; x) + [\Gamma N \cos\pi\Omega + c^2\omega_D \cos^2\psi \sin\pi\Omega]g(x) = RG(x, \psi). \quad (25)$$

Eigenvalue Ω is chosen to make the coefficient of $\mathrm{I}(g; x)$ vanish, and $g(x)$ follows:

$$\Omega = -\frac{1}{2} + \frac{1}{\pi}\tan^{-1}\left(\frac{-\gamma N}{c^2\omega_D \cos\psi}\right), \quad g(x) = \frac{R}{\Delta}\frac{Ax}{\sqrt{C_3}}, \quad (26a)$$

$$\Delta = \sqrt{\Gamma_\Psi^2 N^2 + (c^2\omega_D \cos^2\psi)^2} = \cos\psi\sqrt{\gamma^2 N^2 + (c^2\omega_D \cos\psi)^2}, \quad (26b)$$

$$\sin\pi\Omega = -\frac{c^2\omega_D}{\Delta}\cos^2\psi, \quad \cos\pi\Omega = -\frac{\gamma N}{\Delta}\cos^2\psi. \quad (26c)$$

In (26a), $-\frac{1}{2} < \Omega < 0$ for $0 < v < v_S$. The polynomial form of $g(x)$ allows the use of (B6) (second equation) to evaluate (24):

$$\sigma(x, \psi) = \frac{\mu R}{\Delta}\frac{A}{\sqrt{C_3}}\left(\frac{x_+ - x}{x - x_-}\right)^\Omega (x + \Omega L), \quad L = x_+ - x_-(x_- < x < x_+). \quad (27)$$

Dependence on ψ is now more explicit. The negative Ω gives σ an integrable singularity as $x \to x_+$. Signorini conditions for contact [Georgiadis and Barber 1993] prohibit singular gradients at the contact zone boundary. Therefore (27) leads to

$$\sigma(x, \psi) = -\frac{\mu A}{\sqrt{C_3}}\frac{R}{\Delta}(x_+ - x)^{1+\Omega}(x - x_-)^{-\Omega}, \quad (28a)$$

$$x_+ = -\Omega L, \quad x_- = -(1 + \Omega)L. \quad (28b)$$

For $0 \leqslant v < v_R$, $R \geqslant 0$ for $|\psi| \leqslant \pi/2$, and (28a) satisfies the Signorini condition that nonwelded contact cannot not involve tensile stress. It is also noted that the (R, Δ)-ratio in (28a) is finite for $|\psi| \leqslant \pi/2$.

6. Contour of C

Equation (28b) defines in part contour $\Im$ and, because $\Omega(-\psi) = \Omega(\psi)$ and $\Omega(\pm\pi/2) = -\frac{1}{2}$, does not violate the symmetry of C. The unknown contact zone span L depends on c and is an even function of ψ. It is determined by requiring that (τ_1, τ_2, σ) be consistent with the resultant force system acting on the die. Here $(x_\pm, \sigma)$ and therefore τ_1 are even functions of ψ, and $\tau_2 \approx 0$. Thus the condition that there is no resultant force in the x_2-direction and no resultant torque about the x_3-axis is automatically satisfied. The condition that resultant force in the (x_1, x_3)-directions is $F_1 = \gamma F_3$ and $-F_3$, respectively, is met if

$$\int_\Psi d\psi \int_\Xi \sigma(\xi, \psi)|\xi|\, d\xi = -F_3. \quad (29)$$

Equation (29) is an integral equation for $L(c, \psi)$. One solution approach is based on the observation that, for a given value $x_3 > 0$, projection of die (19) onto the x_1x_2-plane is an elliptical area bounded by

contour $C_1x_1^2 + C_2x_2^2 =$ constant. In terms of (x, ψ), if the span of C along the x_1-axis ($\psi = 0$) is L_1, then the span L for a given $|\psi| < \pi/2$ is

$$L = \sqrt{\frac{C_1}{A_1}} L_1. \tag{30}$$

A simple assumption is that (30) also holds in (28b) for $(C, \Im)$, where L_1 is an unknown function of c. Here, however, it is argued that, for a given speed (c), F_3 should be stationary with respect to (28a). That is,

$$\int_\Psi d\psi \int_\Xi \delta\sigma(\xi, \psi)|\xi|\, d\xi = 0. \tag{31}$$

This requirement is satisfied when at every $x_- < x < x_+$, $|\psi| < \pi/2$,

$$\delta\sigma = \frac{\partial\sigma}{\partial x}\delta x + \frac{\partial\sigma}{\partial\psi}\delta\psi = 0. \tag{32}$$

Here ψ and x are held constant in the first and second coefficients, respectively, and $(\delta x, \delta\psi)$ are arbitrary. Differentiation of (28a) shows that

$$x = -(1+2\Omega)L: \quad \frac{\partial\sigma}{\partial x} = 0, \quad \frac{\partial^2\sigma}{\partial x^2} > 0. \tag{33a}$$

The second term then vanishes for $x = -(1+2\Omega)L$ if

$$-\frac{\partial}{\partial\psi}\left(\frac{RA}{\Delta\sqrt{C_3}} QL\right) = 0, \quad Q = (1+\Omega)^{1+\Omega}(-\Omega)^{-\Omega}. \tag{33b}$$

Separation of variables and integration leads to

$$L = \frac{C_1}{A}\frac{R_1\Delta}{R\Delta_1}\frac{Q_1}{Q}L_1, \qquad Q_1 = (1+\Omega_1)^{1+\Omega_1}(-\Omega_1)^{-\Omega_1}, \tag{34a}$$

$$R_1 = 4\omega_{1D}\omega_{1S} - K_1^2, \qquad \Delta_1 = \sqrt{\gamma^2 N_1^2 + (c^2\omega_{1D})^2}, \tag{34b}$$

$$N_1 = 2\omega_{1D}\omega_{1S} + K_1, \qquad \Omega_1 = -\frac{1}{2} + \frac{1}{\pi}\tan^{-1}\left(\frac{-\gamma N_1}{c^2\omega_{1D}}\right), \tag{34c}$$

$$\omega_{1S} = \sqrt{1-c^2}, \qquad \omega_{1D} = \sqrt{1-\frac{c^2}{c_D^2}}, \quad K_1 = c^2 - 2. \tag{34d}$$

For $L = L_2$, that is, $|\psi| = \pi/2$, (34a) and its static ($c = 0$) and smooth sliding ($c \neq 0$, $\gamma = 0$) limit cases give, respectively,

$$L_2 = \frac{C_1}{C_2}\frac{\sqrt{c_D^4 + \gamma^2}}{c_D^2 - 1}\frac{R_1 Q_1}{\Delta_1}L_1, \quad L_2 = \frac{C_1}{C_2}L_1, \quad L_2 = \frac{C_1}{C_2}\frac{c_D^2}{2(c_D^2-1)}\frac{R_1}{c^2\omega_{1D}}L_1. \tag{35}$$

Equations (30), (34a) and (35) in light of (28b) allow several observations:

(I) Except for a circular projection profile and smooth contact ($C_1 = C_2$, $\gamma = 0$), the ratio of spans along the axes of symmetry is not maintained in C.

γ	$c=0.1$	$c=0.2$	$c=0.3$	$c=0.4$	$c=0.5$	$c=0.6$
0.1	0.9938	0.9712	0.9330	0.8781	0.8034	0.7049
0.2	0.9948	0.9721	0.9339	0.8789	0.8042	0.7055
0.3	0.9963	0.9736	0.9354	0.8803	0.8045	0.7066

Table 1. Values of the dimensionless ratio C_2L_2/C_1L_1 for pairs of (γ, c).

(II) In the static case with an elliptic projection profile, the difference between spans is enhanced in C.

(III) Die translation speed ($c \neq 0$) accentuates this effect.

(IV) Friction leaves C with symmetry only with respect to the x_1-axis, whether die translation occurs ($c \neq 0$) or not ($c = 0$).

Results in [Rahman 1996] also exhibit a sliding speed effect on span ratio. Moreover, stationary principles are features of static smooth contact [Barber 1992]. The effect noted in (III) is illustrated in Table 1 with values of ratio C_2L_2/C_1L_1 for values of (γ, c).

Substituting (28) and (34a) in (29), and applying integration results from Appendix B along with an integration variable change, gives, finally, an equation for L_1 as a function of c:

$$F_3 = \left(\frac{R_1Q_1}{\Delta_1}\right)^3 (C_1L_1)^3 \frac{\mu}{\sqrt{C_3}} \int_\Psi \frac{d\psi}{Q^3} \left(\frac{\Delta}{AR}\right)^2 \int_{-(1+\Omega)}^{-\Omega} (-\Omega - t)^{1+\Omega} (t + 1 + \Omega)^{-\Omega} |t|\, dt. \tag{36}$$

In view of (28b) and the monotonic variation of Ω with ψ and its range $\left(-\frac{1}{2} < \Omega < 0\right)$, span L does not cross $\Im$.

7. Rolling without slipping

Consider that rolling without slipping by a rigid sphere of radius r_0 is what produces the translating C. Rolling at constant speed requires no force in the x_1-direction, but indentation needs a compressive force, which we call F_3, to be imposed. Thus (19) and (20) are replaced by

$$x_1^2 + x_2^2 + (x_3 + r_0)^2 = r_0^2, \quad u_3^C = U_3 - \frac{1}{2r_0}(x_1^2 + x_2^2). \tag{37}$$

In view of (18) and its counterparts for (u_1, u_2), the contact problem in this case gives coupled equations:

$$-c^2\omega_D \cos^2\psi \frac{(vp)}{\pi} \int_\Xi d\xi \frac{\sigma(\xi, \psi)}{\xi - x} + N\mathrm{T}(x, \psi) = \mu R G_3(x, \psi), \tag{38a}$$

$$-N\sigma(x, \psi)\cos\psi + \frac{(vp)}{\pi\omega_S} \int_\Xi \frac{d\xi}{\xi - x} [N_1\tau_1(\xi, \psi) + N_{12}\tau_2(\xi, \psi)] = \mu R G_1(x, \psi), \tag{38b}$$

$$-N\sigma(x, \psi)\sin\psi + \frac{(vp)}{\pi\omega_S} \int_\Xi \frac{d\xi}{\xi - x} [N_{12}\tau_1(\xi, \psi) + N_2\tau_2(\xi, \psi)] = \mu R G_2(x, \psi). \tag{38c}$$

Coefficients (N_1, N_2, N_{12}) are

$$(N_1, N_2) = M(\cos^2\psi, \sin^2\psi) - M, \quad N_{12} = M\sin\psi\cos\psi, \tag{39a}$$

$$M = K + 4\omega_S\omega_D - 2\omega_S^2 = 2N + c^2\cos^2\psi, \quad G_k(x,\psi) = \frac{\partial}{\partial x}u_k^C(x,0). \tag{39b}$$

Linear analysis [Johnson 1985] of contact surface kinematics and experience with the 2D rolling cylinder [Brock 2004] suggests in view of (37) that (u_1^C, u_2^C) are such that

$$[G_1(x,\psi), G_2(x,\psi)] = G(x,\psi)(\cos\psi, \sin\psi), \quad G_3(x,\psi) = -\frac{x}{r_0}, \quad G(x,\psi) = -V_0 + \frac{x^2}{2r_0^2}. \tag{40}$$

In light of Appendix B, we write

$$\frac{1}{\mu}(\sigma, \tau_k) = (g, g_k)\cos\pi\Omega + [\mathrm{I}(g;x), \mathrm{I}(g_k;x)]\sin\pi\Omega. \tag{41}$$

Here $k = (1, 2)$ and, as in (26), dependence of $(\sigma, \tau_1, \tau_2, \Omega)$ and (g, g_1, g_2) on ψ is implicit. Use of Appendix B then gives the set of equations

$$\mathbf{K}\begin{bmatrix}\mathrm{I}(g;x)\\ \mathrm{I}(g_1;x)\\ \mathrm{I}(g_2;x)\end{bmatrix} + \mathbf{M}\begin{bmatrix}g(x)\\ g_1(x)\\ g_2(x)\end{bmatrix} = R\begin{bmatrix}G_3\\ G\cos\psi\\ G\sin\psi\end{bmatrix}, \tag{42a}$$

$$\mathbf{K} = \begin{bmatrix} -c^2\omega_D\cos^2\psi\cos\pi\Omega & N\cos\psi\sin\pi\Omega & N\sin\psi\sin\pi\Omega \\ -N\cos\psi\sin\pi\Omega & \dfrac{N_1}{\omega_S}\cos\pi\Omega & \dfrac{N_{12}}{\omega_S}\cos\pi\Omega \\ -N\sin\psi\sin\pi\Omega & \dfrac{N_{12}}{\omega_S}\cos\pi\Omega & \dfrac{N_2}{\omega_S}\cos\pi\Omega \end{bmatrix}, \tag{42b}$$

$$\mathbf{M} = \begin{bmatrix} c^2\omega_D\cos^2\psi\sin\pi\Omega & N\cos\psi\cos\pi\Omega & N\sin\psi\cos\pi\Omega \\ -N\cos\psi\cos\pi\Omega & -\dfrac{N_1}{\omega_S}\sin\pi\Omega & -\dfrac{N_{12}}{\omega_S}\sin\pi\Omega \\ -N\sin\psi\cos\pi\Omega & -\dfrac{N_{12}}{\omega_S}\sin\pi\Omega & -\dfrac{N_2}{\omega_S}\sin\pi\Omega \end{bmatrix}. \tag{42c}$$

In (42b) $|\mathbf{K}|$ vanishes for eigenvalues $\Omega = (\Omega_\pm, \Omega_0)$ given by

$$\Omega_\pm = \Omega_0 \mp i\mathrm{P}, \quad \Omega_0 = -\tfrac{1}{2}, \tag{43a}$$

$$\mathrm{P} = \frac{1}{\pi}\ln\sqrt{\frac{1+q}{1-q}}, \quad q = \frac{-N}{\sqrt{\omega_S\omega_D}c^2\cos^2\psi}. \tag{43b}$$

Quantity $q > 0$ for $|\psi| \leqslant \pi/2$ when $0 < v < v_R$, and $(\Omega_0, \Omega_\pm)$ is associated with eigenfunction sets $(g_0, g_\pm)$ and $(g_k^0, g_k^\pm)$, $k = (1, 2)$. Given that $|\mathbf{K}| = 0$, the first term in (42a) disappears by choosing

$$g_1^\pm(x) = \mathrm{H}_\pm(x)\cos\psi, \quad g_2^\pm(x) = \mathrm{H}_\pm(x)\sin\psi, \tag{44a}$$

$$N\sin\pi\Omega_\pm\mathrm{H}_\pm(x) = c^2\omega_F\cos^2\psi\cos\pi\Omega_\pm g_\pm(x), \tag{44b}$$

$$g_1^0(x) = g_0(x)\sin\psi, \quad g_2^0(x) = -g_0(x)\cos\psi. \tag{44c}$$

Substitution into the remaining term in (42a) gives three equations for $(g_0, g_\pm)$. From (43) it follows that

$$\sin\pi\Omega_\pm = -\cosh\pi\mathrm{P} = -\frac{\sqrt{\omega_S\omega_D}c^2\cos^2\psi}{\sqrt{(1-\omega_S\omega_D)R}}, \quad \cos\pi\Omega_\pm = \mp i\sinh\pi\mathrm{P} = \frac{\pm iN}{\sqrt{(1-\omega_S\omega_D)R}}. \tag{45a}$$

Their use in the three equations then leads to the expressions

$$g_0(x) = 0, \quad g_\pm(x) = \frac{\sqrt{R}}{2\sqrt{1-\omega_S\omega_D}}\left[\sqrt{\frac{\omega_S}{\omega_D}}G_3(x,\psi) \pm iG(x,\psi)\right]. \tag{46}$$

Use of (41) and polynomial integration results from Appendix B lead to closed-form expressions for (σ, τ_1, τ_2). In light of (43a) these are singular as $x \to x_+$, and enforcement of the Signorini conditions leads to requirements

$$\left[\mathrm{P}\frac{L}{r_0} + \sqrt{\frac{\omega_S}{\omega_D}}\right]\left(x_+ - \frac{L}{2}\right) = 0, \quad L = x_+ - x_-, \tag{47a}$$

$$V_0 + \frac{L}{r_0}\sqrt{\frac{\omega_S}{\omega_D}} - \frac{1}{2r_0^2}\left[\left(x_+ - \frac{L}{2}\right)^2 + \frac{L^2}{8}(1-4\mathrm{P}^2)\right] = 0. \tag{47b}$$

Expressions for (V_0, x_+) follow as

$$V_0 = \frac{L}{r_0}\left[\frac{L}{16r_0}(1-4\mathrm{P}^2) - \mathrm{P}\sqrt{\frac{\omega_S}{\omega_D}}\right], \quad x_\pm = \pm\frac{L}{2}. \tag{48}$$

Use of (48) in the closed-form expressions for (σ, τ_1, τ_2) gives

$$\sigma(x,\psi) = \frac{-\mu\mathrm{B}Q}{2r_0\cos\Phi}\sqrt{L^2-4x^2}\cos\left[\mathrm{P}\ln\frac{L-2x}{L+2x} - \Phi\right], \tag{49a}$$

$$\begin{bmatrix}\tau_1(x,\psi)\\ \tau_2(x,\psi)\end{bmatrix} = \frac{-\mu\mathrm{B}Q}{2r_0\cos\Phi}\sqrt{\frac{\omega_D}{\omega_S}}\begin{bmatrix}\cos\psi\\ \sin\psi\end{bmatrix}\sqrt{L^2-4x^2}\sin\left[\mathrm{P}\ln\frac{L-2x}{L+2x} - \Phi\right], \tag{49b}$$

$$Q = \frac{\sqrt{R}}{\sqrt{1-\omega_S\omega_D}}, \quad \Phi = \tan^{-1}\frac{x\mathrm{P}}{2\mathrm{B}r_0}, \quad \mathrm{B} = \frac{\mathrm{P}L}{2r_0} + \sqrt{\frac{\omega_S}{\omega_D}}. \tag{49c}$$

Equation (49) is integrable in x but the rapid oscillatory behavior due to the logarithmic term implies that compression is guaranteed only in a region $|x| < r_C < L/2$ of C. Under the reasonable assumption that $(L, r_C) \ll r_0$ it can be shown that

$$r_C = \frac{L}{2}\frac{1-\exp(-\pi/2\mathrm{P})}{1+\exp(-\pi/2\mathrm{P})}. \tag{50}$$

For a steel solid ($\nu = 1/3$, $\mu = 75\,\mathrm{GPa}$) calculations of (43) for various combinations of $|\psi| < \pi/2$ and $0 < c < c_R$ give $\exp(-\pi/2\mathrm{P}) \approx O(10^{-9})$. As in [Brock 2004], therefore, the boundary strip is orders of magnitude smaller than the contact zone span L. In (49) (σ, τ_1) and τ_2 are, respectively, even and odd functions of ψ. It follows that shear traction on C produces neither resultant force in the (x_1, x_2)-direction nor resultant moment about the x_3-axis. Compressive force F_3 is the resultant of σ so that (29) again provides an integral equation for span L in (49). Application of the stationary principle in (33) for this

$c=0.1$	$c=0.2$	$c=0.3$	$c=0.4$	$c=0.5$	$c=0.6$
0.994	0.9733	0.9384	0.8882	0.8204	0.7318

Table 2. Values of the dimensionless ratio L_2/L_1 for values of c.

case gives for $|\psi| < \pi/2$

$$x = 0: \quad \frac{\partial \sigma}{\partial x} = 0, \quad \frac{\partial^2 \sigma}{\partial x^2} > 0. \tag{51}$$

It can then be shown that L is given by

$$L = \frac{\mathrm{B}_1 Q_1}{\mathrm{B} Q} L_1, \quad Q_1 = \frac{\sqrt{R_1}}{\sqrt{1-(\omega_S \omega_D)_1}}, \quad \mathrm{B}_1 = \sqrt{\frac{\omega_{1S}}{\omega_{1D}}} + \frac{\mathrm{P}_1 L_1}{2r_0}. \tag{52}$$

Equation (52) is transcendental in (L, L_1), but becomes a linear relation under the assumption that $(L, L_1) \ll r_0$:

$$L = \sqrt{\frac{\omega_D \omega_{1S}}{\omega_S \omega_{1D}}} \frac{Q_1}{Q} L_1, \tag{53a}$$

$$L_2 = L_1 \quad (c = 0), \qquad L_2 = \frac{1}{2} \sqrt{\frac{c_D^2 + 1}{c_D^2 - 1}} \sqrt{\frac{c_D \omega_{1S}}{\omega_{1D}}} Q_1 L_1 \quad (c \neq 0). \tag{53b}$$

In light of the same assumption (29) reduces to the relation for unknown span L_1 along the x_1-axis of C:

$$\frac{1}{\mu r_0^2} F_3 = 2 \left[Q_1 \sqrt{\frac{\omega_{1S}}{\omega_{1D}}} \frac{L_1}{2r_0} \right]^3 \int_\Psi \frac{\omega_D}{\omega_S Q^2} d\psi \int_0^1 t \, dt \sqrt{1-t^2} \cos \mathrm{P} \ln \frac{1-t}{1+t}. \tag{54}$$

Study of (53) shows that in this case, contact zone C does not preserve the circular profile of the projected die area except in the static limit ($c = 0$). Values of the span ratio L_2/L_1 are given in Table 2 for $c \neq 0$, and show that increasing speed tends to "squeeze" C onto the x_1-axis. Equation (53a) does not define an ellipse. However, an elliptical approximation for C can use (53b) to define the ratio of semimajor and semiminor dimensions.

8. Comment on supercritical/subseismic behavior

As noted above sliding contact solutions for speeds $v_R < v < v_S$ violate Signorini conditions [Georgiadis and Barber 1993]. In particular, in the sliding die problem here (28a) for normal stress in C still holds for this speed range, and is still both bounded and continuous on zone boundary $\Im$. However, $R = 0$ along spans defined by $|\psi| = \Psi_R$, and $R < 0$ for $|\psi| < \Psi_R$, where

$$\Psi_R = \tan^{-1} \sqrt{\frac{c^2}{c_R^2} - 1}. \tag{55}$$

That is, contact zone traction changes in a continuous fashion from compression in two fan-shaped regions $\Psi_R < |\psi| < \pi/2$ to tension in two fan-shaped regions $|\psi| < \Psi_R$. The situation for the rolling

sphere case is more complicated: For $|\psi| < \Psi_R$, $R < 0$ and eigenvalues are now

$$\Omega_0 = -\frac{1}{2}, \quad \Omega_\pm = \mp\frac{i}{\pi}\ln\sqrt{\frac{q+1}{q-1}}. \tag{56}$$

Equation (56) and behavior of R show that traction is continuous as $|\psi| \to \Psi_R$ but, because $\Omega_\pm$ have no real part, traction on $\Im$ in fan-shaped regions $|\psi| < \Psi_R$ is both oscillatory in nature and not continuous. These two results suggest that contact actually does not occur for $|\psi| < \Psi_R$. Such a consideration is beyond the scope of this paper. Careful study of die/sphere-contact zone separation for $|\psi| < \Psi_R$ is required. Moreover, $\Psi_R \to 21.25°$ as $v \to v_S$ for a typical [Achenbach 1973] value $c_R = 0.932$. That is, separation would involve a substantial portion of the projection area in the subseismic limit.

9. Summary comments

Combining quasipolar coordinates with an analysis defined in terms of Cartesian coordinates produces solutions that can be seen as awkward hybrids. However, analytical expressions for contact zone traction in the quasipolar system are readily extracted. In any event, the approach was adopted in order to address problems without axial symmetry. Indeed no degree of symmetry is required. That imposed on contact zone C served to guarantee that a simple resultant force system could produce die sliding and rolling in the specified direction. Rolling contact by a sphere was considered because its 2D counterpart, the cylinder, is a standard rolling problem.

The assumption that key geometric features of the area projected by the rigid die onto the contact surface are preserved in the contact zone shape, or that the zone is essentially elliptical, is often accurate [Johnson 1985; Hills et al. 1993; Bayer 1994; Blau 1996]. It also avoids an iteration process based on, for example, maintenance of compression everywhere in the zone. Here, in addition to the Signorini requirement of bounded traction on the zone boundary, a requirement that resultant compressive force be stationary with respect to the traction was imposed. This gave expressions that defined the contact zone geometry. These indicated that the contact zone is often a distortion of the projected area. In particular, sliding/rolling speed tends to "flatten" the contact zone onto the line of travel, see [Rahman 1996]. Friction in sliding destroys any projection area symmetry, save that with respect to the line of travel. It is hoped that these results afford some insight into problems of 3D dynamic contact.

Appendix A

Consider integrals involving real parameters (X, Y) over the entire $\mathrm{Im}(p)$-axis P:

$$\frac{1}{2\pi i}\int_{\mathrm{P}} |p|\left(1, \frac{\sqrt{-p}}{\sqrt{p}}\right)\exp[pX - Y\sqrt{-p}\sqrt{p}]\frac{dp}{p} \quad (Y \geqslant 0). \tag{A1}$$

$\mathrm{Re}(\sqrt{\pm p}) \geqslant 0$ in the p-plane with, respectively, branch cuts $\mathrm{Im}(p) = 0$, $\mathrm{Re}(p) < 0$ and $\mathrm{Im}(p) = 0$, $\mathrm{Re}(p) > 0$. Specifically, for $\mathrm{Re}(p) = 0+$ and, respectively, $\mathrm{Im}(p) = q > 0$ and $\mathrm{Im}(p) = q < 0$:

$$\sqrt{-p} = \left|\frac{q}{2}\right|^{1/2}(1 \mp i), \quad \sqrt{p} = \left|\frac{q}{2}\right|^{1/2}(1 \pm i). \tag{A2}$$

Use of (A2) reduces (A1) to

$$\frac{1}{i\pi}\int_0^\infty (\cos qX, \sin qX)\exp(-Yq)\,dq. \tag{A3}$$

From standard [Peirce and Foster 1956] tables (A3) is evaluated as

$$\frac{1}{i\pi}\left(\frac{Y}{X^2+Y^2}, \frac{X}{X^2+Y^2}\right). \tag{A4}$$

It is noted that the X-derivative of (A4) gives the evaluation for integrals

$$\frac{1}{2\pi i}\int_{\mathrm{P}} |p|\left(1, \frac{\sqrt{-p}}{\sqrt{p}}\right)\exp(-pX - Y\sqrt{-p}\sqrt{p})\,dp \quad (Y>0). \tag{A5}$$

It is also noted [Stakgold 1967] that

$$\frac{1}{\pi}\frac{Y}{X^2+Y^2} \to \delta(X) \quad (Y\to 0). \tag{A6}$$

Here δ is the Dirac function.

Appendix B

Consider region Ξ of the $\mathrm{Re}(t)$-axis defined as $x_- < t < x_+$ and function

$$W(x) = \int_\Xi \frac{\Omega(t)\,dt}{t-x}, \quad |\mathrm{Re}\,\Omega(t)| < 1. \tag{B1}$$

For $x\in\Xi$, $W(x\pm i0) = w(x) \pm i\pi\Omega(x)$, where $w(x)$ is the principal value

$$w(x) = (vp)\int_\Xi \frac{\Omega(t)\,dt}{t-x}. \tag{B2}$$

For a function $g(t)$ that is bounded and piecewise continuous in Ξ the following relations hold for $x\in\Xi$:

$$G(x) = g(x)\cos\pi\Omega(x) + \mathrm{I}(g;x)\sin\pi\Omega(x), \tag{B3a}$$

$$\frac{1}{\pi}(vp)\int_\Xi \frac{G(t)}{t-x}\,dt = -g(x)\sin\pi\Omega(x) + \mathrm{I}(g;x)\cos\pi\Omega(x), \tag{B3b}$$

$$\int_\Xi G(t)\,dt = \int_\Xi g(t)\exp[-w(t)]\,dt. \tag{B3c}$$

In (B3a) and (B3b) the functional

$$\mathrm{I}(g;x) = \frac{1}{\pi}\exp w(x)(vp)\int_\Xi \frac{g(t)}{t-x}\exp[-w(t)]\,dt. \tag{B4}$$

For $x\notin\Xi$ (B3b) is replaced with

$$\frac{1}{\pi}\int_\Xi \frac{G(t)}{t-x}\,dt = \frac{1}{\pi}\exp W(x)\int_\Xi \frac{g(t)}{t-x}\exp[-w(t)]\,dt. \tag{B5}$$

For $\Omega(t) = \Omega < 0$ (constant), polynomial forms of $g(t)$ give explicit results, for example, for $g(t) = (t^0, t, t^2)$ the right-hand sides of (B3a) are

$$\left(\frac{x_+ - x}{x - x_-}\right)^{\Omega}, \quad (x + \Omega L)\left(\frac{x_+ - x}{x - x_-}\right)^{\Omega}, \quad \left[x^2 + \Omega(x + x_+) - \frac{\Omega}{2}(1 - \Omega)L^2\right]\left(\frac{x_+ - x}{x - x_-}\right)^{\Omega}. \tag{B6}$$

Similarly, the right-hand sides of (B5) are, respectively,

$$\frac{1}{\sin \pi\Omega}\left[\left(\frac{x - x_+}{x - x_-}\right)^{\Omega} - 1\right], \tag{B7a}$$

$$\frac{1}{\sin \pi\Omega}\left[x\left(\frac{x - x_+}{x - x_-}\right)^{\Omega} - x - \Omega L\right], \tag{B7b}$$

$$\frac{1}{\sin \pi\Omega}\left[x^2\left(\frac{x - x_+}{x - x_-}\right)^{\Omega} - x^2 - \Omega(x + x_+) + \frac{\Omega}{2}(1 - \Omega)L^2\right]. \tag{B7c}$$

Here $L = x_+ - x_-$ is the width of Ξ. The results in (B1)–(B7) are standard, and in this case, taken from [Brock and Georgiadis 2000; Brock 2004].

References

[Achenbach 1973] J. D. Achenbach, *Wave propagation in elastic solids*, North-Holland Series in Applied Mathematics and Mechanics **16**, North-Holland, Amsterdam, 1973.

[Ahmadi et al. 1983] N. Ahmadi, L. M. Keer, and T. Mura, "Non-Hertzian contact stress analysis for an elastic half-space: normal and sliding contact", *Int. J. Solids Struct.* **19**:4 (1983), 357–373.

[Barber 1983] J. R. Barber, "The solution of elasticity problems for the half-space by the method of Green and Collins", *Appl. Sci. Res.* **40**:2 (1983), 135–157.

[Barber 1992] J. R. Barber, *Elasticity*, Solid Mechanics and its Applications **12**, Kluwer, Dordrecht, 1992.

[Barwell 1979] F. T. Barwell, *Bearing systems: principles and practice*, Oxford University Press, Oxford, 1979.

[Bayer 1994] R. G. Bayer, *Mechanical wear prediction and prevention*, Mechanical Engineering **91**, Marcel Dekker, New York, 1994.

[Blau 1996] P. J. Blau, *Friction science and technology*, Mechanical Engineering **100**, Marcel Dekker, New York, 1996.

[Brock 2004] L. M. Brock, "Coupled thermoelastic analysis of perfect rolling contact: solution behavior near yield initiation", *J. Therm. Stresses* **27**:5 (2004), 383–403.

[Brock and Georgiadis 2000] L. M. Brock and H. G. Georgiadis, "Siding contact with friction of a thermoelastic solid at subsonic, transonic and supersonic speeds", *J. Therm. Stresses* **23**:7 (2000), 629–656.

[Churilov 1978] V. A. Churilov, "Action of an elliptical stamp moving at a constant speed on an elastic half-space", *Prikl. Mat. Mekh.* **42**:6 (1978), 1074–1079. In Russian; translated in *J. Appl. Math. Mech.* **42**:6 (1978), 1176–1182.

[Craggs and Roberts 1967] J. W. Craggs and A. M. Roberts, "On the motion of a heavy cylinder over the surface of an elastic half-space", *J. Appl. Mech.* (*ASME*) **34**:1 (1967), 207–209.

[Erdogan 1985] F. Erdogan, "Mixed boundary value problems in mechanics", pp. 1–86 in *Mechanics today*, vol. 4, edited by S. Nemat-Nasser, Pergamon, New York, 1985.

[Georgiadis and Barber 1993] H. G. Georgiadis and J. R. Barber, "On the super-Rayleigh/subseismic elastodynamic indentation problem", *J. Elasticity* **31**:3 (1993), 141–161.

[Hills et al. 1993] D. A. Hills, D. Nowell, and A. Sackfield, *Mechanics of elastic contacts*, Butterworth-Heinemann, Oxford, 1993.

[Johnson 1985] K. L. Johnson, *Contact mechanics*, Cambridge University Press, Cambridge, 1985.

[Kalker 1990] J. J. Kalker, *Three-dimensional bodies in elastic contact*, Solid Mechanics and its Applications **2**, Kluwer, Dordrecht, 1990.

[Peirce and Foster 1956] B. O. Peirce and R. M. Foster, *A short table of integrals*, 4th ed., Ginn, New York, 1956.

[van der Pol and Bremmer 1950] B. van der Pol and H. Bremmer, *Operational calculus: based on the two-sided Laplace integral*, Cambridge University Press, Cambridge, 1950.

[Rahman 1996] M. Rahman, "Hertz problem for a rigid punch moving across the surface of a semi-infinite elastic solid", *Z. Math. Phys.* **47**:4 (1996), 601–615.

[Sneddon 1972] I. N. Sneddon, *The use of integral transforms*, McGraw-Hill, New York, 1972.

[Stakgold 1967] I. S. Stakgold, *Boundary value problems in mathematical physics*, vol. 1, MacMillan, New York, 1967. Reprinted in Classics in Applied Mathematics **29**, SIAM, Philadelphia, 2000.

Received 6 Mar 2012. Revised 27 Mar 2012. Accepted 30 May 2012.

LOUIS MILTON BROCK: brock@engr.uky.edu
Department of Mechanical Engineering, University of Kentucky, Lexington, KY 40506-0503, United States
http://www.engr.uky.edu/me/faculty_staff/brock.html

JOURNAL OF MECHANICS OF MATERIALS AND STRUCTURES
Vol. 7, No. 5, 2012
dx.doi.org/10.2140/jomms.2012.7.485

msp

BUCKLING ANALYSIS OF NONUNIFORM COLUMNS WITH ELASTIC END RESTRAINTS

SEVAL PINARBASI

Since compression members, such as columns in a multistory building, are mostly the key elements in a structure, even a small decrease in their load carrying capacity can lead to catastrophic failure of the structure. A compression member has to be designed to satisfy not only the strength and serviceability requirements, but also the stability requirements. In fact, the behavior of a slender column is mostly governed by the stability limit states. In an attempt to construct ever-stronger and ever-lighter structures, many engineers currently design slender high strength columns with variable cross sections and various end conditions. Even though buckling behavior of uniform columns with ideal boundary conditions have extensively been studied, there are limited studies in the literature on buckling analysis of nonuniform columns with elastic end restraints since such an analysis requires the solution of more complex differential equations for which it is usually impractical or sometimes even impossible to obtain exact solutions. This paper shows that variational iteration method (VIM) can successfully be used for this purpose. VIM results obtained for columns of constant cross sections, for which exact results are available in the literature, agree with the exact results perfectly, verifying the efficiency of VIM in the analysis of this special type of buckling problem. It is also shown that unlike exact solution procedures, variational iteration algorithms can easily be used even when the variation of column stiffness along its length and/or the end conditions are rather complex.

1. Introduction

Compression members subjected to uniform axial loads are commonly used in many engineering applications. Columns in a multistory building, for example, are the key structural elements which support the heavy weight of the structure. Even a small decrease in their load carrying capacity can lead to catastrophic failure of the structure. Compression members differ from tension members in that the design of the former has to consider not only the strength and serviceability requirements but also the stability requirements. In fact, the behavior of a slender column is mostly governed by the stability limit states. For this reason, many international design specifications include specific provisions on stability of compression members.

Since 1744, when the Swiss mathematician Leonhard Euler published his famous buckling formula, research on stability of slender columns has increasingly continued. This continuous interest on stability problems is based mainly on the desire of constructing "ever-stronger" and "ever-lighter" structures. This "optimum structure" approach has led most engineers to design columns with higher strength and lighter weight. Unfortunately, design engineers are lack of sufficient guidance on design of nonuniform columns since most of the provisions on compression members are developed for uniform columns.

Keywords: variational iteration method, elastic buckling, stability, nonuniform column, elastic end restraints.

Elastic buckling behavior of uniform columns has extensively been investigated by many researchers. For fully developed buckling theory and the related exact solutions, one can refer to one of the classical textbooks on structural stability (e.g., [Timoshenko 1961; Chajes 1974; Wang et al. 2005; Simitses and Hodges 2006]). On the other hand, there are very few studies in the literature on columns with variable flexural stiffness since such an analysis requires the solution of more complex differential equations. In many cases, it is impractical and sometimes even impossible to obtain closed-form solutions to these problems.

When the buckling studies in the literature are examined, it is also seen that most of the studies on column buckling assume ideal end conditions. Such ideal boundary conditions can realistically model the real end conditions in some special structures, such as columns in one-story buildings, vertical and diagonal elements in truss structures and bracing elements in braced frames. However, in a general multistory building, the ends of the columns are neither hinged nor fully fixed or free. Instead, they are commonly connected to beams and the restraining effect of the beams on the column ends strongly depends on the type of the beam-to-column connection. In addition, the behavior of a column in a frame is significantly influenced from the existence and amount of the bracing members in the frame. For this reason, the buckling solutions obtained for columns of ideal end conditions cannot always be safely used for columns with elastic end restraints.

However, as in the case of buckling analysis of nonuniform columns, buckling analysis of columns with elastic end restraints is difficult to handle due to the complex boundary conditions and studies in the literature on this subject are also very limited (e.g., [Eisenberger and Clastornik 1987; Li 2000; 2001; 2003; Ozturk and Sabuncu 2005; Atanackovic and Novakovic 2006; Tan and Yuan 2008; Singh and Li 2009; Atanackovic et al. 2010]). For this reason, most design specifications offer engineers design charts, instead of design formulas, for the design of such framed columns. These "alignment" charts are drawn from the buckling (characteristic) equation derived for uniform columns with elastic end springs, which needs special techniques to solve due to its high nonlinearity, by making some assumptions on the stiffnesses of the restraints (e.g., the assumption of identical slopes at the ends of the beam). Thus, even these charts do not provide exact values. Moreover, they are applicable only to uniform columns. However, as mentioned previously, due to economical and esthetic issues, nowadays, many columns are designed with variable stiffness.

Consequently, there is a need for a practical tool to solve buckling problems of nonuniform columns with elastic end restraints. In recent years, many analytical approaches; such as, variational iteration method (VIM), homotopy perturbation method (HPM), differential quadrature method (DQM) are proposed for the solution of nonlinear equations and many researchers (e.g., [Arbabi and Li 1991; Du et al. 1996; Rosa and Franciosi 1996; Cailo and Elishakoff 2004; Civalek 2004; Aydogdu 2008; Malekzadeh and Karami 2008; Atay 2009; Coşkun 2009; 2010; Huang and Luo 2011; Ozturk and Coşkun 2011; Serna et al. 2011; Yuan and Wang 2011]) have shown that complex engineering problems, such as buckling and vibration problems, can easily be solved using these techniques. A kind of nonlinear analytical technique which was proposed by He [1999], variational iteration method (VIM) has many successful applications to various kinds of nonlinear engineering problems [Abulwafa et al. 2007; Batiha et al. 2007; Coşkun and Atay 2007; Ganji and Sadighi 2007; Ganji et al. 2007; 2008; Sweilam and Khader 2007; Coşkun and Atay 2008; Miansari et al. 2008; Shou and He 2008; Ozturk 2009; Liu and Gurram 2009; Atay 2010; Coşkun et al. 2011; Geng 2011; Yang and Chen 2011]. As shown in [Coşkun and Atay 2009;

Atay and Coşkun 2009; Okay et al. 2010; Pinarbasi 2011], VIM is an effective and powerful technique that can successfully be used in the analysis of elastic stability of compression and flexural members with variable cross sections under different loading and boundary conditions. In this paper, this powerful technique is used to determine the buckling loads of slender columns with elastic end restraints. To the best knowledge of authors, exact solutions to this problem are available only for some particular cases of uniform columns. For this reason, before analyzing the columns with variable cross sections, the buckling loads of columns with constant cross sections are determined using classical variational iteration algorithm and VIM results are compared with the exact results. After verifying the efficiency of VIM in the analysis of this special type of buckling problem, stability of columns with variable flexural stiffness is studied. In the analyses, columns with two different types of stiffness variations along their lengths; linear and exponential variations, and with various end conditions are considered. Buckling loads obtained for these nonuniform columns are computed using classical variational iteration algorithm and compared with those obtained for uniform columns.

2. Elastic buckling of columns with elastic end restraints

General buckling equation and related boundary conditions. Consider an axially loaded column of variable flexural rigidity EI along its length L with elastic end restraints as shown in Figure 1, left. Assume that the lateral displacement and rotation of the top end of the column are restrained, respectively, by an extensional spring with elastic spring constant α_0 and a rotational spring with elastic spring constant β_0. Further assume that similar springs with spring constants α_L and β_L restrain the bottom end of the column.

Figure 1, middle, shows the buckled shape of such a column under a uniaxial load of P. In the figure, M_A, M_B and V show support reactions. As can be seen from that figure, the origin of x-y coordinate system is located at the top end of the column. The equilibrium equation at an arbitrary section of the

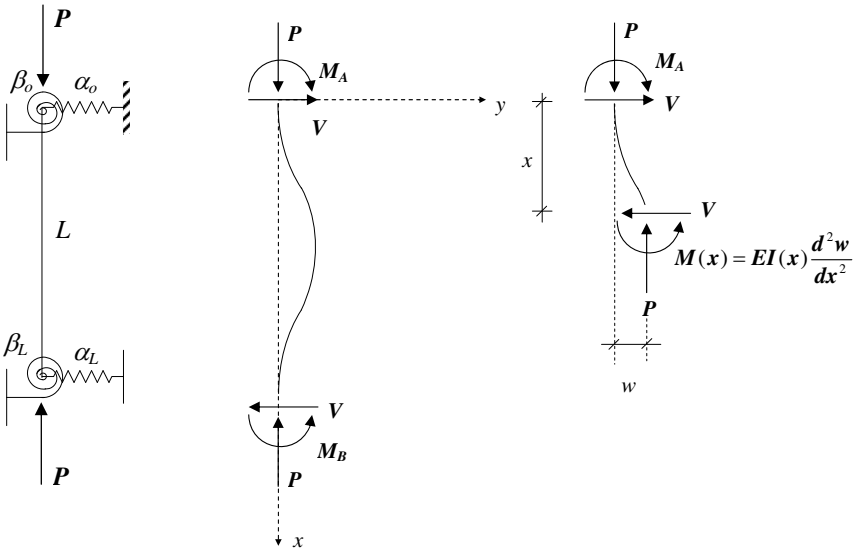

Figure 1. An axially loaded column with elastic end restraints. Left: undeformed shape. Middle: deformed (buckled) shape. Right: free body diagram for internal forces.

column can be written from the free body diagram shown in Figure 1, right as

$$M(x) + Pw(x) - Vx - M_A = 0, \tag{1}$$

where $w(x)$, or simply w, is the displacement component in y direction. Using the well-known moment-curvature relation

$$M(x) = EI(x)\frac{d^2w}{dx^2}, \tag{2}$$

Equation (1) can be rewritten as

$$EI(x)\frac{d^2w}{dx^2} + Pw = Vx + M_A. \tag{3}$$

Differentiation of (3) with respect to x gives shear force in the column at any section:

$$V = EI(x)\frac{d^3w}{dx^3} + \frac{d[EI(x)]}{dx}\frac{d^2w}{dx^2} + P\frac{dw}{dx}. \tag{4}$$

Further differentiation of (4) with respect to x yields the governing equation of the buckling problem:

$$\frac{d^4w}{dx^4} + \frac{2}{EI(x)}\frac{d[EI(x)]}{dx}\frac{d^3w}{dx^3} + \frac{1}{EI(x)}\left(P + \frac{d^2[EI(x)]}{dx^2}\right)\frac{d^2w}{dx^2} = 0. \tag{5}$$

It is to be noted that the governing equation (5) is applicable to all columns regardless of their end conditions.

Using (2) and (3), the boundary conditions at the top and bottom end of the column can be written as

$$\text{at } x = 0; \quad \beta_0\frac{dw}{dx} = EI(x)\frac{d^2w}{dx^2} \quad \text{and} \quad \alpha_0 w = -\left(EI(x)\frac{d^3w}{dx^3} + \frac{d[EI(x)]}{dx}\frac{d^2w}{dx^2} + P\frac{dw}{dx}\right) \tag{6}$$

and

$$\text{at } x = L; \quad \beta_L\frac{dw}{dx} = -EI(x)\frac{d^2w}{dx^2} \quad \text{and} \quad \alpha_L w = EI(x)\frac{d^3w}{dx^3} + \frac{d[EI(x)]}{dx}\frac{d^2w}{dx^2} + P\frac{dw}{dx}. \tag{7}$$

Columns with constant stiffness. When flexural stiffness of the column does *not* change along its length, in other words, when $EI(x) = EI$, the governing equation (5) and the related boundary conditions (6) and (7) reduce to the simpler forms

$$\frac{d^4w}{dx^4} + \frac{P}{EI}\frac{d^2w}{dx^2} = 0 \tag{8}$$

with

$$\frac{d^2w}{dx^2} - \frac{\beta_0}{EI}\frac{dw}{dx} = 0 \quad \text{and} \quad \frac{d^3w}{dx^3} + \frac{P}{EI}\frac{dw}{dx} + \frac{\alpha_0}{EI}w = 0 \qquad \text{at } x = 0, \tag{9}$$

and

$$\frac{d^2w}{dx^2} + \frac{\beta_L}{EI}\frac{dw}{dx} = 0 \quad \text{and} \quad \frac{d^3w}{dx^3} + \frac{P}{EI}\frac{dw}{dx} - \frac{\alpha_L}{EI}w = 0 \qquad \text{at } x = L. \tag{10}$$

For easier computations, these equations can be written in nondimensional form as

$$(\bar{w})'''' + \lambda(\bar{w})'' = 0 \tag{11}$$

with

$$(\bar{w})'' - \bar{\beta}_0(\bar{w})' = 0 \quad \text{and} \quad (\bar{w})''' + \lambda(\bar{w})' + \bar{\alpha}_0\bar{w} = 0 \qquad \text{at } \bar{x} = 0, \tag{12}$$

$$(\bar{w})'' + \bar{\beta}_L(\bar{w})' = 0 \quad \text{and} \quad (\bar{w})''' + \lambda(\bar{w})' - \bar{\alpha}_L\bar{w} = 0 \qquad \text{at } \bar{x} = 1, \tag{13}$$

where $\bar{w} = w/L$ and $\bar{x} = x/L$, primes denote differentiation with respect to $\bar{x}$, the normalized spring stiffnesses are

$$\bar{\beta}_0 = \frac{\beta_0 L}{EI}, \quad \bar{\beta}_L = \frac{\beta_L L}{EI}, \quad \bar{\alpha}_0 = \frac{\alpha_0 L^3}{EI} \qquad \text{and} \quad \bar{\alpha}_L = \frac{\alpha_L L^3}{EI} \tag{14}$$

and the normalized critical load is

$$\lambda = \frac{PL^2}{EI}. \tag{15}$$

Since exact solutions are available in the literature for uniform columns and since these solutions correspond to limiting conditions for variable stiffness cases, before studying the buckling problems of nonuniform columns, the buckling loads of uniform columns are to be determined and compared with the exact solutions available in the literature.

Columns with variable stiffness.

Columns with linearly varying stiffness. When flexural stiffness of the column decrease along its length linearly, i.e., when

$$EI(x) = EI(1 - b\tfrac{x}{L}), \tag{16}$$

where b is a constant determining the "sharpness" of the stiffness change along the column length, the governing equation becomes

$$\frac{d^4w}{dx^4} - \frac{2b/L}{(1 - bx/L)}\frac{d^3w}{dx^3} + \frac{P}{EI(1 - bx/L)}\frac{d^2w}{dx^2} = 0, \tag{17}$$

which can be written in nondimensionalized form as follows:

$$(\bar{w})'''' - \frac{2b}{(1 - b\bar{x})}(\bar{w})''' + \frac{\lambda}{(1 - b\bar{x})}(\bar{w})'' = 0. \tag{18}$$

Similarly, the related boundary conditions can be expressed in nondimensional form:

$$\text{at } \bar{x} = 0; \qquad (\bar{w})'' - \bar{\beta}_0(\bar{w})' = 0, \qquad (\bar{w})''' - b(\bar{w})'' + \lambda(\bar{w})' + \bar{\alpha}_0\bar{w} = 0, \tag{19}$$

$$\text{at } \bar{x} = 1; \qquad (\bar{w})'' + \frac{\bar{\beta}_L}{(1 - b)}(\bar{w})' = 0, \qquad (\bar{w})''' - \frac{b}{(1 - b)}(\bar{w})'' + \frac{\lambda}{(1 - b)}(\bar{w})' - \frac{\bar{\alpha}_L}{(1 - b)}\bar{w} = 0. \tag{20}$$

Columns with exponentially varying stiffness. If the bending stiffness of the column changes exponentially along its length, i.e., if

$$EI(x) = EIe^{-a(x/L)}, \tag{21}$$

where a is a positive constant determining the "sharpness" of the stiffness change, the governing equation becomes

$$\frac{d^4w}{dx^4} - \frac{2a}{L}\frac{d^3w}{dx^3} + \left(\frac{P}{EIe^{-a(x/L)}} + \frac{a^2}{L^2}\right)\frac{d^2w}{dx^2} = 0, \tag{22}$$

which, when written in nondimensionalized form, becomes

$$(\bar{w})'''' - 2a(\bar{w})''' + (\lambda e^{a\bar{x}} + a^2)(\bar{w})'' = 0. \tag{23}$$

Similarly, the related boundary conditions can be expressed in nondimensional form as

$$(\bar{w})'' - \bar{\beta}_0(\bar{w})' = 0 \quad \text{and} \quad (\bar{w})''' - a(\bar{w})'' + \lambda(\bar{w})' + \bar{\alpha}_0\bar{w} = 0, \qquad \text{at } \bar{x} = 0, \tag{24}$$

$$(\bar{w})'' + \bar{\beta}_L e^a(\bar{w})' = 0 \quad \text{and} \quad (\bar{w})''' - a(\bar{w})'' + \lambda e^a(\bar{w})' - \bar{\alpha}_L e^a\bar{w} = 0 \qquad \text{at } \bar{x} = 1. \tag{25}$$

3. VIM formulations for the studied buckling problems

According to the variational iteration method (VIM) [He 1999], a general homogeneous nonlinear differential equation can be written in the form

$$Lw(x) + Nw(x) = 0, \tag{26}$$

where L is a linear operator and N is a nonlinear operator, and the "correction functional" is

$$w_{n+1}(x) = w_n(x) + \int_0^x \lambda(\xi)\big(Lw_n(\xi) + N\tilde{w}_n(\xi)\big)\,d\xi. \tag{27}$$

In (27), $\lambda(\xi)$ is a general Lagrange multiplier that can be identified optimally via variational theory, w_n is the n-th approximate solution and $\tilde{w}_n$ denotes a restricted variation, i.e., $\delta\tilde{w}_n = 0$. As summarized in [He et al. 2010] for a fourth order differential equation such as the equations of the problem considered in this paper, $\lambda(\xi)$ equals to

$$\lambda(\xi) = \frac{(\xi - x)^3}{6}. \tag{28}$$

The original variational iteration algorithm proposed in [He 1999] has the iteration formula

$$w_{n+1}(x) = w_n(x) + \int_0^x \lambda(\xi)\big(Lw_n(\xi) + Nw_n(\xi)\big)\,d\xi. \tag{29}$$

In a recent paper, He et al. [2010] proposed two additional variational iteration algorithms for solving various types of differential equations. These algorithms can be expressed as follows:

$$w_{n+1}(x) = w_0(x) + \int_0^x \lambda(\xi)\big(Nw_n(\xi)\big)\,d\xi, \tag{30}$$

$$w_{n+2}(x) = w_{n+1}(x) + \int_0^x \lambda(\xi)\big(Nw_{n+1}(\xi) - Nw_n(\xi)\big)\,d\xi. \tag{31}$$

Thus, the three VIM iteration algorithms for (18), as an example, can be written as

$$\bar{w}_{n+1}(x) = \bar{w}_n(x) + \int_0^x \frac{(\xi - x)^3}{6}\left(\bar{w}_n''''(\xi) - \frac{2b}{1-b\xi}\bar{w}_n'''(\xi) + \frac{\lambda}{1-b\xi}\bar{w}_n''(\xi)\right)d\xi,$$

$$\bar{w}_{n+1}(x) = \bar{w}_0(x) + \int_0^x \frac{(\xi - x)^3}{6}\left(-\frac{2b}{1-b\xi}\bar{w}_n'''(\xi) + \frac{\lambda}{1-b\xi}\bar{w}_n''(\xi)\right)d\xi,$$

$$\bar{w}_{n+2}(x) = \bar{w}_{n+1}(x) + \int_0^x \frac{(\xi - x)^3}{6}\left(-\frac{2b}{1-b\xi}(\bar{w}_{n+1}'''(\xi) - \bar{w}_n'''(\xi)) + \frac{\lambda}{1-b\xi}(\bar{w}_{n+1}''(\xi) - \bar{w}_n''(\xi))\right)d\xi.$$

Similar algorithms can easily be written for (11) and (23). In order to determine the most effective VIM algorithm to be used in the current study, one single case of a buckling equation (linearly varying stiffness case with $b = 0.3$) is solved using all three algorithms. Parallel to the findings of Pinarbasi [2011], all iteration algorithms yield exactly the same results. For this reason, the classical VIM algorithm is decided to be used throughout the study.

4. Buckling loads for columns with elastic restraints

The general buckling problems formulated in Section 2 are specialized to three different end conditions shown in Figure 2. In Case I (left), the bottom end of the column which is free to rotate ($\beta_L \to 0$) is laterally restrained with an extensional spring (with α_L) while the top end of the column is fixed ($\alpha_0 \to \infty$, $\beta_0 \to \infty$). Such a column can exist in a single story frame where the beam-to-column connections are simple shear connections. Case II (Figure 2, middle) investigates an interior column in a multistory building whose lateral stiffness is provided by laterally stiff elements such as lateral bracings or reinforced concrete walls. In such a "sway-prevented structure", the relative lateral displacement of one end of the column with respect to the other end is so small that it is neglected. For this reason, in Case II, the stiffnesses of linear springs are assumed to approach infinity ($\alpha_0 \to \infty$, $\alpha_L \to \infty$) while rotational spring stiffnesses (β_0 and β_L) are let have any value. In Case III (Figure 2, right), the relative lateral displacement of one end of the column with respect to the other end is *not* small so it cannot be neglected. Such columns can be seen in a "sway-permitted" structure whose lateral stiffness is provided only by flexural stiffnesses of frame members. For simplicity, the lateral stiffness of the extensional spring at the top end of the column is taken zero, while rotational spring stiffnesses (β_0 and β_L) can have any value.

Columns with constant stiffness. The exact solution to the differential equation (11) has the form

$$\bar{w} = C_1 \sin\sqrt{\lambda}\bar{x} + C_2 \cos\sqrt{\lambda}\bar{x} + C_3\bar{x} + C_4, \tag{32}$$

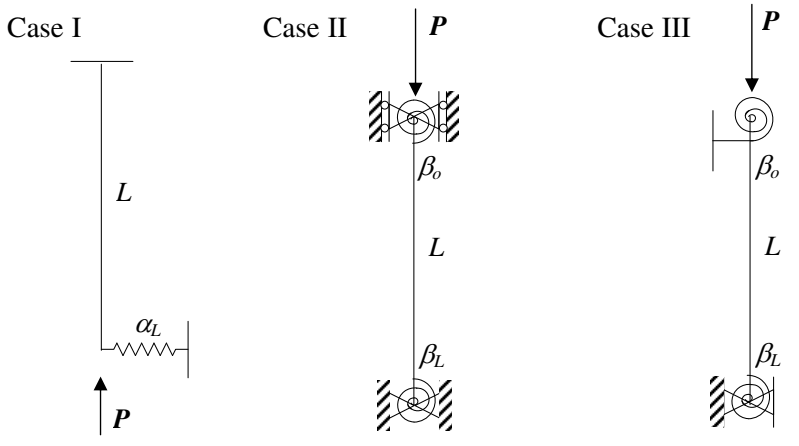

Figure 2. The three cases (boundary conditions) studied in the paper. Case I: $\alpha_0 \to \infty$, $\beta_0 \to \infty$, $\beta_L \to 0$. Case II: $\alpha_0 \to \infty$, $\alpha_L \to \infty$. Case III: $\alpha_0 \to 0$, $\alpha_L \to \infty$.

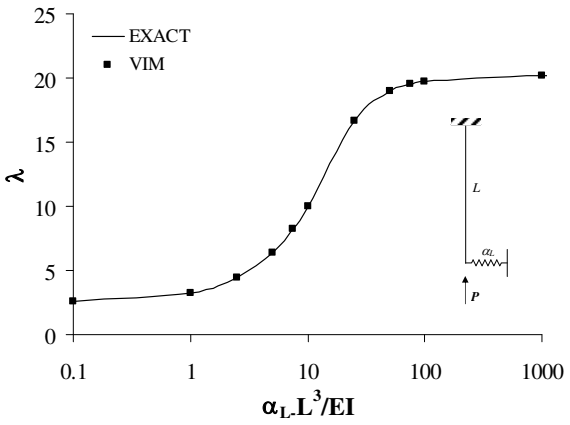

	λ	
$\alpha_L L^3/EI$	EXACT	VIM
0.1	2.54841	2.54841
1	3.27349	3.27349
2.5	4.46442	4.46442
5	6.39207	6.39207
7.5	8.23092	8.23092
10	9.95634	9.95634
25	16.6435	16.6435
50	18.9922	18.9922
75	19.4958	19.4958
100	19.7035	19.7035
1000	20.1496	20.1496

Figure 3. Case I — columns with constant stiffness — variation of normalized buckling load with normalized linear spring stiffness.

where C_i (i=1,2,3,4) are evaluated from the related boundary conditions. In Case I, the boundary conditions are

$$[(\bar{w})']_{\bar{x}=0} = 0, \quad [\bar{w}]_{\bar{x}=0} = 0, \quad [(\bar{w})'']_{\bar{x}=1} = 0 \quad \text{and} \quad [(\bar{w})''' + \lambda(\bar{w})' - \bar{\alpha}_L \bar{w}]_{\bar{x}=1} = 0. \tag{33}$$

By substituting (32) into these boundary conditions, four homogeneous equations are obtained. These equations can be put into matrix form:

$$[M(\lambda)]\{C\} = \{0\}, \tag{34}$$

where $\{C\} = \{C_1\ C_2\ C_3\ C_4\}^T$. Thus, the problem reduces to an eigenvalue problem. For a nontrivial solution, the determinant of the coefficient matrix has to be zero. The smallest possible real root of the characteristic equation, which is obtained by equating the determinant of the coefficient matrix to zero, gives the nondimensional buckling load in the first buckling mode. For some particular values of α_L, the exact values are calculated and plotted in Figure 3, in a semilogarithmic scale.

Even though the differential equation to be solved in this case is relatively simple, when the exact solution is tried to be obtained, finding the smallest root of the resulting characteristic equation which contains trigonometric functions can be somewhat difficult. It is observed that the result is very sensitive to the initial guess. So, one should be aware of that a couple of trials may be required to find the correct root of the characteristic equation.

The same problem is also studied using VIM. The initial approximation is selected as a third degree polynomial with four unknown coefficients A_i (i=1,2,3,4):

$$\bar{w}_0 = A_1(\bar{x})^3 + A_2(\bar{x})^2 + A_3\bar{x} + A_4. \tag{35}$$

Using the first iteration algorithm and conducting nine iterations, $\bar{w}_9$ is obtained. Through substitution in the boundary conditions (33), four homogeneous equations are obtained. Similar to the exact solution procedure, by making the determinant of the coefficient matrix of these equations equal to zero, the characteristic equation for the related bucking problem is obtained. The roots of the characteristic equation give the normalized buckling loads. Since the characteristic equation is a polynomial, one can easily

	λ								
$\beta_0 L/EI$		$\beta_L = \beta_0$			$\beta_L = 0$			$\beta_L \to \infty$	
	Exact	VIM (9 iter)	VIM (17 iter)	Exact	VIM (9 iter)	VIM (17 iter)	Exact	VIM (9 iter)	VIM (17 iter)
0	9.870	9.8696	9.8696	9.870	9.8696	9.8696	20.191	20.1907	20.1907
0.5	11.772	11.7719	11.7719	10.798	10.7978	10.7978	21.659	21.6594	21.6594
1	13.492	13.4924	13.4924	11.598	11.5982	11.5982	22.969	22.9688	22.9688
2	16.463	16.4634	16.4634	12.894	12.8944	12.8944	25.182	25.1822	25.1822
4	20.957	20.9568	20.9568	14.660	14.6602	14.6602	28.397	28.3971	28.3969
10	28.168	28.1683	28.1677	17.076	17.0763	17.0763	33.153	33.1546	33.1532
20	**30.355**	**32.7846**	**32.7819**	18.417	18.4173	18.4173	35.902	35.9059	35.9019
∞	39.478	39.4916	39.4784	20.191	20.1908	20.1907	39.478	39.4916	39.4784

Table 1. Case II — columns with constant stiffness — comparison of VIM solutions with exact solutions [Wang et al. 2005].

	λ								
$\beta_0 L/EI$		$\beta_L = \beta_0$			$\beta_L = 0$			$\beta_L \to \infty$	
	Exact	VIM (9 iter)	VIM (17 iter)	Exact	VIM (9 iter)	VIM (17 iter)	Exact	VIM (9 iter)	VIM (17 iter)
0	0.000	0.0000	0.0000	0.000	0.0000	0.0000	2.4674	2.46740	2.46740
0.5	0.922	0.9220	0.9220	0.4268	0.42676	0.42676	3.3731	3.37309	3.37309
1	1.7071	1.7071	1.7071	0.7402	0.74017	0.74017	4.1159	4.11586	4.11586
2	2.9607	2.9607	2.9607	1.1597	1.15966	1.15966	5.2392	5.23920	5.23920
4	4.6386	4.6386	4.6386	1.5992	1.59919	1.59919	6.6071	6.60712	6.60712
10	6.9047	6.9047	6.9047	**2.0517**	**2.04167**	**2.04167**	8.1955	8.19547	8.19547
20	8.1667	8.1667	8.1667	2.2384	2.23840	2.23840	8.9583	8.95831	8.95831
∞	9.8696	9.8696	9.8696	2.4674	2.46740	2.46740	9.8696	9.86960	9.86960

Table 2. Case III — columns with constant stiffness — comparison of VIM solutions with exact solutions [Wang et al. 2005].

compute its all roots. Selecting the smallest root is no more tedious. For comparison, VIM results are also plotted in Figure 3, which shows perfect agreement with the exact results.

For Case II and Case III, the characteristic equations of the buckling problems were derived by Wang et al. [2005]. They also tabulated exact results for some particular values of spring stiffnesses. In order to evaluate the efficiency of VIM, approximate solutions are obtained for the same values of spring stiffnesses using classical iteration algorithm and VIM results are compared with the exact results given in [Wang et al. 2005] in Tables 1 and 2. The same initial approximation chosen in Case I, namely, Equation (35), is used also in these two cases. Normalized buckling loads are computed for two different number of iterations; nine and seventeen.

From (12) and (13), for uniform columns, the boundary conditions for Case II become

$$[(\bar{w})'' - \bar{\beta}_0(\bar{w})']_{\bar{x}=0} = 0, \quad [\bar{w}]_{\bar{x}=0} = 0, \quad [(\bar{w})'' + \bar{\beta}_L(\bar{w})']_{\bar{x}=1} = 0 \quad \text{and} \quad [\bar{w}]_{\bar{x}=1} = 0 \tag{36}$$

and the boundary conditions for Case III become

$$[(\bar{w})'' - \bar{\beta}_0(\bar{w})']_{\bar{x}=0} = 0, \quad [(\bar{w})''' + \lambda(\bar{w})']_{\bar{x}=0} = 0, \quad [(\bar{w})'' + \bar{\beta}_L(\bar{w})']_{\bar{x}=1} = 0, \quad [\bar{w}]_{\bar{x}=1} = 0. \tag{37}$$

From Tables 1 and 2, it can be seen that even the VIM results obtained with nine iterations are sufficiently close to the exact results. Still, by increasing the number of iterations, the exact results can be obtained even when spring stiffnesses converge infinity. One can see that only one result in Table 1, shown in bold, does not match. This corresponds to the case when $\beta_0 = \beta_L = 20$. Considering that all other results match perfectly, this discrepancy may be due to a misprint in the reference. A similar, but smaller, mismatch occurs in Table 2, when $\beta_0 = 10$ and $\beta_L = 0$.

Figure 3 and Tables 1 and 2 clearly show that VIM is a powerful technique in predicting buckling loads of uniform columns with elastic restraints. The excellent match of VIM solutions with exact results also encourages the use of this practical technique in buckling problems of nonuniform columns, whose exact solutions are impractical or sometimes even impossible to derive.

Columns with variable stiffness. Although it is somewhat easy to derive closed form solutions for buckling problems of uniform columns, which has a fourth order homogenous differential equation with constant coefficients, it may be relatively difficult to obtain exact results for buckling of nonuniform columns. To the best knowledge of author, there are no such solutions available in the literature. For this reason, in this section of the paper, only the VIM results obtained using the classical VIM iteration algorithm will be presented.

Similar to the constant stiffness cases studied in the previous section, the iterations in variable stiffness cases are initiated with the simple approximation given in (35). To simplify the integration processes, the variable coefficients in the iteration integrals are expanded in series using nine terms and the normalized buckling loads are obtained from ninth approximate solution.

For each case illustrated in Figure 2, the normalized buckling loads of columns with variable (linearly/exponentially varying) stiffness are computed using classical VIM iteration algorithm for various values of normalized spring stiffness(es) (i.e., for various values of α_L for Case I and of β_0 and β_L for Case II and Case III) and for various degrees of stiffness changes (i.e., for various values of b or a). The numerical results are presented in Tables 3 and 4 for Case I, Tables 5–10 for Case II, and Tables 11–16 for Case III. The tabulated results can be used directly by structural engineers designing columns with linearly or exponentially varying stiffness along their lengths restrained with nonclassical elastic end supports.

It can be valuable to investigate the effect of the degree of stiffness nonlinearity on buckling loads of nonuniform columns by plotting some representative graphs from the above tabulated results. In the following plots, four particular cases of linear (b={0, 0.3, 0.5, 0.7}) and exponential (a={0, 0.5, 1.0, 2.0}) stiffness changes are studied for each end conditions illustrated in Figure 2. As can be inferred from Figure 4, whose two parts plot the variation of bending stiffness of a column with the selected stiffness changes through its length, the cases for b=0 and a=0 actually correspond to the uniform stiffness cases.

	$\alpha_L L^3/EI$								
b	0	0.1	0.25	0.5	1	2.5	5	10	100
0.0	2.4674	2.5484	2.6698	2.8716	3.2735	4.4644	6.3921	9.9563	19.7035
0.1	2.3928	2.4734	2.5940	2.7946	3.1940	4.3761	6.2843	9.7821	18.7228
0.2	2.3155	2.3956	2.5154	2.7147	3.1112	4.2835	6.1696	9.5904	17.7134
0.3	2.2351	2.3145	2.4335	2.6313	3.0246	4.1857	6.0464	9.3767	16.6704
0.4	2.1511	2.2299	2.3479	2.5440	2.9337	4.0819	5.9128	9.1353	15.5871
0.5	2.0643	2.1424	2.2593	2.4534	2.8389	3.9723	5.7681	8.8606	14.4553
0.6	1.9801	2.0574	2.1730	2.3650	2.7460	3.8630	5.6184	8.5544	13.2674
0.7	1.9170	1.9936	2.1083	2.2985	2.6757	3.7777	5.4922	8.2475	12.0251
0.8	1.8623	1.9384	2.0522	2.2410	2.6147	3.7020	5.3692	7.8866	10.6673

Table 3. Case I — columns with linearly varying stiffness.

	$\alpha_L L^3/EI$								
a	0	0.1	0.25	0.5	1	2.5	5	10	100
0.00	2.4674	2.5484	2.6698	2.8716	3.2735	4.4644	6.3921	9.9563	19.7035
0.25	2.2868	2.3667	2.4863	2.6851	3.0807	4.2499	6.1288	9.5241	17.4010
0.50	2.1121	2.1121	2.3085	2.5041	2.8929	4.0380	5.8616	9.0572	15.3231
0.75	1.9438	2.0211	2.1369	2.3290	2.7104	3.8290	5.5895	8.5514	13.4555
1.00	1.7821	1.8581	1.9717	2.1601	2.5335	3.6230	5.3114	8.0046	11.7834
1.50	1.4803	1.5532	1.6622	1.8424	2.1980	3.2199	4.7329	6.8056	8.9663
2.00	1.2105	1.2800	1.3837	1.5546	1.8894	2.8285	4.1188	5.5513	6.7559
2.50	0.9780	1.0435	1.1409	1.3005	1.6097	2.4465	3.4737	4.3719	5.0448
3.00	0.7850	0.8451	0.9340	1.0789	1.3559	2.0716	2.8276	3.3552	3.7360

Table 4. Case I — columns with exponentially varying stiffness.

	$\beta_0 L/EI$								
b	0	0.1	0.25	0.5	1	2	4	10	100
0.0	9.8696	10.0666	10.3511	10.7978	11.5982	12.8944	14.6602	17.0763	19.7970
0.1	9.3716	9.5634	9.8402	10.2741	11.0493	12.2985	13.9866	16.2690	18.8042
0.2	8.8635	9.0498	9.3183	9.7384	10.4868	11.6860	13.2922	15.4364	17.7834
0.3	8.3434	8.5237	8.7832	9.1885	9.9079	11.0537	12.5733	14.5737	16.7298
0.4	7.8087	7.9824	8.2321	8.6213	9.3093	10.3974	11.8247	13.6751	15.6365
0.5	7.2560	7.4224	7.6614	8.0327	8.6863	9.7116	11.0399	12.7326	14.4948
0.6	6.6812	6.8396	7.0665	7.4180	8.0334	8.9897	10.2107	11.7371	13.2950
0.7	6.0825	6.2318	6.4451	6.7745	7.3475	8.2278	9.3329	10.6842	12.0333
0.8	5.4696	5.6090	5.8077	6.1131	6.6402	7.4393	8.4228	9.5952	10.7371

Table 5. Case II — columns with linearly varying stiffness, β_L=0.

	$\beta_0 L/EI$								
b	0	0.1	0.25	0.5	1	2	4	10	100
0.0	9.8696	10.2656	10.8447	11.7719	13.4924	16.4634	20.9568	28.1683	37.9572
0.1	9.3716	9.7676	10.3458	11.2696	12.9768	15.9024	20.2681	27.1131	36.0973
0.2	8.8635	9.2599	9.8377	10.7582	12.4511	15.3254	19.5477	25.9988	34.1762
0.3	8.3434	8.7407	9.3187	10.2362	11.9131	14.7283	20.2726	24.8132	32.1791
0.4	7.8087	8.2078	8.7867	9.7015	11.3601	14.1053	17.9768	23.5401	30.0877
0.5	7.2560	7.6579	8.2386	9.1507	10.7869	13.4462	17.0968	22.1551	27.8773
0.6	6.6812	7.0870	7.6700	8.5778	10.1829	12.7305	16.1153	20.6196	25.5111
0.7	6.0825	6.4914	7.0740	7.9702	9.5239	11.9159	14.9736	18.8703	22.9324
0.8	5.4696	5.8740	6.4438	7.3060	8.7630	10.9259	13.5782	16.8166	20.0636

Table 6. Case II — columns with linearly varying stiffness, $\beta_L = \beta_0$.

	$\beta_0 L/EI$								
b	0	0.1	0.25	0.5	1	2	4	10	100
0.0	20.1907	20.4982	20.9462	21.6594	22.9688	25.1822	28.3971	33.1546	38.7118
0.1	19.1685	19.4679	19.9039	20.5971	21.8669	24.0044	27.0859	31.5885	36.7606
0.2	18.1179	18.4087	18.8318	19.5035	20.7310	22.7876	25.7281	29.9663	34.7519
0.3	17.0330	17.3144	17.7236	18.3722	19.5541	21.5237	24.3143	28.2765	32.6709
0.4	15.9057	16.1770	16.5709	17.1942	18.3265	20.2020	22.8317	26.5041	30.4993
0.5	14.7245	14.9845	15.3615	15.9569	17.0343	18.8066	21.2619	24.6272	28.2130
0.6	13.4714	13.7186	14.0766	14.6405	15.6564	17.3134	19.5769	22.6134	25.7757
0.7	12.1185	12.3509	12.6868	13.2143	14.1593	15.6846	17.7327	20.4122	23.1324
0.8	10.6238	10.8384	11.1478	11.6318	12.4924	13.8631	15.6644	17.9511	20.2078

Table 7. Case II — columns with linearly varying stiffness, $\beta_L \to \infty$.

	$\beta_0 L/EI$								
a	0	0.1	0.25	0.5	1	2	4	10	100
0.00	9.8696	10.0666	10.3511	10.7978	11.5982	12.8944	14.6602	17.0763	19.7970
0.25	8.6951	8.8800	9.1463	9.5628	10.3039	11.4894	13.0723	15.1763	17.4678
0.50	7.6345	7.8078	8.0570	8.4449	9.1301	10.2115	11.6253	13.4490	15.3706
0.75	6.6807	6.8432	7.0761	7.4371	8.0696	9.0535	10.3113	11.8848	13.4891
1.00	5.8266	5.9789	6.1965	6.5322	7.1152	8.0080	9.1226	10.4735	11.8071
1.50	4.3885	4.5224	4.7123	5.0019	5.4948	6.2237	7.0879	8.0690	8.9779
2.00	3.2634	3.3813	3.5470	3.7962	4.2104	4.7983	5.4560	6.1537	6.7615
2.50	2.3955	2.4998	2.6448	2.8592	3.2054	3.6734	4.1640	4.6491	5.0474
3.00	1.7329	1.8261	1.9540	2.1391	2.4273	2.7948	3.1528	3.4818	3.7373

Table 8. Case II — columns with exponentially varying stiffness, β_L=0.

	$\beta_0 L/EI$								
a	0	0.1	0.25	0.5	1	2	4	10	100
0.00	9.8696	10.2656	10.8447	11.7719	13.4924	16.4634	20.9568	28.1683	37.9572
0.25	8.6951	9.0912	9.6684	10.5871	12.2742	15.1312	19.3093	25.6463	33.6012
0.50	7.6345	8.0318	8.6080	9.5184	11.1681	13.8959	17.7352	23.2317	29.6633
0.75	6.6807	7.0803	7.6563	8.5575	10.1638	12.7453	16.2284	20.9375	26.1113
1.00	5.8266	6.2294	6.8054	7.6958	9.2507	11.6682	14.7864	18.7760	22.9202
1.50	4.3885	4.8003	5.3753	6.2343	7.6558	9.6994	12.1029	14.8873	17.5178
2.00	3.2634	3.6860	4.2546	5.0617	6.3049	7.9434	9.7142	11.6021	13.2518
2.50	2.3955	2.8297	3.3810	4.1094	5.1398	6.3912	7.6528	8.9047	9.9273
3.00	1.7329	2.1777	2.6960	3.3199	4.1300	5.0524	5.9299	6.7435	7.3689

Table 9. Case II — columns with exponentially varying stiffness, $\beta_L = \beta_0$.

	$\beta_0 L/EI$								
a	0	0.1	0.25	0.5	1	2	4	10	100
0.00	20.1907	20.4982	20.9462	21.6594	22.9688	25.1822	28.3971	33.1546	38.7118
0.25	17.7938	18.0823	18.5020	19.1681	20.3842	22.4186	25.3196	29.4819	34.1545
0.50	15.6379	15.9085	16.3014	16.9228	18.0507	19.9163	22.5250	26.1504	30.0674
0.75	13.7046	13.9583	14.3258	14.9051	15.9497	17.6565	19.9937	23.1361	26.4052
1.00	11.9763	12.2141	12.5577	13.0972	14.0633	15.6210	17.7068	20.4171	23.1330
1.50	9.0679	9.2767	9.5767	10.0436	10.8665	12.1541	13.7950	15.7797	17.6281
2.00	6.7879	6.9712	7.2329	7.6360	8.3327	9.3851	10.6528	12.0744	13.3081
2.50	5.0249	5.1861	5.4144	5.7615	6.3477	7.1965	8.1554	9.1490	9.9556
3.00	3.6800	3.8224	4.0220	4.3206	4.8104	5.4843	6.1918	6.8675	7.3829

Table 10. Case II — columns with exponentially varying stiffness, $\beta_L \to \infty$.

	$\beta_0 L/EI$								
b	0	0.1	0.25	0.5	1	2	4	10	100
0.0	0.0000	0.0968	0.2305	0.4268	0.7402	1.1597	1.5992	2.0417	2.4188
0.1	0.0000	0.0967	0.2300	0.4250	0.7347	1.1453	1.5703	1.9922	2.3473
0.2	0.0000	0.0966	0.2295	0.4232	0.7288	1.1300	1.5395	1.9403	2.2732
0.3	0.0000	0.0965	0.2289	0.4211	0.7224	1.1133	1.5067	1.8856	2.1959
0.4	0.0000	0.0964	0.2283	0.4189	0.7153	1.0953	1.4714	1.8276	2.1148
0.5	0.0000	0.0963	0.2276	0.4164	0.7075	1.0754	1.4331	1.7655	2.0293
0.6	0.0000	0.0961	0.2268	0.4136	0.6987	1.0534	1.3912	1.6987	1.9384
0.7	0.0000	0.0960	0.2260	0.4106	0.6891	1.0291	1.3455	1.6269	1.8420
0.8	0.0000	0.0961	0.2255	0.4079	0.6795	1.0041	1.2981	1.5528	1.7433

Table 11. Case III — columns with linearly varying stiffness, β_L=0.

	$\beta_0 L/EI$								
b	0	0.1	0.25	0.5	1	2	4	10	100
0.0	0.0000	0.1967	0.4798	0.9220	1.7071	2.9607	4.6386	6.9047	9.4865
0.1	0.0000	0.1965	0.4788	0.9180	1.6933	2.9182	4.5311	6.6604	9.0232
0.2	0.0000	0.1963	0.4775	0.9134	1.6773	2.8698	4.4121	6.3987	8.5430
0.3	0.0000	0.1961	0.4760	0.9078	1.6585	2.8142	4.2791	6.1165	8.0429
0.4	0.0000	0.1957	0.4741	0.9010	1.6358	2.7492	4.1288	5.8099	7.5185
0.5	0.0000	0.1952	0.4715	0.8921	1.6075	2.6713	3.9561	5.4726	6.9637
0.6	0.0000	0.1942	0.4673	0.8791	1.5695	2.5738	3.7520	5.0946	6.3687
0.7	0.0000	0.1916	0.4587	0.8569	1.5131	2.4437	3.5003	4.6591	5.7178
0.8	0.0000	0.1845	0.4392	0.8142	1.4207	2.2575	3.1740	4.1383	4.9853

Table 12. Case III — columns with linearly varying stiffness, $\beta_L = \beta_0$.

	$\beta_0 L/EI$								
b	0	0.1	0.25	0.5	1	2	4	10	100
0.0	2.4674	2.6634	2.9430	3.3731	4.1159	5.2392	6.6071	8.1955	9.6752
0.1	2.2928	2.4857	2.7604	3.1821	3.9076	4.9969	6.3089	7.8103	9.1890
0.2	2.1154	2.3048	2.5743	2.9869	3.6937	4.7466	5.9993	7.4106	8.6869
0.3	1.9346	2.1203	2.3839	2.7866	3.4729	4.4864	5.6760	6.9935	8.1658
0.4	1.7495	1.9310	2.1883	2.5800	3.2437	4.2140	5.3359	6.5553	7.6214
0.5	1.5589	1.7357	1.9857	2.3650	3.0036	3.9262	4.9746	6.0903	7.0476
0.6	1.3608	1.5323	1.7740	2.1390	2.7488	3.6176	4.5850	5.5902	6.4348
0.7	1.1522	1.3172	1.5490	1.8972	2.4732	3.2797	4.1559	5.0413	5.7679
0.8	0.9276	1.0846	1.3042	1.6316	2.1661	2.8978	3.6682	4.4207	5.0217

Table 13. Case III — columns with linearly varying stiffness, $\beta_L \to \infty$.

	$\beta_0 L/EI$								
a	0	0.1	0.25	0.5	1	2	4	10	100
0.00	0.0000	0.0968	0.2305	0.4268	0.7402	1.1597	1.5992	2.0417	2.4188
0.25	0.0000	0.0965	0.2293	0.4224	0.7265	1.1240	1.5278	1.9208	2.2456
0.50	0.0000	0.0963	0.2279	0.4177	0.7117	1.0862	1.4542	1.8001	2.0774
0.75	0.0000	0.0961	0.2265	0.4125	0.6957	1.0462	1.3787	1.6803	1.9148
1.00	0.0000	0.0958	0.2248	0.4068	0.6783	1.0041	1.3015	1.5617	1.7582
1.50	0.0000	0.0951	0.2210	0.3936	0.6392	0.9132	1.1436	1.3307	1.4644
2.00	0.0000	0.0943	0.2162	0.3775	0.5934	0.8141	0.9835	1.1115	1.1986
2.50	0.0000	0.0931	0.2098	0.3569	0.5390	0.7067	0.8237	0.9064	0.9603
3.00	0.0000	0.0908	0.1999	0.3285	0.4722	0.5896	0.6643	0.7142	0.7457

Table 14. Case III — columns with exponentially varying stiffness, β_L=0.

	$\beta_0 L/EI$								
a	0	0.1	0.25	0.5	1	2	4	10	100
0.00	0.0000	0.1967	0.4798	0.9220	1.7071	2.9607	4.6386	6.9047	9.4865
0.25	0.0000	0.1963	0.4772	0.9120	1.6727	2.8559	4.3782	6.3250	8.4094
0.50	0.0000	0.1957	0.4740	0.9004	1.6335	2.7421	4.1111	5.7711	7.4488
0.75	0.0000	0.1951	0.4701	0.8867	1.5895	2.6202	3.8410	5.2466	6.5926
1.00	0.0000	0.1943	0.4656	0.8709	1.5404	2.4917	3.5716	4.7537	5.8301
1.50	0.0000	0.1921	0.4538	0.8323	1.4289	2.2214	3.0468	3.8658	4.5463
2.00	0.0000	0.1892	0.4382	0.7845	1.3033	1.9450	2.5555	3.1061	3.5282
2.50	0.0000	0.1852	0.4184	0.7288	1.1695	1.6731	2.1077	2.4651	2.7204
3.00	0.0000	0.1799	0.3942	0.6669	1.0314	1.4111	1.7059	1.9282	2.0780

Table 15. Case III — columns with exponentially varying stiffness, $\beta_L = \beta_0$.

	$\beta_0 L/EI$								
a	0	0.1	0.25	0.5	1	2	4	10	100
0.00	2.4674	2.6634	2.9430	3.3731	4.1159	5.2392	6.6071	8.1955	9.6752
0.25	2.0666	2.2553	2.5237	2.9344	3.6366	4.6801	5.9165	7.3018	8.5478
0.50	1.7254	1.9076	2.1656	2.5580	3.2220	4.1898	5.3033	6.5057	7.5498
0.75	1.4364	1.6124	1.8608	2.2361	2.8638	3.7595	4.7581	5.7959	6.6662
1.00	1.1924	1.3628	1.6022	1.9614	2.5545	3.3812	4.2723	5.1623	5.8834
1.50	0.8153	0.9759	1.1990	1.5284	2.0559	2.7527	3.4489	4.0890	4.5742
2.00	0.5525	0.7047	0.9134	1.2152	1.6803	2.2555	2.7820	3.2263	3.5426
2.50	0.3722	0.5171	0.7127	0.9880	1.3919	1.8521	2.2336	2.5290	2.7278
3.00	0.2507	0.3891	0.5720	0.8203	1.1621	1.5137	1.7751	1.9618	2.0818

Table 16. Case III — columns with exponentially varying stiffness, $\beta_L \to \infty$.

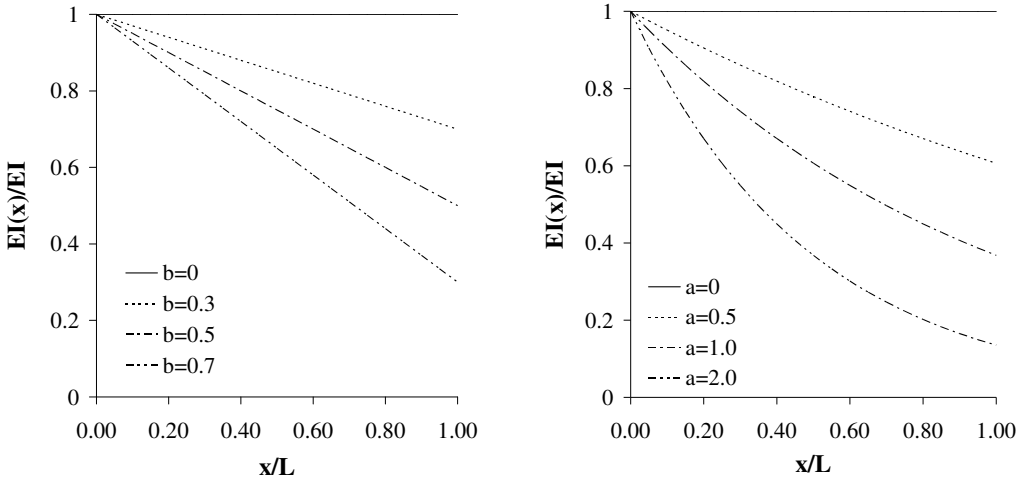

Figure 4. Stiffness variations studied in the paper in more detail. Left: linear variation in stiffness. Right: exponential variation in stiffness.

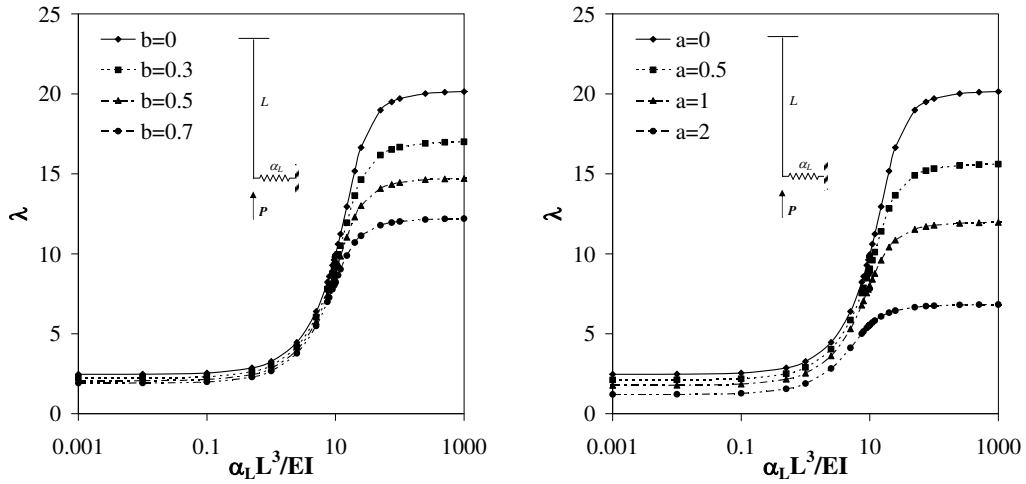

Figure 5. Case I — columns with variable stiffness: variation of normalized buckling load with normalized linear spring stiffness. Left: linear variation in stiffness. Right: exponential variation in stiffness.

Figure 5 shows the variation of normalized buckling load with normalized linear spring stiffness for columns of variable stiffness with the end conditions considered in Case I. Recalling that the cases for b=0 and a=0 correspond to uniform columns, it can be seen from these graphs that as the sharpness of the stiffness variation (a or b) increases, the buckling load of the column decreases considerably especially if the spring stiffness is large. Figure 5 also shows that there is no need to increase the spring stiffness beyond a critical value because further increases will result in no change in buckling load. For a particular case, this "critical" value of the spring stiffness can easily be determined using VIM.

Figures 6 and 7 show the variation of normalized buckling load with normalized rotational spring stiffnesses for columns of, respectively, linearly and exponentially variable flexural stiffness with the boundary conditions considered in Case II. Similarly, Figures 8 and 9 show the effect of rotational spring stiffnesses on normalized buckling load for columns of, respectively, linearly and exponentially variable flexural stiffness with the boundary conditions considered in Case III. Comparison of the graphs presented in Figures 6 and 7 with those given in Figures 8 and 9 clearly shows the importance of the lateral bracing of the columns. Case II columns with lateral bracing have much larger elastic buckling loads compared to Case III columns which are free to displace in lateral direction.

5. Conclusions

In an attempt to construct ever-stronger and ever-lighter structures, many engineers currently design slender high strength columns with variable cross sections and various end conditions. Even though buckling behavior of uniform columns with ideal boundary conditions are extensively studied, there are limited studies in the literature on buckling analysis of nonuniform columns with elastic end restraints. This is due to the fact that such an analysis requires the solution of more complex differential equations for which it is usually impractical or sometimes even impossible to obtain exact solutions.

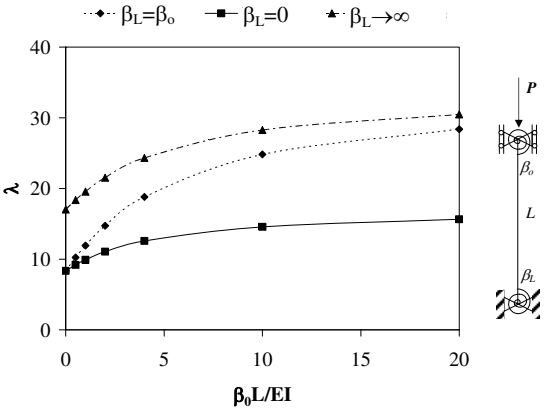

	λ		
$\beta_0 L/EI$	$\beta_L=\beta_0$	$\beta_L=0$	$\beta_L\to\infty$
0	8.34341	8.34341	17.033
0.5	10.2362	9.18849	18.3722
1	11.9131	9.90792	19.5541
2	14.7283	11.0537	21.5237
4	18.7877	12.5733	24.3143
10	24.8132	14.5737	28.2765
20	28.3848	15.6475	30.4787

a. b=0.3

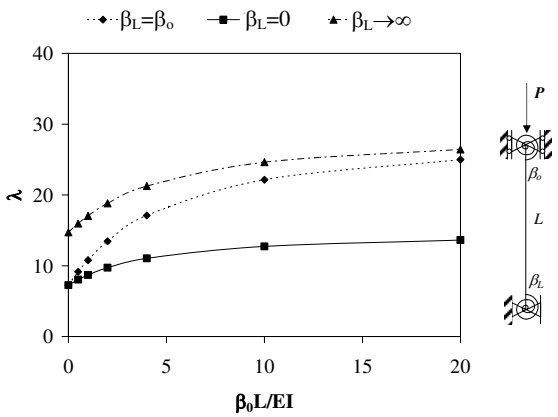

	λ		
$\beta_0 L/EI$	$\beta_L=\beta_0$	$\beta_L=0$	$\beta_L\to\infty$
0	7.25597	7.25597	14.7245
0.5	9.1507	8.03271	15.9569
1	10.7869	8.68631	17.0343
2	13.4462	9.71162	18.8066
4	17.0968	11.0399	21.2619
10	22.1551	12.7326	24.6272
20	24.9815	13.6171	26.4395

b. b=0.5

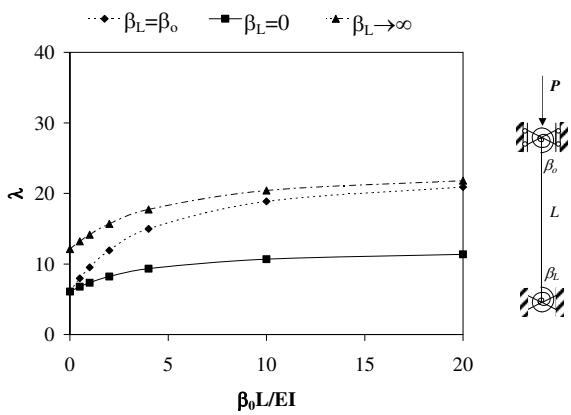

	λ		
$\beta_0 L/EI$	$\beta_L=\beta_0$	$\beta_L=0$	$\beta_L\to\infty$
0	6.08246	6.08246	12.1185
0.5	7.97022	6.77453	13.2143
1	9.52393	7.3475	14.1593
2	11.9159	8.2278	15.6846
4	14.9736	9.33292	17.7327
10	18.8703	10.6842	20.4122
20	20.9134	11.3675	21.8001

c. b=0.7

Figure 6. Case II — variation of normalized buckling load with normalized rotational spring stiffnesses for columns with linearly varying stiffness.

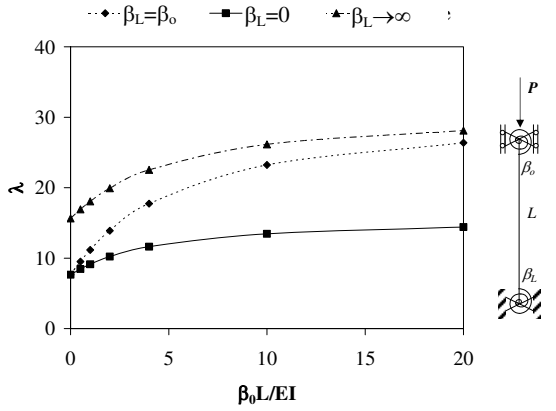

	λ		
$\beta_0 L/EI$	$\beta_L=\beta_0$	$\beta_L=0$	$\beta_L\to\infty$
0	7.63449	7.63449	15.6379
0.5	9.51836	8.44491	16.9228
1	11.1681	9.13009	18.0507
2	13.8959	10.2115	19.9163
4	17.7352	11.6253	22.525
10	23.2317	13.449	26.1504
20	26.3844	14.411	28.125

a. a=0.5

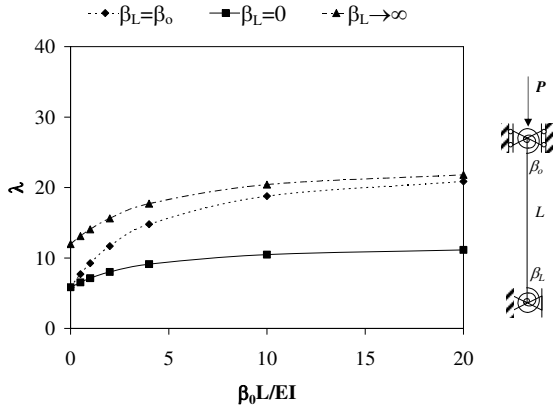

	λ		
$\beta_0 L/EI$	$\beta_L=\beta_0$	$\beta_L=0$	$\beta_L\to\infty$
0	5.82655	5.82655	11.9763
0.5	7.69583	6.53223	13.0972
1	9.25074	7.11518	14.0633
2	11.6682	8.00799	15.621
4	14.7864	9.12257	17.7068
10	18.776	10.4735	20.4171
20	20.864	11.1509	21.8082

b. a=1

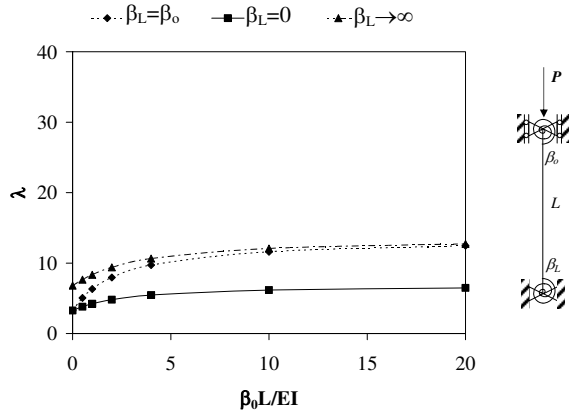

	λ		
$\beta_0 L/EI$	$\beta_L=\beta_0$	$\beta_L=0$	$\beta_L\to\infty$
0	3.26337	3.26337	6.78791
0.5	5.06173	3.79622	7.63600
1	6.30488	4.2104	8.33274
2	7.94339	4.79829	9.38508
4	9.71424	5.45597	10.6528
10	11.6021	6.15367	12.0744
20	12.4645	6.47049	12.7239

c. a=2

Figure 7. Case II — variation of normalized buckling load with normalized rotational spring stiffnesses for columns with exponentially varying stiffness.

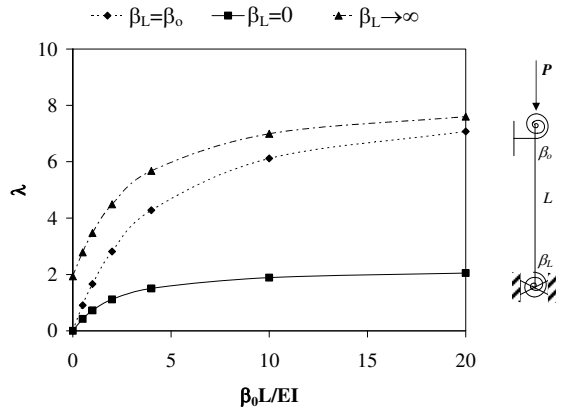

	λ		
$\beta_0 L/EI$	$\beta_L=\beta_0$	$\beta_L=0$	$\beta_L\to\infty$
0	0.00000	0.00000	1.93455
0.5	0.90783	0.42114	2.78663
1	1.65849	0.72239	3.47294
2	2.81421	1.11334	4.48636
4	4.27910	1.50670	5.67600
10	6.11654	1.88562	6.99354
20	7.07751	2.04883	7.60366

a. b=0.3

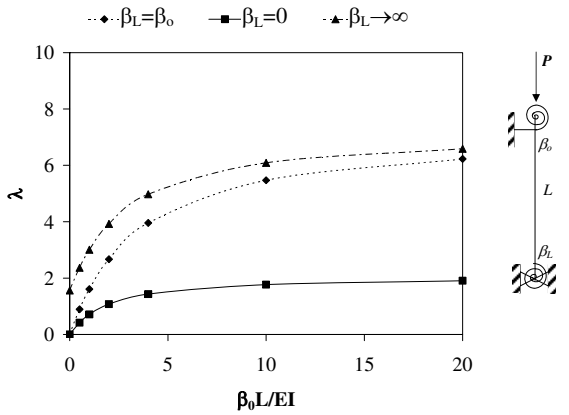

	λ		
$\beta_0 L/EI$	$\beta_L=\beta_0$	$\beta_L=0$	$\beta_L\to\infty$
0	0.00000	0.00000	1.55885
0.5	0.89207	0.41639	2.36504
1	1.60747	0.70749	3.00361
2	2.67126	1.07538	3.92620
4	3.95605	1.43309	4.97456
10	5.47257	1.76553	6.09031
20	6.22766	1.90520	6.59212

b. b=0.5

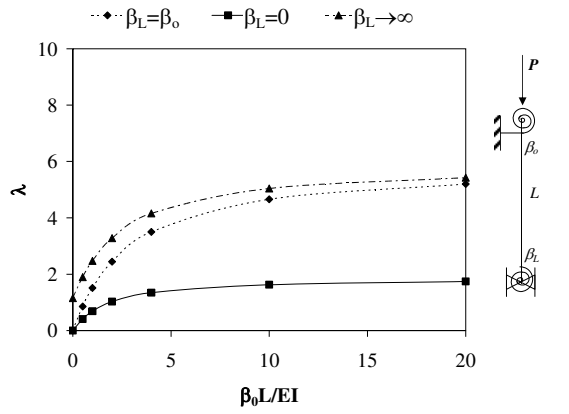

	λ		
$\beta_0 L/EI$	$\beta_L=\beta_0$	$\beta_L=0$	$\beta_L\to\infty$
0	0.00000	0.00000	1.15216
0.5	0.85687	0.41056	1.89724
1	1.51307	0.68909	2.47320
2	2.44373	1.02909	3.27971
4	3.50031	1.34553	4.15588
10	4.65906	1.62689	5.04125
20	5.20407	1.74162	5.42537

c. b=0.7

Figure 8. Case III — variation of normalized buckling load with normalized rotational spring stiffnesses for columns with linearly varying stiffness.

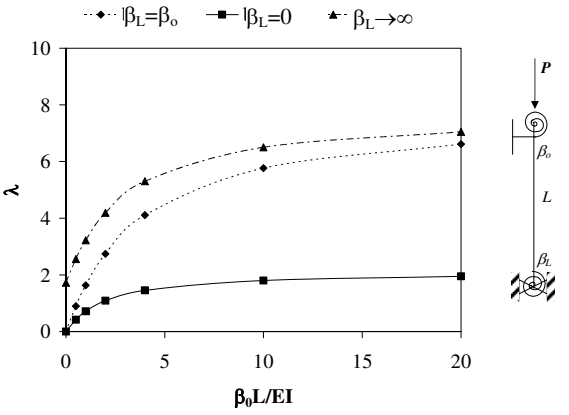

	λ		
$\beta_0 L/EI$	$\beta_L=\beta_0$	$\beta_L=0$	$\beta_L\to\infty$
0	0.00000	0.00000	1.72544
0.5	0.90036	0.41772	2.55800
1	1.63354	0.71170	3.22202
2	2.74207	1.08621	4.18976
4	4.11106	1.45422	5.30329
10	5.77112	1.80014	6.50565
20	6.61537	1.94665	7.05180

a. a=0.5

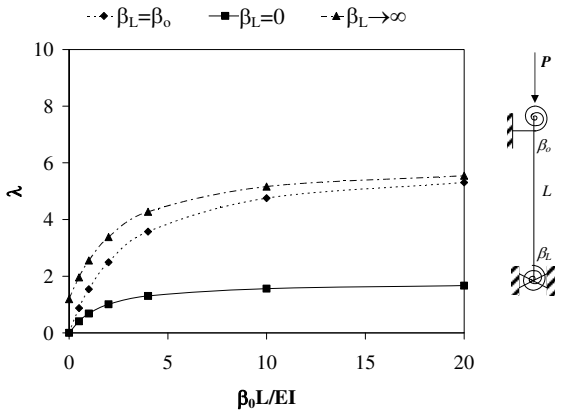

	λ		
$\beta_0 L/EI$	$\beta_L=\beta_0$	$\beta_L=0$	$\beta_L\to\infty$
0	0.00000	0.00000	1.19237
0.5	0.87089	0.40682	1.96144
1	1.54044	0.67830	2.55445
2	2.49166	1.00407	3.38124
4	3.57160	1.30152	4.27229
10	4.75369	1.56165	5.16229
20	5.30830	1.66670	5.54461

b. a=1

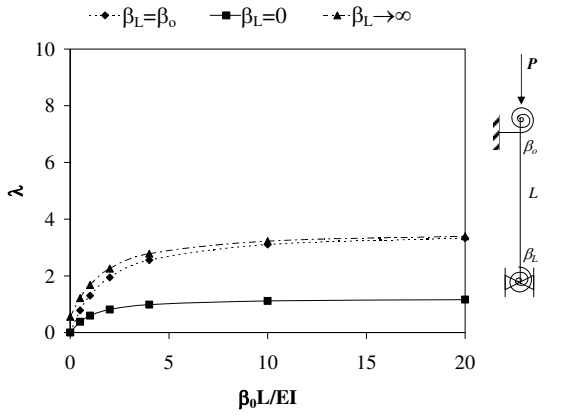

	λ		
$\beta_0 L/EI$	$\beta_L=\beta_0$	$\beta_L=0$	$\beta_L\to\infty$
0	0.00000	0.00000	0.55250
0.5	0.78447	0.37748	1.21519
1	1.30331	0.59337	1.68031
2	1.94497	0.81411	2.25547
4	2.55547	0.98351	2.78196
10	3.10614	1.11153	3.22630
20	3.33138	1.15897	3.39786

c. a=2

Figure 9. Case III — variation of normalized buckling load with normalized rotational spring stiffnesses for columns with exponentially varying stiffness.

This paper shows that the variational iteration method (VIM) can successfully be used to determine the buckling loads of slender columns with elastic end restraints. To the best knowledge of author, exact solutions to this problem are available only for some particular cases of uniform columns. For this reason, before analyzing the columns with variable cross sections, the buckling loads of columns with constant cross sections are determined using classical variational iteration algorithm and VIM results are compared to the exact results, which show perfect match. After verifying the efficiency of VIM in the analysis of this special type of buckling problem, the columns with variable flexural stiffness are analyzed using this practical technique. It is shown that unlike exact solution procedures, variational iteration algorithms can easily be used even when the column stiffness change along its length exponentially or linearly and/or the end conditions are rather complex.

References

[Abulwafa et al. 2007] E. M. Abulwafa, M. A. Abdou, and A. A. Mahmoud, "Nonlinear fluid flows in pipe-like domain problem using variational-iteration method", *Chaos Solitons Fractals* **32**:4 (2007), 1384–1397.

[Arbabi and Li 1991] F. Arbabi and F. Li, "Buckling of variable cross-section columns - integral equation approach", *J. Struct. Eng. -ASCE* **117**:8 (1991), 2426–2441.

[Atanackovic and Novakovic 2006] T. M. Atanackovic and B. N. Novakovic, "Optimal shape of an elastic column on elastic foundation", *Eur. J. Mech. A Solids* **25**:1 (2006), 154–165.

[Atanackovic et al. 2010] T. M. Atanackovic, B. B. Jakovljevic, and M. R. Petkovic, "On the optimal shape of a column with partial elastic foundation", *Eur. J. Mech. A Solids* **29**:2 (2010), 283–289.

[Atay 2009] M. T. Atay, "Determination of critical buckling loads for variable stiffness Euler columns using homotopy perturbation method", *Int. J. Nonlinear Sci. Numer. Sim.* **10**:2 (2009), 199–206.

[Atay 2010] M. T. Atay, "Determination of buckling loads of tilted buckled column with varying flexural rigidity using variational iteration method", *Int. J. Nonlinear Sci. Numer. Sim.* **11** (2010), 93–103.

[Atay and Coşkun 2009] M. T. Atay and S. B. Coşkun, "Elastic stability of Euler columns with a continuous elastic restraint using variational iteration method", *Comput. Math. Appl.* **58**:11–12 (2009), 2528–2534.

[Aydogdu 2008] M. Aydogdu, "Semi-inverse method for vibration and buckling of axially functionally graded beams", *J. Reinforced Plastics Compos.* **27**:7 (2008), 683–691.

[Batiha et al. 2007] B. Batiha, M. S. M. Noorani, and I. Hashim, "Application of variational iteration method to heat- and wave-like equations", *Phys. Lett. A* **369** (2007), 55–61.

[Cailo and Elishakoff 2004] I. Cailo and I. Elishakoff, "Can a trigonometric function serve both as the vibration and the buckling mode of an axially graded structure?", *Mech. Based Des. Struct. Mach.* **32**:4 (2004), 401–421.

[Chajes 1974] A. Chajes, *Principles of structural stability theory*, Prentice Hall, Englewood Cliffs, NJ, 1974.

[Civalek 2004] O. Civalek, "Application of differential quadrature (DQ) and harmonic differential quadrature (HDQ) for buckling analysis of thin isotropic plates and elastic columns", *Eng. Struct.* **26**:2 (2004), 171–186.

[Coşkun 2009] S. B. Coşkun, "Determination of critical buckling loads for Euler columns of variable flexural stiffness with a continuous elastic restraint using homotopy perturbation method", *Int. J. Nonlinear Sci. Numer. Sim.* **10**:2 (2009), 191–197.

[Coşkun and Atay 2008] S. B. Coşkun and M. T. Atay, "Fin efficiency analysis of convective straight fins with temperature dependent thermal conductivity using variational iteration method", *Appl. Therm. Eng.* **28**:17–18 (2008), 2345–2352.

[Coşkun et al. 2011] S. B. Coşkun, M. T. Atay, and B. Ozturk, "Transverse vibration analysis of Euler-Bernoulli beams using analytical approximate techniques", pp. 1–22 in *Advances in Vibration Analysis Research, InTech*, edited by F. Ebrahimi, 2011.

[Coşkun 2010] S. B. Coşkun, "Analysis of tilt-buckling of Euler columns with varying flexural stiffness using homotopy perturbation method", *Math. Model. Anal.* **15**:3 (2010), 275–286.

[Coşkun and Atay 2007] S. B. Coşkun and M. T. Atay, "Analysis of convective straight and radial fins with temperature-dependent thermal conductivity using variational iteration method with comparison with respect to finite element analysis", *Math. Probl. Eng.* (2007), Art. ID 42072, 15.

[Coşkun and Atay 2009] S. B. Coşkun and M. T. Atay, "Determination of critical buckling load for elastic columns of constant and variable cross-sections using variational iteration method", *Comput. Math. Appl.* **58**:11–12 (2009), 2260–2266.

[Du et al. 1996] H. Du, K. M. Liew, and M. K. Lim, "Generalized differential quadrature method for buckling analysis", *J. Eng. Mech.* **122**:2 (1996), 95–100.

[Eisenberger and Clastornik 1987] M. Eisenberger and J. Clastornik, "Vibrations and buckling of a beam on a variable winkler elastic foundation", *J. Sound Vib.* **115** (1987), 233–241.

[Ganji and Sadighi 2007] D. D. Ganji and A. Sadighi, "Application of homotopy-perturbation and variational iteration methods to nonlinear heat transfer and porous media equations", *J. Comput. Appl. Math.* **207**:1 (2007), 24–34.

[Ganji et al. 2007] D. D. Ganji, G. A. Afrouzi, and R. A. Talarposhti, "Application of variational iteration method and homotopy–perturbation method for nonlinear heat diffusion and heat transfer equations", *Phys. Lett. A* **368** (2007), 450–457.

[Ganji et al. 2008] D. D. Ganji, A. Sadighi, and I. Khatami, "Assessment of two analytical approaches in some nonlinear problems arising in engineering sciences", *Phys. Lett. A* **372** (2008), 4399–4406.

[Geng 2011] F. Geng, "A piecewise variational iteration method for treating a nonlinear oscillator of a mass attached to a stretched elastic wire", *Comput. Math. Appl.* **62**:4 (2011), 1641–1644.

[He 1999] J. H. He, "Variational iteration method - a kind of nonlinear analytical technique: some examples", *Int. J. Non Linear Mech.* **34**:4 (1999), 699–708.

[He et al. 2010] J. H. He, G. C. Wu, and F. Austin, "The variational iteration method which should be followed", *Nonlinear Sci. Lett. A.* **1**:1 (2010), 1–30.

[Huang and Luo 2011] Y. Huang and Q.-Z. Luo, "A simple method to determine the critical buckling loads for axially inhomogeneous beams with elastic restraint", *Comput. Math. Appl.* **61**:9 (2011), 2510–2517.

[Li 2000] Q. S. Li, "Buckling of elastically restrained non-uniform columns", *Eng. Struct.* **22** (2000), 1231–1243.

[Li 2001] Q. S. Li, "Buckling of multi-step non-uniform beams with elastically restrained boundary conditions", *J. Constr. Steel Res.* **57** (2001), 753–777.

[Li 2003] Q. S. Li, "Buckling analysis of non-uniform bars with rotational and translational springs", *Eng. Struct.* **25** (2003), 1289–1299.

[Liu and Gurram 2009] Y. Liu and C. S. Gurram, "The use of He's variational iteration method for obtaining the free vibration of an Euler-Bernoulli beam", *Math. Comput. Modelling* **50**:11–12 (2009), 1545–1552.

[Malekzadeh and Karami 2008] P. Malekzadeh and G. Karami, "A mixed differential quadrature and finite element free vibration and buckling analysis of thick beams on two-parameter elastic foundations", *Appl. Math. Model.* **32** (2008), 1381–1394.

[Miansari et al. 2008] M. Miansari, D. D. Ganji, and M. Miansari, "Application of He's variational iteration method to nonlinear heat transfer equations", *Phys. Lett. A* **372**:6 (2008), 779–785.

[Okay et al. 2010] F. Okay, M. T. Atay, and S. B. Coşkun, "Determination of buckling loads and mode shapes of a heavy vertical column under its own weight using the variational iteration method", *Int. J. Nonlinear Sci. Numer. Simul.* **11**:10 (2010), 851–857.

[Ozturk 2009] B. Ozturk, "Free vibration analysis of beam on elastic foundation by variational iteration method", *Int. J. Nonlinear Sci. Numer. Sim.* **10**:10 (2009), 1255–1262.

[Ozturk and Coşkun 2011] B. Ozturk and S. B. Coşkun, "The homotopy perturbation method for free vibration analysis of beam on elastic foundation", *Struct. Eng. Mech.* **37** (2011), 415–425.

[Ozturk and Sabuncu 2005] H. Ozturk and M. Sabuncu, "Stability analysis of a cantilever composite beam on elastic supports", *Compos. Sci. Technol* **65** (2005), 1982–1995.

[Pinarbasi 2011] S. Pinarbasi, "Lateral torsional buckling of rectangular beams using variational iteration method", *Sci. Res. Essays* **6**:6 (2011), 1445–1457.

[Rosa and Franciosi 1996] D. M. A. Rosa and C. Franciosi, "The optimized Rayleigh method and mathematica in vibrations and buckling problems", *J. Sound Vib.* **191** (1996), 795–808.

[Serna et al. 2011] M. A. Serna, J. R. Ibanez, and A. Lopez, "Elastic flexural buckling of non-uniform members: closed-form expression and equivalent load approach", *J. Constr. Steel Res.* **67** (2011), 1078–1085.

[Shou and He 2008] D.-H. Shou and J.-H. He, "Beyond Adomian method: the variational iteration method for solving heat-like and wave-like equations with variable coefficients", *Phys. Lett. A* **372**:3 (2008), 233–237.

[Simitses and Hodges 2006] G. J. Simitses and D. H. Hodges, *Fundamentals of structural stability*, Elsevier, 2006.

[Singh and Li 2009] K. V. Singh and G. Li, "Buckling of functionally graded and elastically restrained non-uniform columns", *Compos. Part B-Eng.* **40** (2009), 393–403.

[Sweilam and Khader 2007] N. H. Sweilam and M. M. Khader, "Variational iteration method for one dimensional nonlinear thermoelasticity", *Chaos Solitons Fractals* **32**:1 (2007), 145–149.

[Tan and Yuan 2008] K. H. Tan and W. F. Yuan, "Buckling of elastically restrained steel columns under longitudinal non-uniform temperature distribution", *J. Constr. Steel Res.* **64** (2008), 51–61.

[Timoshenko 1961] S. P. Timoshenko, *Theory of elastic stability*, 2nd ed., McGraw-Hill, New York, 1961.

[Wang et al. 2005] C. M. Wang, C. Y. Wang, and J. N. Reddy, *Exact solutions for buckling of structural members*, CRC Press, Florida, 2005.

[Yang and Chen 2011] G. Yang and R. Chen, "Choice of an optimal initial solution for a wave equation in the variational iteration method", *Comput. Math. Appl.* **61**:8 (2011), 2053–2057.

[Yuan and Wang 2011] Z. Yuan and X. Wang, "Buckling and post-buckling analysis of extensive beam-columns by using the differential quadrature method", *Comput. Math. Appl.* **62**:12 (2011), 4499–4513.

Received 8 Mar 2012. Revised 5 Jun 2012. Accepted 9 Jul 2012.

SEVAL PINARBASI: sevalp@gmail.com
Department of Civil Engineering, Kocaeli University, Umuttepe Campus, 41380 Kocaeli, Turkey, Phone: +90 262 303 3274, Fax: +90 262 303 3003

SUBMISSION GUIDELINES

ORIGINALITY

Authors may submit manuscripts in PDF format online at the Submissions page. Submission of a manuscript acknowledges that the manuscript is original and has neither previously, nor simultaneously, in whole or in part, been submitted elsewhere. Information regarding the preparation of manuscripts is provided below. Correspondence by email is requested for convenience and speed. For further information, write to one of the Chief Editors:

Davide Bigoni	bigoni@ing.unitn.it
Iwona Jasiuk	ijasiuk@me.concordia.ca
Yasuhide Shindo	shindo@material.tohoku.ac.jp

LANGUAGE

Manuscripts must be in English. A brief abstract of about 150 words or less must be included. The abstract should be self-contained and not make any reference to the bibliography. Also required are keywords and subject classification for the article, and, for each author, postal address, affiliation (if appropriate), and email address if available. A home-page URL is optional.

FORMAT

Authors can use their preferred manuscript-preparation software, including for example Microsoft Word or any variant of TEX. The journal itself is produced in LATEX, so accepted articles prepared using other software will be converted to LATEX at production time. Authors wishing to prepare their document in LATEX can follow the example file at www.jomms.net (but the use of other class files is acceptable). At submission time only a PDF file is required. After acceptance, authors must submit all source material (see especially Figures below).

REFERENCES

Bibliographical references should be complete, including article titles and page ranges. All references in the bibliography should be cited in the text. The use of BibTEX is preferred but not required. Tags will be converted to the house format (see a current issue for examples); however, for submission you may use the format of your choice. Links will be provided to all literature with known web locations; authors can supply their own links in addition to those provided by the editorial process.

FIGURES

Figures must be of publication quality. After acceptance, you will need to submit the original source files in vector format for all diagrams and graphs in your manuscript: vector EPS or vector PDF files are the most useful. (EPS stands for Encapsulated PostScript.)

Most drawing and graphing packages—Mathematica, Adobe Illustrator, Corel Draw, MATLAB, etc.—allow the user to save files in one of these formats. Make sure that what you're saving is vector graphics and not a bitmap. If you need help, please write to graphics@msp.org with as many details as you can about how your graphics were generated.

Please also include the original data for any plots. This is particularly important if you are unable to save Excel-generated plots in vector format. Saving them as bitmaps is not useful; please send the Excel (.xls) spreadsheets instead. Bundle your figure files into a single archive (using zip, tar, rar or other format of your choice) and upload on the link you been given at acceptance time.

Each figure should be captioned and numbered so that it can float. Small figures occupying no more than three lines of vertical space can be kept in the text ("the curve looks like this:"). It is acceptable to submit a manuscript with all figures at the end, if their placement is specified in the text by means of comments such as "Place Figure 1 here". The same considerations apply to tables.

WHITE SPACE

Forced line breaks or page breaks should not be inserted in the document. There is no point in your trying to optimize line and page breaks in the original manuscript. The manuscript will be reformatted to use the journal's preferred fonts and layout.

PROOFS

Page proofs will be made available to authors (or to the designated corresponding author) at a Web site in PDF format. Failure to acknowledge the receipt of proofs or to return corrections within the requested deadline may cause publication to be postponed.

Journal of Mechanics of Materials and Structures

Volume 7, No. 5 May 2012

1559-3959(2012)7:5;1-9